FERMILAB-THESIS-2024-20

BOOSTED DARK MATTER SEARCH WITH THE ICARUS DETECTOR AT THE GRAN SASSO UNDERGROUND NATIONAL LABORATORY

by

HECTOR CARRANZA JR.

Presented to the Faculty of the Graduate School of
The University of Texas at Arlington in Partial Fulfillment of the
Requirements for the Degree of

DOCTOR OF PHILOSOPHY

THE UNIVERSITY OF TEXAS
AT ARLINGTON

December 2024

Supervising Committee
Dr. Jaehoon Yu, Supervisor
Dr. Jonathan A. Asaadi
Dr. Ramon E. Lopez
Dr. Benjamin J.P. Jones
Dr. Zdzislaw E. Musielak

To my mom, dad, and wife

Acknowledgement

Achieving success in my Ph.D journey was only possible because of the huge support network I have. This support network is on the order of hundreds. I am lucky to have friends and family tell me they wish me success. It is because of the encouragement that I did not give up, despite all the curve balls either life threw at me or I threw at myself.

My network starts with my mother and my father. Without both of you, well, I would not even exist. You have always supported me to be my best, no matter the cost. The love, emotional support, and financial support over my whole physics career are immeasurable. You both are the greatest parents I could have ever asked for, and I love you both. Mom, thank you for talking to me through nights, even at 2am in times when I was lost. You knew the words that I needed to get back up. Dad, thank you for never doubting that I could make it, no matter how long it took. I hope the physics that we yet do not understand allows you to know that we made it. If not, well, when I see you, I will tell you all about it.

To my lovely wife, Ana, thank you for being so supportive since we first met in 2016. My journey through the Ph.D encompasses our whole relationship, and I could not have asked for a better person to be by my side throughout my ups and downs. We got together, fell in love, and married each other through the span of my Ph.D. You traveled with me and made sure I took the time to enjoy life. You helped me get organized when my work got chaotic and helped me see clearly during very difficult times. Now, we have finally made it and can go into the future.

A big thank you to my supervisor, Jaehoon Yu, for endless support during my highest

moments and lowest moments. My Ph.D. spanned a long eight years, with five of those years performing research under your guidance. This is not possible without the belief that I am able to achieve, and here we are. You put your faith in me even when I failed along the way. You would still see a light at the end of the tunnel and guided me to see it as well. I got to know and work with all the amazing people throughout my Ph.D. because of your recommendations, enabling my growth as a physicist. This dissertation could only get to this final stage because of the countless revisions and suggestions you gave me.

Thank you to the whole ICARUS collaboration at Gran Sasso for allowing me and our team at UTA to perform an analysis of the ICARUS data collected at Gran Sasso. Special thanks to Carlo Rubbia, Alberto Guglielmi, Christian Farnese, Daniele Gibin, and Angela Fava for their patience and support in the completion of this dissertation. This is only possible because of their gracious support throughout the analysis, even with everything on their plate. The work put into getting our paper ready to publish was enormous from all of you and Jae, and it was an honor to publish the paper with all of you. Thank you, Christian, for sharing, explaining, and guiding me through the use of the ICARUS at Gran Sasso detector simulation tools, even on your busiest days.

Thank Doojin Kim for your theoretical guidance in understanding boosted dark matter and the Monte Carlo event generator to perform this study. Since 2019, you have educated me on the codes you built and the theory necessary to understand the output of the event generator. This was a foundational step in getting the preliminary study up and running and then subsequently performing the full-blown analysis.

I would like to acknowledge and thank everyone in the DUNE collaboration during my involvement with the installation and commissioning of the ProtoDUNE Dual Phase detector. My understanding of the Liquid Argon Time Projection Chamber was very minimal, and I was fortunate to learn directly from top experts in the field. Special thanks to Filippo Resnati, Francesco Pietropaolo, Dominique Duchesneau, Dario Auterio, and Surhan Tufanli for teaching me their knowledge of LArTPCs and mentoring me with hands-on experience

with the various components of the detector. The best way to learn is to dive right in, and I definitely dove right into the installation and commissioning of the ProtoDUNE Dual Phase detector. In order to perform an analysis with the hardware, knowledge of the software is necessary, and I have Francesca Stocker to thank for teaching me the basic ins and outs of the analysis software LArSoft.

I would also like to thank Stephen Pordes for his guidance since the first day we met back at the beginning of 2019. My life in Switzerland and France was made special every time I spent time with him. He really took the time to show me why each component of an LArTPC exists in a way that made me appreciate my work that much more. Thank you for the hours of Zoom calls, the countless lessons that were necessary for me to understand how to approach the analysis, and the things I just did not learn from the education system. Our conversations always ended with my brain making more connections both in making analysis code and understanding hardware. Not just in physics, but food as well. Bread and cheese, then British cookies with coffee. I am super grateful for your and Ruth Porde's hospitality during my ruptured finger accident. My recovery was speedy thanks to the care both of you gave me.

Additionally, I would like to thank the ICARUS collaboration at Fermilab for their support in my leadership role as a drift high voltage expert. Special thanks to Wooyoung Jang, Zachary Williams, Geoffrey Savage, Matthew Micheli, Linda Bagby, and Antonio Gioiosa for their guidance in understanding the drift high voltage subsystems and their support during times when things just were not working, and I had no clue why. Work planning and test executions only went smoothly (most of the time) because of all the help I had from them. Being lost without them is an understatement. Also, thank you Wooyoung, as my understanding of the Monte Carlo code mechanics was also very much supplemented by you, in addition to how a detector sensitivity analysis works.

A big thank you to our UTA scanning team, Brad Brown, Rohit Raut, Samriddha Chakraborty, and Samuel Blanchard, for the preliminary scanning of data. Thank you,

Brad, for taking care of the scanning logistics and Rohit, for making scripts to aid in the process.

To my committee members Jonathan Asaadi, Ben Jones, Ramon Lopez, and Zdzislaw Musielak, as well as my academic advisor, Dr. Qiming Zhang, thank you for your support in my graduate physics education and patience during my long Ph.D. journey. Performing research is important for Ph.D. achievement, but it is only possible with the basics in the toolbox and the necessary encouragement to learn the basics.

Lastly, thank you to my friends and family from both California and Texas. My radio silence would go on for long periods of time, but I still had all of you checking up on me throughout my Ph.D. Thank you to Juan Cardenas for inspiring my curiosity in physics, sharing the craziest discussions that would lead us down the rabbit hole that was hours deep, and the random phone calls that were right on time. Thank you to Jesus Gonzales for checking up on me to make sure I am still going at it, not giving up, and giving me those linguistic lessons. Thank you, Godmother, Godfather, aunts, uncles, and cousins here in the United States and Mexico for emotional support.

Abstract

Boosted Dark Matter Search with the

ICARUS T-600 Detector at the Gran Sasso Underground Laboratory

Hector Carranza Jr., Ph.D

The University of Texas at Arlington, 2024

The quest to discover dark matter is one of the most pressing topics in modern physics. Evidence of gravitational anomalies is present at different cosmological scales, spanning the stability and rotation of galaxies to the overall density profile of the entire observable Universe. Due to the discrepancy between the mass measured and the gravitational influence on the mass, if General Relativity is to correctly describe gravity at different scales, extra electromagnetically invisible matter termed dark matter must exist. In recent decades, many experiments have been performed to detect dark matter with masses that span many orders of magnitude, from Mass Compact Halo Objects (MACHOs) with masses several orders of magnitude that of our sun to very light particles on the order of $\sim \mu$eV. However, experiments have only been able to constrain the possible parameter space of dark matter models and, in general, probe dark matter models with single constituent dark matter like Weakly Interacting Massive Particles (WIMPs). In the Boosted Dark Matter (BDM) paradigm, there are four particles in the dark sector: χ_0, χ_1, χ_2, and the dark photon X. WIMP-like properties are ascribed to χ_0 to describe the physics of the gravitational anomalies, while relativistic components are assigned to χ_1 and χ_2. The inelastic boosted dark matter (iBDM) channel

$\chi_1 e^- \to \chi_2 e^- \to \chi_1 X e^- \to \chi_1 (e^+ e^-) e^-$, where χ_2 is an excited state of χ_1, has a unique signature that is distinguishable from neutrino interactions, making neutrino experiments a viable search environment for BDM. Using data collected by the ICARUS collaboration with ICARUS T-600 Liquid Argon Time Projection Chamber (LArTPC) during its operation at the Gran Sasso Underground Laboratory (LNGS), the first-ever LArTPC dark matter search using the ICARUS detector is presented. With a total detector exposure of 0.13 kton·year, a total of 4 iBDM candidate events were identified by several stages of data scanning. All were rejected due to defined selection criteria and a wire-by-wire dE/dx evaluation, giving a null result. Exclusion plots at 90%C.L. for the dark photon (m_X, ϵ) parameter space for fixed (m_0, m_1, m_2) DM mass sets are presented, setting new limits on the dark photon visible decay parameter space.

List of Figures

List of Tables

Contents

Chapter 1

Evidence for Dark Matter

Physics has been successful in identifying the laws of nature. The two overarching theories humanity has developed are Einstein's General Theory of Relativity (GR) [1,2] and Quantum Mechanics (QM) [3]. Our understanding of the Universe at the largest of scales comes from GR, describing gravitational dynamics and indicating the need for extra dark matter (DM) at all cosmological scales. QM allows for the quantitative understanding of the microscopic Universe, containing the mathematical tools to calculate subatomic interactions.

GR is fundamentally a deterministic theory, where the position and velocity of particles, stars, and galaxies can be determined simultaneously, and the equations that define the Universe take smooth, continuous values. On the other hand, QM is a theory that describes the world based on probabilities and does not allow for the simultaneous knowledge of the velocity and position of a particle, describing light and matter as being both a particle and a wave. As a consequence of imposing these characteristics on light and matter, the possible states of a system become discrete rather than the smooth, continuous nature of GR. Despite these fundamental differences, there are regions of the Universe where the two theories semi-work together. For example, the stability of stars, like our Sun, depends on the inward gravitational pressure balanced by the outward pressure of nuclear fusion reaction [4, 5]. Similarly, fermion degeneracy produces a kind of pressure that prevents neutron stars from

fully collapsing under the force of gravity [4].

The search for dark matter (DM) is, in fact, an interdisciplinary endeavor. All of our current evidence for it is gravitationally supported. Proof of any other interaction between ordinary matter and DM has yet to be recorded. However, the current understanding of the Big Bang suggests that DM had a significant role when it comes to seeding the current large scale structure of the Universe. In addition, the most modern and accurate use of QM is Quantum Field Theory, the fundamental framework for humanity's most successful model of particle physics called the Standard Model. The Standard Model contains all known particles and their interactions. However, none of these particles seem to fit the bill of DM, in the best case, only able to comprise a fractional of the total estimated DM in the observable Universe.

In this chapter, we will present some of the cosmological evidence of DM through gravitational signatures. The goal is to show the various evidence for DM's existence and what this evidence implicitly imposes on its bulk properties. The bulk properties will provide the basic ingredients for the construction of DM particle models that will be discussed in Ch. 2.

1.1 Zwicky and the Coma Cluster

Fritz Zwicky has coined the creator of the term "dark matter." His paper in Ref. [6] and also Stefano Profumo's book on possible particle properties of DM in Ref. [7] discuss the calculation of matter necessary to cause the dynamics of the Coma cluster. Zwicky studied the motion of the galaxies or "nebulae" in the Coma Cluster to understand the amount of matter in the cluster. Focusing first on individual nebulae i, Newton's second law reads

$$m_i \frac{d^2 \overrightarrow{r_i}}{dt^2} = \overrightarrow{F_i}. \tag{1.1}$$

Multiplying each side with r_i via the scalar product and noting that

$$\frac{d^2}{dt^2}\left(\overrightarrow{r_i}^2\right) = 2\left[\left(\frac{d\overrightarrow{r_i}}{dt}\right)^2 + \overrightarrow{r_i}\cdot\frac{d^2\overrightarrow{r_i}}{dt^2}\right] \rightarrow \overrightarrow{r_i}\cdot\frac{d^2\overrightarrow{r_i}}{dt^2} = \frac{1}{2}\frac{d^2}{dt^2}\left(\overrightarrow{r_i}^2\right) - \left(\frac{d\overrightarrow{r_i}}{dt}\right)^2 \tag{1.2}$$

The differential equation for the entire nebula cluster can be expressed as

$$\frac{1}{2}\frac{d^2}{dt^2}\left(\sum_i m_i\overrightarrow{r_i}^2\right) = \sum_i\left[\overrightarrow{r_i}\cdot\overrightarrow{F_i} + m_i\left(\frac{d\overrightarrow{r_i}}{dt}\right)^2\right]. \tag{1.3}$$

The two terms on the right side of eq. 1.3 are the virial and twice the kinetic energy of the nebula cluster, respectively. The quantity in parentheses on the left side of the equation is the nebula cluster's polar moment. Assuming that the cluster is stationary, and therefore the polar moment oscillates around a constant value, the time average of the change of the polar moment over time is essentially zero. Defining the potential and kinetic energy terms

$$U_{tot} = \sum_i \overrightarrow{r_i}\cdot\overrightarrow{F_i} \quad and \quad T_{tot} = \sum_i \frac{1}{2}m_i\left(\frac{d\overrightarrow{r_i}}{dt}\right)^2 \tag{1.4}$$

and time averaging eq. 1.3, the outcome is the *virial theorem*

$$-\langle U_{tot}\rangle_\tau = 2\langle T_{tot}\rangle_\tau. \tag{1.5}$$

The potential energy of the system is completely gravitational, therefore

$$U = -\sum_{i<j} G_N\frac{m_i m_j}{r_{ij}}. \tag{1.6}$$

Approximating the mass distribution of the nebula as uniform with a total mass M_{tot} and a radius R_{tot}, the mass of the cluster can be integrated with the distribution and arrive at the collective potential of the Coma cluster

$$U = -G_N\frac{3M_{tot}^2}{5R_{tot}}. \tag{1.7}$$

The kinetic energy term can be averaged over time and velocities (we will denote this double average as a double bar over the v, following the notation in [7])

$$\sum_i m_i \overline{v_i^2} = M_{tot} \overline{\overline{v_i^2}}. \tag{1.8}$$

The velocity used by Zwicky was the *line-of-sight velocity* of a nebula and this velocity is measured by using the Doppler shift of the nebula. The line-of-sight velocity is 1/3 the radial velocity. An explicit form for the total mass M_{tot} can now be expressed as

$$M_{tot} = \frac{10 R_{tot} \overline{\overline{v^2}}}{3 G_N}. \tag{1.9}$$

The numerical factor 10/3 is influenced by the physical distribution of the nebulae/galaxies. Therefore, the conservative option for a quantitative estimate is to take the order of magnitude for eq. 1.9.

Zwicky applied this formulation to the Coma cluster and obtained a mass-to-light ratio of around 500 [6]. With modern measurements and a refined galaxy distribution measurement, the mass-to-light ratio is closer to 400. This result is significant compared to the ratios found in other clusters, differing about two orders of magnitude [7]. The discrepancy between measured mass and observed mass at this scale, which is at the scale of galaxy clusters, brings into question whether this measured-to-seen mass difference appeared at other scales, such as galaxies, or on the opposite extreme of the structure of the overall observable Universe. In the remaining sections of this chapter, a brief exploration of the various mass measurements across various scales is presented, showing evidence of gravitational anomalies.

1.2 Gravitational Anomalies in the Universe

Zwicky's analysis of the Coma cluster dynamics opened the possibility that DM could be influencing the dynamics of the Universe at larger or smaller scales. The Coma Cluster

analysis came at a time when the science community was shown evidence that Einstein's General Theory of Relativity (GR) is the correct description for gravity.

According to GR, space and time merge to become space-time, and the transformations that enable the laws of physics to be invariant from one inertial reference frame to another are Poincare invariance [8]. This is in contrast to Newtonian mechanics, as the equations that govern the laws of physics obey Galilean transformations. The force of gravity is matter and energy responding to a non-flat space-time, where curvature creates deviations from a straight path. This is encapsulated in Einstein's field equations, which take the form [2, 9]

$$R_{\mu\nu} - \frac{1}{2}Rg_{\mu\nu} = 8\pi G_N T_{\mu\nu} \tag{1.10}$$

where $R_{\mu\nu}$ is the Ricci curvature tensor, R is the Ricci scalar, $g_{\mu\nu}$ is the metric, and $T_{\mu\nu}$ is the energy-momentum tensor. The left side of the equation describes the curvature of space-time, and the right-hand side describes the matter content in space-time. In general, the field equation deceives the reader with its visual simplicity, hiding the fact that it contains 10 partial differential equations, with 6 of those being independent.

With different curvature characteristics of space-time defined by the metric $g_{\mu\nu}$, the path $x^\mu(\lambda)$ that matter takes to traverse the space-time is the "shortest distance" between the beginning and end of the path called a geodesic. These paths are given by the geodesic equation

$$\frac{d^2x^\mu}{d\lambda} + \Gamma^\mu_{\rho\sigma}\frac{dx^\rho}{d\lambda}\frac{dx^\sigma}{d\lambda} = 0. \tag{1.11}$$

where $\Gamma^\mu_{\rho\sigma}$ is the Christoffel symbol, which encodes the information about the curvature of the space-time under consideration. Its expression takes the form

$$\Gamma^\mu_{\rho\sigma} = \frac{1}{2}g^{\sigma\rho}(\partial_\mu g_{\nu\rho} + \partial_\nu g_{\rho\mu} - \partial_\rho g_{\mu\nu}) \tag{1.12}$$

Using the metric, Einstein's field equations and the geodesic equation give the motion of

particles under the influence of gravity.

It should be noted that the geodesic equation is true for both massive and massless particles. This fact led to the first prediction of GR: light bends around massive objects due to the object's gravitational influence. The bending of light creates a *lensing effect*, which is appropriately termed *gravitational lensing*. Based on equation 1.10, the amount of lensing depends on the mass density distribution of matter in the region of space under investigation.

There is *strong gravitational lensing* and *weak gravitational lensing*, the latter of which can be approximated by perturbing the Newtonian limit of the field equations. In this limit, with the metric convention $(+---)$, the metric reads [2]

$$ds^2 = \left(1 + 2\frac{\Phi}{c^2}\right) dt^2 - \left(1 - 2\frac{\Phi}{c^2}\right) (dx^2 + dy^2 + dz^2) \tag{1.13}$$

where the potential obeys the usual Poisson equation

$$\nabla^2 \Phi = 4\pi G_N \rho. \tag{1.14}$$

where ρ is the mass density and $\nabla = (\frac{d}{dx}, \frac{d}{dy}, \frac{d}{dz})$. The weak-field metric contains extra terms that supplement correction to Newtonian gravity. These include terms that correct for the perihelion of Mercury and the deviation of light from distant objects due to the Sun's gravitational field [2].

Gravitational lensing is light being deflected from its straight path, bending due to massive sources changing the space-time metric. As seen in eq. 1.11, the metric defines the geodesic paths. Defining a deflection of light by an angle $\hat{\alpha}$, and noting that the original photon path $x^{(0)\mu}(\lambda)$ is perturbed by $x^{(1)\mu}(\lambda)$ and hence the path has a new form

$$x^\mu(\lambda) = x^{(0)\mu}(\lambda) + x^{(1)\mu}(\lambda). \tag{1.15}$$

Light travels along null ($ds^2 = 0$), hence

$$g_{\mu\nu}\frac{dx^\mu}{d\lambda}\frac{dx^\nu}{d\lambda} = 0. \tag{1.16}$$

Plugging in equation 1.15 and combing to first-order effects (the zeroth order is just the photon traveling in a completely straight line), the result with the geodesic equation leads to the deflection angle formula [2]

$$\hat{\alpha} = 2\int \vec{\nabla}_\perp \Phi \; ds \tag{1.17}$$

where ds is the physical distance traversed by the light. This equation works at a very simple, static Universe level. However, as previously seen, the effect of DM is seen at galactic scales, and it is at this scale that gravitational lensing will make sense. There is evidence that the Universe is expanding (in fact, this expansion is *accelerating*) and, therefore, the above formulation needs to be enhanced via some expansion scale factor $a(t)$. In literature, the metric that describes this is called the Friedmann-Robertson-Walker metric and, in spherical coordinates, takes the form [9]

$$ds^2 = c^2dt^2 + a^2(t)\left[\frac{dr^2}{1 - kr^2/R_0^2} + r^2d\Omega^2\right] \tag{1.18}$$

where $k = 0, 1, -1$ (flat, spherical, and hyperbolic Universes respectively), r is called the comoving coordinate (the physical observable distance is scaled by $r_{obs} = a(t)r$), and R_0 is the radius of the expanding space-time sphere. For the Universe in which we currently live, k is very close to 1, meaning our Universe is a nearly flat expanding space-time. The scale factor $a(t)$ has a direct effect on the measurement of distant cosmological objects. The light of objects moving away from an observer will look red-shifted due to the expansion of space, "stretching" the emitted light to have a longer wavelength λ. The amount of stretching can

be quantified with the expression

$$\lambda_0 = \frac{a(t_0)}{a(t_1)}\lambda_1 \tag{1.19}$$

where λ_0 is wavelength at the observer and λ_1 is the wavelength at the source. The definition of redshift can now be presented as

$$1 + z = \frac{1}{a(t_1)}. \tag{1.20}$$

This formula can be understood with the example of $z = 1 \rightarrow a(t_1) = 1/2$. This means if an observer looks at an object at redshift $z = 1$, the light emitted was at a "time" when the object was 1/2 its current size.

Gravitational lensing is a way to understand the mass distribution in a region of space-time, and the lensing is defined by how the light from objects is distorted and "misplaced" relative to where the objects are expected to be. Due to the Universe not being static, care must be taken in order to accurately determine distances when the determining factor is light emitted from a distant object. Defining, for now, χ as the *comoving* distance from a source and the observer of the source, we get that the observed flux of light as

$$F = \frac{L}{4\pi\chi^2} \tag{1.21}$$

where L is the luminosity. The comoving distance χ for a defined expanding space-time can be rewritten in the form

$$F = \frac{L}{4\pi d_L^2} \tag{1.22}$$

where d_L is the luminosity distance

$$d_L(z) = (1 + z)d_M(z) \rightarrow d_M = f(\chi)/R_0 \tag{1.23}$$

d_M is called the metric distance and is defined by the curvature of the expanding space-time.

At times, objects have a defined physical size and are referred to as *standard candles*. This means the object would have a defined size D and would take up an angle θ in the sky

$$sin(\theta/2) = \frac{D/2}{a(t_1)d_M} \tag{1.24}$$

this can be simplified in the small angle limit (which is valid given the distances between cosmological objects)

$$\theta = D/d_A \quad (\theta << 1rad) \tag{1.25}$$

where here we define the important quantity for calculating the distance to objects called the *angular diameter distance*

$$d_A = \frac{d_M(z)}{1+z}. \tag{1.26}$$

The results here defining how to calculate distances are what separate a static Universe (Minkowski metric) from an expanding one (FRW metric). Not only is the gravitational lens the cause for a change in the emitted light from an object, but the stretching of space-time also has an effect. In general, the warping of the light source (shear, twisting, and magnification) can be described by matrix [2, 10]

$$A_{ij} = \frac{\partial \beta^i}{\partial \theta^j} \tag{1.27}$$

Where β is the angle to the source and θ is the angle to the image. In this case, instead of just a point source as the lens, there is a *lensing potential*. Therefore, A_{ij} encodes the information of the *lensing map*.

The cosmology presented here is the basic technique used to measure effects in the Universe and discover that in order for the observed dynamics to exist, there must be some missing matter.

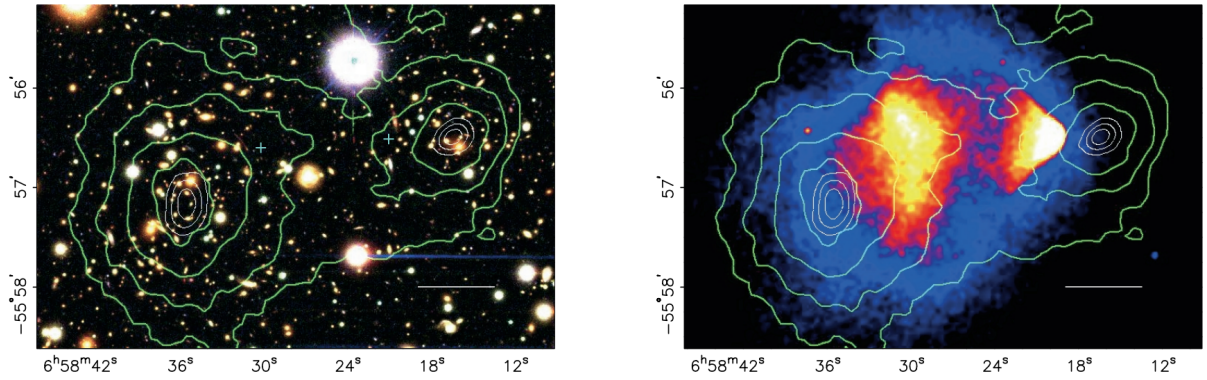

Figure 1.1: This figure shows the image of the Bullet Cluster with mass density contours (left), and the contours with a visible mass show with the red and yellow color and invisible mass shown in blue [11]. The contours are derived from the weak lensing magnification κ reconstruction (green lines).

1.2.1 Merger Cluster 1E 0657-558: The Bullet Cluster

The next cluster to shine a light on this gravitational problem was the *Bullet cluster* [11]. This time, instead of studying the movements of the galaxies in the cluster, this study focuses on how light is distorted along the map of the cluster. This links back directly to the previous discussion about weak gravitational lensing and the construction of the Bullet cluster lensing map. The matrix A_{ij} for this analysis takes the form [2, 10]

$$A = \begin{pmatrix} 1-\kappa+\gamma_1 & \gamma_2 \\ \gamma_2 & 1-\kappa-\gamma_1 \end{pmatrix} = (1-\kappa)\begin{pmatrix} 1+g_1 & g_2 \\ g_2 & 1-g_1 \end{pmatrix} \rightarrow \quad g_i = \frac{\gamma_i}{1-\kappa} \tag{1.28}$$

where κ is called the convergence, γ_1, γ_2 are the shear, and g_i is the reduced shear. The convergence measures the size change of the object image, and the shear measures the shape change of the image. κ is also termed the *dimensionless mass density*, and therefore, measuring the convergence allows for the measurement of the mass distribution for a given lensing potential. The reduced shear of the image was first calculated, then subsequently the convergence. In Fig. 1.1, the mass distribution is shown for the Bullet Cluster. The mass distribution is formed from two galactic clusters colliding. The green contours show the

reconstruction of κ, which can then be used to reconstruct the mass distribution. Surveying the area for X-rays reveals the portion attributed to baryonic matter (red-yellow), while the portion that is "dark" (shown as the blue region in Fig. 1.1) is hypothesized to be DM. This claim is substantiated because these portions are at the extremities of the distribution, where *nearly* collisionless matter during a merger would extend. Assuming the existence of DM in the Bullet cluster, a limit on the DM self-interaction cross section can be obtained [12]

$$\sigma_{\chi\chi}/m_\chi < 1cm^2\ g^{-1}. \tag{1.29}$$

This self-interaction cross-sectional measurement serves as crucial information on the particle properties of DM and puts bounds on the parameter space of DM theories.

1.2.2 Non-Keplerian Galaxy Velocity Distribution

The velocity distribution of galaxies indicates a significant deviation from the currently understood theory. Using Newton's law of gravitation with the expression of centripetal acceleration, the expression for rotation velocity is

$$v_c(r) = \sqrt{\frac{G_N M}{r}} \quad (r > R) \tag{1.30}$$

for a mass distribution contained within a radius R. Outside the center of a galaxy, where most of the mass is concentrated, the expectation is $v_c \sim r^{-1/2}$. Assuming a spherical galaxy, and therefore a mass distribution $M(r) = \frac{4}{3}\pi r^3 \rho$, the velocity within the galactic center becomes

$$v_c(r) = \sqrt{\frac{4\pi G_N \rho}{3}} r \quad (r \leq R). \tag{1.31}$$

The red-shift and blue-shift of the various rotating objects can be calculated, and in turn, the velocity of objects rotating within a galaxy and the mass distribution can be obtained. The outcome of analyzing the velocity distribution of various galaxies indicates that the

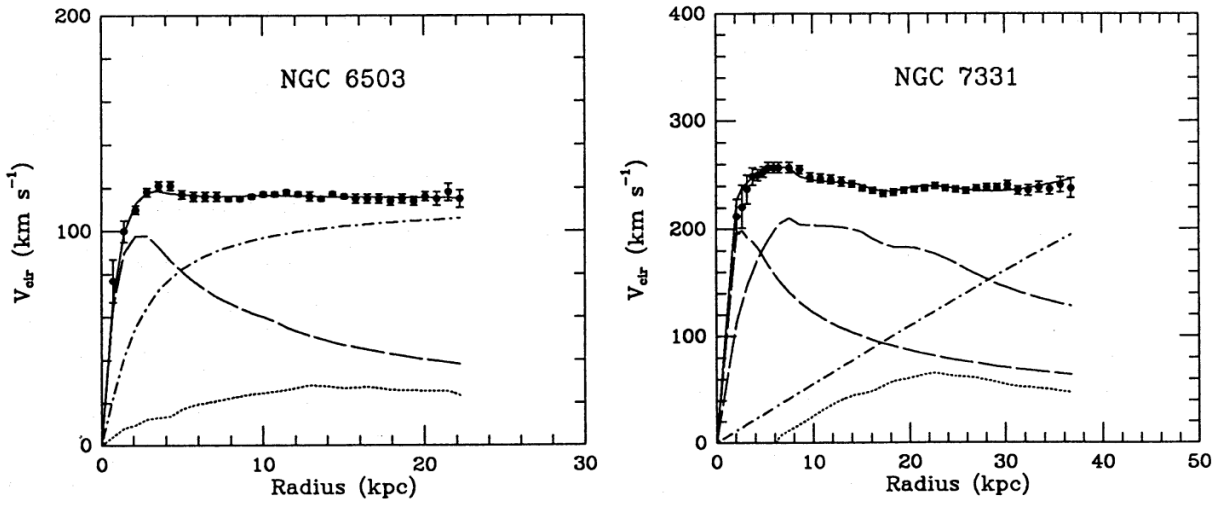

Figure 1.2: Radial Velocity measurement as a function of radial distance from the center of galaxies [13]. The Two graphs correspond to two different galaxies. The long dashed lines indicate what would be expected if the luminous matter in the galaxy was the only factor. It is clear from the data points that this is not the case for both galaxies, and evidence for a DM halo exists with a distribution model with equation 1.32.

expected velocity fall-off away from the galactic center is non-existent. Instead, the velocity approaches a constant value outside the galactic center. This is evident in Fig. 1.2. The data points are represented by the black points, and the fit line that goes through the points is modeled by an isothermal sphere of matter usually referred to as the DM Halo. This gravitational anomaly leads to the possibility of the existence of a DM halo around galaxies in order to compensate for the absence of visible, baryonic matter to explain the constant circular velocity. The halo distribution is modeled as [13]

$$\rho(r) = \rho_0 \left[1 + \left(\frac{r}{r_c} \right)^2 \right]^{-1} \tag{1.32}$$

where ρ_0 is the central halo density and r_c is the halo core radius. The result of implementing the above is shown by the solid black line being in very good agreement with the data in Fig. 1.2 for the two galaxies NGC 6503 and NGC 7331 [13]. The line with long dashes indicates what the velocity distribution should look like if galaxy rotational dynamics followed Newton's universal law of gravitation. This curve is typically referred to as the Keplerian

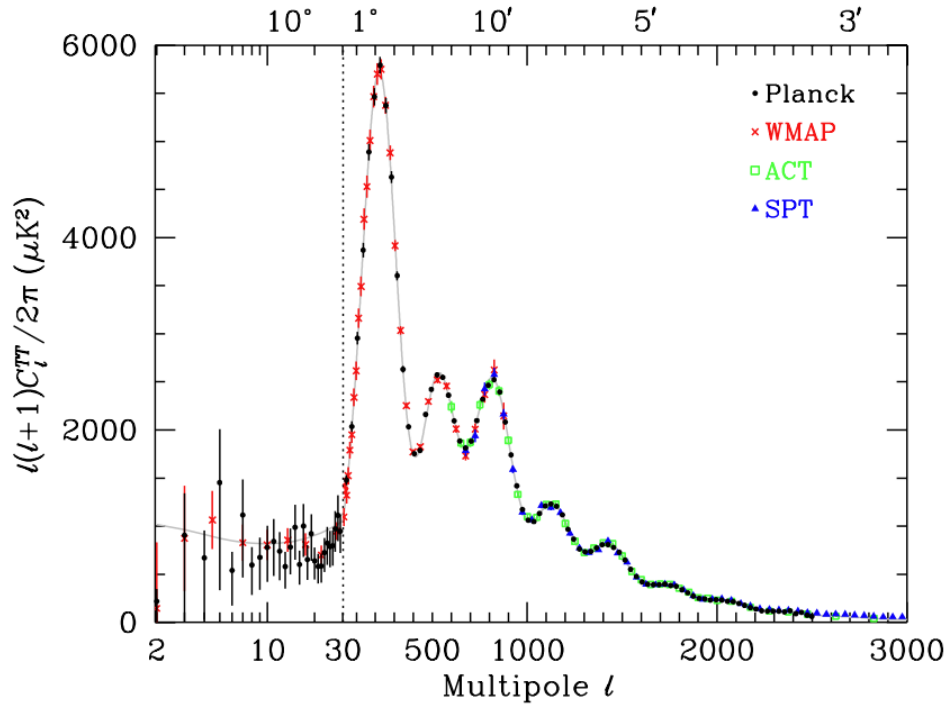

Figure 1.3: The power spectrum of the Cosmic Microwave Background (CMB) [14]. The different colored points are measurements from the various experiments indicated in the legend. The points are fitted via the coefficients of Eq. 1.33.

velocity curve.

1.2.3 Cosmic Microwave Background Distribution

Even though FRW metric takes into account the expansion of the Universe, the expansion is homogeneous. The Universe paints a different picture when looking at the *cosmic microwave background*(CMB), showing density fluctuations at the grandest of scales. When the Universe was just seconds old, it was hot and dense and, therefore, a plasma. Plasma is a hot, dense state of matter consisting of free electrons and nuclei.

As the Universe expanded and cooled, particle species began to decouple from the hot, dense plasma as the expansion rate matched the interaction rate that kept the species coupled to the expanding thermal bath. There was a point in the expansion called *recombination* [9], where the Universe cooled down to a point where electrons and protons had the chance to

settle down and form hydrogen via $e^- + p \rightarrow H + \gamma$. The way photons stayed coupled to the expanding thermal bath was primarily via *Thomson scattering* $e^- + \gamma \rightarrow e^- + \gamma$ [9]. Since recombination reduces the number of free electrons, the interaction rate is reduced, and eventually, photons decoupled from the thermal bath. These are the photons responsible for the CMB. This means these photons have information about the Universe during the photon decoupling period when the Universe was $\sim 370,000$ years old. The scale factor $a(t)$ can then be used to figure out the surface of last-scattering for the photons. The CMB map is created via the analysis of photons from this surface.

Due to the spherical symmetry of the CMB (although the CMB has anisotropies, these deviations from homogeneous are randomly distributed in the sky), the temperature fluctuations can be modeled with spherical harmonics [9]

$$\frac{\delta T}{T} = \sum_{l=2}^{+\infty} \sum_{m=-l}^{+l} a_{lm} Y_{lm}(\theta, \phi) \tag{1.33}$$

where T is the average CMB temperature today. The power spectrum is achieved by comparing the temperature variation at two distinct points in the sky via what is called a two-point correlation function

$$\begin{aligned} C(\theta) = \langle \delta(\hat{n}) \delta(\hat{n}') \rangle &= \sum_{ml} \sum_{m'l'} a_{ml} a^*_{m'l'} Y_{lm}(\hat{n}) Y_{l'm'}(\hat{n'}) \\ &= \sum_{l} \frac{2l+1}{4\pi} C_l P_l(cos\theta) \end{aligned} \tag{1.34}$$

where $P_l(cos\theta)$ are the Legendre polynomials. The formulation is the *multipole expansion* of the CMB power spectrum. The coefficients C_l are proportional to the power spectrum, hence the literature usually graphs C_l *vs* l as seen in Fig. 1.3.

This approach is phenomenological in the sense that the two-point correlation function relating the temperature variations in two different points in space was fitted to understand C_l. This means all the physics that goes into the the power spectrum is coded into the spherical

harmonic coefficients. Looking at the different points in which particle species decouple from the early Universe plasma, recombination effects, along with space-time curvature effects tell part of the power spectrum story.

The peaks of the spectrum are subject to the amount of matter and its density [9]. Using only baryonic matter as the matter component for the power spectrum peaks does not reproduce the observed data. Introducing another matter and possibly another energy component has been successful in describing the observed CMB power spectrum while also building upon the other observation of missing mass. The model used is termed the ΛCDM (cosmological constant + cold dark matter). The cosmological constant Λ is used to describe the acceleration of the expansion of space-time. The entity tied to this expansion is termed *dark energy*.

CDM is the hypothesis that if DM exists, it moves as a non-relativistic fluid (cold) and influences the matter distribution in the early stages of the Universe, decoupling early on from the thermal bath in order for cosmological substructures to form. CMB measurements have obtained measurements for the various species densities over the critical density ($\Omega_{DM} + \Omega_b + \Omega_r + \Omega_k + \Omega_\Lambda = 1$) [15, 16]

$$\begin{aligned} \Omega_r &= (9.02 \pm 0.21) \times 10^{-5} \\ \Omega_b &= 0.0493 \pm 0.0006 \\ \Omega_m &= 0.3153 \pm 0.0073 \\ \Omega_\Lambda &= 0.6847 \pm 0.0073 \\ |\Omega_k| &< 0.005 \end{aligned} \tag{1.35}$$

where $\Omega_m = \Omega_b + \Omega_{DM}$ and hence

$$\Omega_{DM} \sim 0.27. \tag{1.36}$$

The main takeaway is that visible matter only makes up $\sim 5\%$, while dark matter and dark energy make up the majority of the energy density of the Universe $\sim 95\%$. The amount

of baryonic matter is in line with the theory of Big Bang nuclear synthesis (BBN) [17], which describes the mechanism by which heavy nuclei formed in the earlier stages of the Universe where there were yet to be stars.

1.3 Stellar Objects as Dark Matter

Before diving into the next chapter to discuss particle theories of DM, there are two stellar objects that have been theorized as the explanation for the perceived gravitational anomalies: Massive Compact Halo Objects (MACHOs) and Primordial Black Holes (PBHs).

1.3.1 MACHOs

MACHOs are thought to be composed of "dark baryons". The amount of possible dark baryon population is constrained by CMB data and BBN constraints; therefore, it cannot make up all of Ω_{DM}. The idea is that big, dense objects like balls of gas that have not formed stars, brown dwarfs, or anything planetary in size might be able to make up the dark halo in galaxies. A way to verify this was to look at stars from galaxies and wait for a *microlensing* event. In this case, the MACHO is theoretically smaller than the star it would pass in front of, making the brightness of the star appear magnified. The size and mass of the MACHOs are constrained by the stability of galaxies. In order to determine the density of dark halo along a line-of-sight distance, the *optical dept* $\tau(t)$ is needed [9]

$$\tau(t) = \int_t^{t_0} \Gamma_\gamma(\bar{t})\ d\bar{t} \tag{1.37}$$

where $\bar{t}$ is just an integration variable not an average, t_0 is the present and t is at a different scale a(t). The rate is defined as

$$\Gamma = \eta\sigma v \tag{1.38}$$

Since the goal is to see dark objects pass in front of stars, gravitational lensing, in this case, creates what's called an *Einstein ring*. The microlens radius for the ring is defined as [2]

$$R_E = \sqrt{\frac{4GMd_{LS}d_L}{c^2 d_S}} \tag{1.39}$$

where the set d_i are angular diameter distances with the subscripts meaning lens to the source (LS), observer to the lens (L), and observer to source (S). Noting that the cross-section is microlens area $\sigma = \pi R_E^2$, and the number density along the line-of-sight is $\rho(d_L)$, the final expression for optical dept becomes

$$\tau(t) = \int_0^{d_S} \rho(d_L)\pi R_E^2 \; d(d_L). \tag{1.40}$$

The optical depth is very model-dependent due to the assumption of the dark halo distribution mass distribution. Identifying microlensing events is difficult due to variable stars as they mimic the signature of the microlensing event. This can affect the. The OGLE-III [18] and MACHO experiment [19,20] data on the Magellanic Clouds has set a $16\% - 22\%$ limit on the amount of dark halo matter MACHOs can compose with a mass range of the MACHO population ranging $0.1 - 0.9M_\odot$, where $M_\odot$ is a solar mass. The range exists because of the model-dependent nature of the dark halo. These experiments show that MACHOs can compose a significant percentage of DM, but not 100%.

1.3.2 Primordial Black Holes

Primordial black holes are black holes that formed back in the early days of the Universe. If matter coalesces in a volume of space in which the mass exceeds the Chandrasekhar mass, a black hole forms. Depending on the cosmological model used, primordial black holes can be in abundance. Of course, this must be controlled as if they existed in large quantities, accretion disks would be more abundant, and stellar evolution would be greatly impacted. The limit on the macroscopic mass of dark matter (specifically big masses like primordial

black holes of MACHOs) is $m > 10^6 M_\odot$, as greater masses would disrupt the disk structure of galaxies [20]. Also, if these massive objects were flinging around like projectiles, star systems in the dark halos would be more chaotic.

1.4 Lessons Learned from Cosmology

There are three main lessons about DM that can be taken from its cosmological evidence:

- DM is Dark. The evidence for its existence is purely gravitational. However, this does not rule out the possibility of having an electric charge. Models that allow DM to have electromagnetic interactions include milli-charge particles or, in the case of this dissertation, dark sector gauge boson portals (e.g., the dark photon) to the Standard Model Photon.

- DM is Semi-Collisionless. The mass density distribution of the bullet cluster shows that if the extra mass density on the edges of the contour map is attributed to dark matter, the galaxy cluster merger dynamics puts limits on DM self-interaction cross section as $\sigma_{\chi\chi}/m_\chi \leq 1\ cm^2/g \sim 0.1\ GeV^{-2}$.

- DM Propagates Non-relativistically Presently. This is the basis for the ΛCDM model and has great success in explaining the power spectrum of the CMB. Also, for sub-structures to form, gravitational wells need to form, and therefore, DM has to have a more clumpy property. This is possible with CDM.

Chapter 2

Particle Dark Matter

The cosmological properties of DM have been obtained by analyzing the dynamics of the cosmos at different scales. The success of the ΛCDM hypothesis at explaining the gravitational anomalies at various scales has in some way biased the community into thinking DM is the only way forward. However, one thing is understanding the bulk properties of a system, and another thing entirely is understanding what that system's fundamental particle constituents are. If DM is truly the answer to the observed gravitational anomalies, the DM particle(s) must be detected in an experiment. The cosmological measurements give a starting point. However, this constraint still leaves the mass parameter to span several orders of magnitude, and other types of interaction apart from gravity are unknown. In this chapter, I will first present the Standard Model of particle physics and explain its shortcomings in terms of a candidate for DM. This will lead to a statistical mechanics analysis of cold dark matter and the particle properties necessary to explain the bulk cosmological properties. I will obtain the gross features that will lead to considering the weakly interacting massive particle (WIMP) model as a candidate to explain DM.

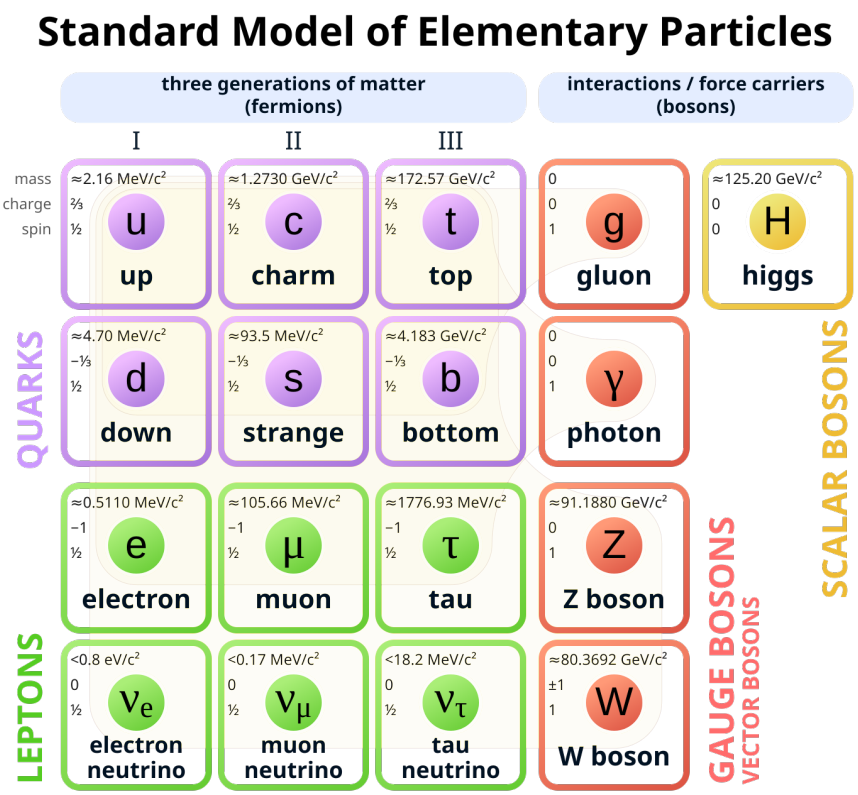

Figure 2.1: The Standard Model of Particle Physics. The fermion sector has a three-generational structure for the quarks and leptons. The gauge bosons are the product of invoking local symmetries via the U(1)(photon), SU(2)(Z and $W^{\pm}$), and SU(3)(gluons) groups. The Higgs boson is a scalar boson that was discovered in 2012 at CERN and completed the model. However, evidence in the neutrino sector and the absence of DM have called for theories beyond the standard (BSM).

2.1 Standard Model

Throughout the discussion in the chapter, I will assume the use of natural units $c = \hbar = 1$. The Standard Model (SM) is the most successful particle physics theory to date. At its foundation, the particle properties and their interactions are described by quantum field theory (QFT). Figure 2.1 shows the elementary particles of the SM. There are two classes, bosons and fermions. In terms of intrinsic differences, it's all in their spin property and

therefore, the Lagrangian for each is different

$$\begin{aligned}
(spin\ 0)\ \mathcal{L}_{scalar} &= \partial_\mu\phi\partial_\mu\phi^* + m^2\phi\phi^* \\
(spin\ 1/2)\ \mathcal{L}_{Dirac} &= \overline{\psi}(i\gamma^\mu\partial_\mu - m)\psi \\
(spin\ 1)\ \mathcal{L}_{proca} &= -\frac{1}{4}F^{(i)}_{\mu\nu}F^{\mu\nu}_{(i)} - \frac{1}{4}B^{(j)}_{\mu\nu}B^{\mu\nu}_{(j)} + \frac{1}{2}m^2X_\mu X^\mu
\end{aligned} \tag{2.1}$$

It should be noted that these are the free particle lagrangians, as interaction terms $\mathcal{L}_{int}$ stem from the procedure of gauge invariance. Gauge theory is what makes the SM volatile, allowing for interactions. Invoking local symmetries (e.g., U(1), SU(2), SU(3) group symmetries) and imposing the lagrangian be invariant under the symmetry introduce interaction terms that couple fermions to new fields. These fields correspond to the bosons in the SM, hence why they are termed *gauge bosons*. The effect can be qualitatively described as

$$\partial_\mu \rightarrow D_\mu = \partial_\mu + i(coupling(s)\ \cdot\ gauge\ field(s)) \tag{2.2}$$

and therefore the regular partial derivative ∂_μ gets promoted to a *covariant derivative* D_μ. In the case of the SM, there are three known forces electromagnetism, weak, and strong nuclear force. In the end the first two are unified to electroweak theory and the strong is described by quantum chromodynamics theory. The SM is described by the group structure $SU(2)_c \times SU(2)_L \times U(1)_Y$, where the subscript "c" means color, L means Left-hand, and Y is hypercharge. These are the symmetries that each group is describing. Quantum chromodynamics characterizes the color charge of the quarks in the strong interaction. The weak force only couples to left-handed particles and right-handed antiparticles, and there is an associated hypercharge for the electromagnetic interaction. This implies that the covariant derivative for the SM takes the form

$$D^{SM}_\mu = \partial_\mu - ig_1\frac{Y}{2}B_\mu - ig_2\frac{\sigma_i}{2}W^i_\mu - ig_3\frac{\lambda_a}{2}G^a_\mu \tag{2.3}$$

Where σ_i are the Pauli matrices and λ_a are the Gell-Mann matrices. The three generations of leptons, neutrinos, and quarks (along with their anti-particle counterparts) obey the Dirac equation, where the field is a 4-component spinor ψ. The photon γ, $W^{\pm}$, and Z^0 bosons follow the proca equation, with the exception of the mass term. This leads to the last boson, the Higgs. The Higgs is a goldstone boson (spin 0), hence follows the scalar Lagrangian with additional potential terms. The Higgs boson was more recently discovered at the Large Hadron Collider at the European Organization for Nuclear Research (CERN). It was the last missing piece to the SM puzzle as the Higgs allows for the spin 1 bosons $W^{\pm}$ and Z^0 to acquire mass in a gauge invariant way. The proca lagrangian in equation set 2.1 has a mass term that is not suitable for gauge invariance. To show this more simply, let us take the proca equation and specialize it for the very interesting massive photon case

$$\mathcal{L} = -\frac{1}{4}B_{\mu\nu}B^{\mu\nu} + \frac{1}{2}m^2 X_\mu X^\mu \tag{2.4}$$

if we make the transformation for the four-potential as

$$X_\mu \to X_\mu - \partial_\mu \beta \tag{2.5}$$

The field-strength term stays invariant, while the mass term becomes

$$\begin{aligned} \frac{1}{2}m^2 X_\mu X^\mu \to\ & \frac{1}{2}m^2 (X_\mu - \partial_\mu\beta)(X^\mu - \partial^\mu\beta) \\ & = \frac{1}{2}m^2 (X_\mu X^\mu - X_\mu(\partial^\mu\beta) - (\partial_\mu\beta)X^\mu + (\partial_\mu\beta)(\partial^\mu\beta)). \end{aligned} \tag{2.6}$$

This is clearly not returning to the original mass term, hence it is not gauge invariant. This was not an issue with the SM photon because it is massless. Also when looking at the strong interaction, which imposes SU(3) gauge symmetry, the gluons are massless and hence was not an issue. However, The weak interaction followed SU(2) gauge symmetry and resulted in the three spin 1 weak force carriers $W^{\pm}$ and Z^0. Experiments showed these bosons do

have mass, hence gauge invariance was not satisfied and hence the Higgs mechanism was discovered. To briefly describe how this applies since my analysis uses a massive photon (dark photon more on this later in the chapter), the Higgs field is introduced via

$$\begin{aligned}\mathcal{L} &= (\partial_\mu \phi)^*(\partial^\mu \phi) - V(\phi) \\ &= (\partial_\mu \phi)^*(\partial^\mu \phi) - \mu^2 \phi^* \phi - \lambda(\phi^* \phi)^2\end{aligned} \tag{2.7}$$

where the complex scalar field is defined as

$$\phi = \frac{1}{\sqrt{2}}(\phi_1 + i\phi_2). \tag{2.8}$$

It has a global U(1) symmetry. In terms of the real scalar fields, the equation reads

$$\mathcal{L} = \frac{1}{2}(\partial_\mu \phi_1)^2 + \frac{1}{2}(\partial_\mu \phi_2)^2 - \frac{1}{2}\mu^2(\phi_1^2 + \phi_2^2) - \frac{\lambda}{4}(\phi_1^2 + \phi_2^2)^2 \tag{2.9}$$

If we minimize the potential, we get the relationship

$$\phi_1^2 + \phi_2^2 = \frac{-\mu^2}{\lambda} = \upsilon^2 \tag{2.10}$$

which is the equation of a circle. This means the range of minimum values lies on a circle of radius υ. At this point, the system is exhibiting symmetry at the minimum. This can be seen visually in Fig. 2.2. This changes once there is a perturbation of the field, kicking it out of the minimum. The point at which the field is perturbed does not matter, hence picking the point

$$\phi_1 = \upsilon, \phi_2 = 0 \rightarrow \ \phi = \upsilon + h(x) + i\rho(x) \tag{2.11}$$

where $h(x)$ and $\rho(x)$ are the perturbation amount from the minimum. Applying this point

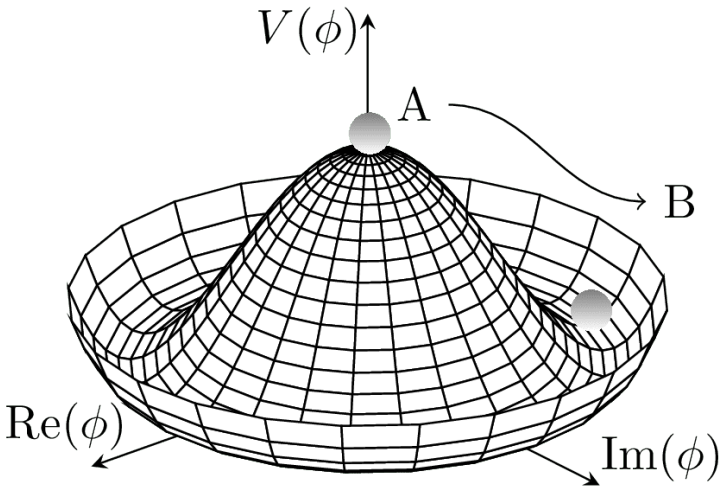

Figure 2.2: The "Mexican Hat" potential. The symmetry is evident when the Higgs boson is in the ground state at the bottom of the potential. Once perturbed away from this minimum point, the global symmetry is spontaneously broken.

to the lagrangian results in the following

$$\mathcal{L} = \frac{1}{2}(\partial_\mu \rho)^2 + \frac{1}{2}(\partial_\mu h)^2 + \mu^2 h^2 - \lambda\eta(h\rho^2 + h^3) - \frac{\lambda}{2}h^2\rho^2 - \frac{\lambda}{4}h^4 - \frac{\lambda}{4}\rho^4 + \cdot\ \cdot\ \cdot \tag{2.12}$$

where the omitted terms are constants of η. On close inspection we can see a term that looks like mass if we identify $\frac{1}{2}m_h^2 = \mu^2 \rightarrow m_h^2 = 2|\mu^2|$. This is great news, since this means by "spontaneously breaking the symmetry" of being in the minimum state, a field h is introduced and acquires mass by traveling up the potential. Unfortunately, the global U(1) symmetry is lost here since we picked a ground state or "vacuum". In some sense, it is "hidden" since we wandered off to some perturbed path of the potential.

How does this apply to the photon? Applying the above formulation under a *local* U(1) transformation defining the covariant derivative

$$\partial_\mu \rightarrow \ D_\mu = \partial_\mu - igX_\mu \tag{2.13}$$

the photon gauge field transforms as

$$X_\mu \rightarrow \ X'_\mu = X_\mu - \frac{1}{g}\partial_\mu \beta(x) \tag{2.14}$$

and finally from previous discussions, knowing that ϕ is invariant with the above covariant and gauge transformation under its own transformation

$$\phi(x) \rightarrow \ \phi'(x) = e^{i\beta(x)}\phi. \tag{2.15}$$

Combining this all together, we have the U(1) invariant lagrangian

$$\mathcal{L} = (D_\mu \phi)^*(D^\mu \phi) - \mu^2 \phi^* \phi - \lambda(\phi^* \phi)^2 - \frac{1}{4} B_{\mu\nu} B^{\mu\nu}. \tag{2.16}$$

The advantage we have now is that the perturbation from the minimum $\upsilon + h(x) + i\rho(x)$ can be made only to contain the real part due to the fact that the $\rho(x)$ "fictitious" field can be removed by redefining the transformation B_μ(this means this field becomes the longitudinal component of the vector field, sometimes phrased as "the vector field ate the goldstone boson"), which means we are left with the identification

$$\phi(x) = \frac{(\upsilon + h(x))}{\sqrt{2}} \tag{2.17}$$

Plugging everything into the lagrangian, the relevant terms are

$$\mathcal{L}_{Xh} = \frac{1}{2}(\partial_\mu h)^2 + \lambda \upsilon^2 h^2 + \frac{1}{2} g^2 \upsilon^2 X_\mu X^\mu - \frac{1}{4} B_{\mu\nu} B^{\mu\nu} + \cdot \ \cdot \ \cdot \tag{2.18}$$

where the vector boson X_μ now has a mass term indicating $m_X = g\upsilon$. Later in the chapter, I will discuss the boosted dark matter model and its incorporation of a dark sector interaction portal with the dark photon. This photon is massive, and hence the Higgs mechanism is a way to give mass to this boson without breaking its new $U(1)_X$ local symmetry. This special

use of giving mass via the Higgs mechanism to a proca equation vector boson is called *The Stueckelberg Field* [21].

The SM of particle physics seems complete. There is an explanation for how the forces can be introduced via gauge invariance, and masses for massive particles can be given via the Higgs mechanism. However, one aspect not explained is the experimental evidence of neutrino oscillations. In fact, our first candidate to explore as a possible DM particle is the neutrino. Before doing so, let me review some statistical mechanics that will be instrumental in the connection between cosmological effects to particle properties.

2.1.1 Thermal Equilibrium and Freeze Out

Neutrinos participate in weak interactions. Their coupling to matter is very weak, which is an aspect that puts them as a possible DM candidate. It could be that neutrinos are all of the DM relic abundance, or possibly a percentage. The content of the universe that *seems* to be DM is understood from cosmological observations. The measurement that quantifies this amount is the abundance of DM $\Omega_{DM} \sim 0.27$. The goal for this section is to combine particle physics and cosmology and calculate the estimated abundance for neutrinos. For full details, use Ref. [9].

In order to obtain this value, we need to understand the thermodynamic properties of the universe at different times. Modeling all matter in the universe as a *perfect fluid*

$$T_{\mu\nu} = (\rho + P)U_\mu U_\nu + P g_{\mu\nu} \tag{2.19}$$

where ρ is the energy density, P is the pressure of the fluid, and U_μ is the relative four-velocity. Conservation of energy and momentum imposes $\nabla_\mu T^\mu{}_\nu = 0$, and the continuity equation can be written

$$\dot{\rho} + 3\frac{\dot{a}}{a}(\rho + P) = 0 \tag{2.20}$$

The equation of state is identified as $\omega = P/\rho$ we get

$$\frac{\dot{\rho}}{\rho} = -3\frac{\dot{a}}{a}(1+\omega) \longrightarrow \rho \sim a^{-3(1-\omega)} \tag{2.21}$$

Depending on the ratio of pressure of the fluid in the rest frame and energy density, the dependence of the energy density of the fluid on the scale factor can be understood. The first law of thermodynamics reads

$$TdS = dU + PdV - \mu dN \tag{2.22}$$

where μ is the chemical potential of a particle species. Defining the entropy density as $s = S/V$ and factoring all terms out leads to the equation

$$(Ts - \rho - P + \mu n)dV + V\left(T\frac{ds}{dT} + \mu\frac{dn}{dT} - \frac{d\rho}{dT}\right)dT = 0 \tag{2.23}$$

in order for the this equation to vanish and make sense, both quantities in parenthesis must vanish, hence for the first parenthesis

$$s = \frac{\rho + P - \mu n}{T} \tag{2.24}$$

and for the second

$$\frac{d\rho}{dT} = T\frac{ds}{dT} + \mu\frac{dn}{dT}. \tag{2.25}$$

Combining both of these with the continuity equation 2.20, noting that $Ts + \mu n = \rho + P$ gives

$$\frac{d}{dt}(sa^3) = -\frac{\mu}{T}\frac{d}{dt}(na^3) \tag{2.26}$$

If the temperature of the system is much greater than the chemical potential of the system or if the number density of the particles does not change in the expansion of the universe, the property of conservation of entropy is present in the comoving reference frame. This is

typically the case when a system is in equilibrium. The entropy here scales as a^{-3}. This expression is important because it relates the entropy density with the number density of particle species. The evolution of these two gives the quantitative answer of when a particle species "freezes out" from the Universe's thermal bath (falls out of thermal equilibrium).

In order to determine the number density of a species, we turn now to statistical mechanics. The probability distribution function $f(p,T)$ of a species dictates the likelihood of a system being in a particular state. I have written it in terms of just the momentum and temperature due to our assumption of thermal equilibrium (wait long enough, and it will get there). The spin of the particle dictates the *spin statistics*, which not only have consequences in the small scale of the Universe but also on the cosmological scale due to the distribution function each obeys

$$f(p,T) = \frac{1}{e^{(E(p)-\mu)/T} \pm 1} \tag{2.27}$$

where (+) is the fermion distribution and (-) is the boson distribution. To get the number density n, energy density ρ and pressure P, we have the relations

$$\begin{aligned} n(T) &= \frac{g}{(2\pi)^3} \int d^3p f(p,T) \\ \rho(T) &= \frac{g}{(2\pi)^3} \int d^3p f(p,T) E(p) \\ P(T) &= \frac{g}{(2\pi)^3} \int d^3p f(p,T) \frac{p^2}{3E(p)} \end{aligned} \tag{2.28}$$

where g is the number of internal degrees of freedom, for example spin states. Therefore, given our understanding of the SM and the possible interactions that can keep each species in equilibrium with the primordial plasma "soup", the freeze-out temperature can be calculated by calculating when the rate of the processes that keep a particle species in equilibrium becomes equal to the rate of expansion of space

$$T_{f.o} \rightarrow H(T_{f.o}) \sim \Gamma(T_{f.o}). \tag{2.29}$$

where H is the Hubble parameter $\dot{a}/a$. In other words, if the mean free path of the particle is larger than the size of the universe at a given time, the particle has effectively decoupled from the universe's thermal bath, and particles in general, free stream and the number density reduces proportionally to the expansion of spacetime (a(t)). The rate of a certain process a particle can have is defined by the probability of interacting with the medium it's traversing, the density of the medium, and the speed of the particle. More explicitly

$$\Gamma = n\sigma v. \tag{2.30}$$

The cross section σ contains the SM aspects. Depending on how the particle species couples to the interactions in the thermal bath. This means we must indicate the particle we want to analyze before proceeding.

However, the number density can be approximated already for fermion and bosons via the $f(p,T)$ probability distribution. Using the energy relation $E^2 = m^2 + p^2$, setting the chemical potential $\mu = 0$(thermal equilibrium condition) and going to spherical coordinates in the p phase space

$$n = \frac{g}{2\pi^2}\int_0^\infty dp \frac{p^2}{e^{\sqrt{p^2+m^2}/T} \pm 1} \tag{2.31}$$

This equation at the extreme limits can be evaluated analytically. The two extremes are the relativistic ($T \gg m$) case and the non-relativistic ($T \ll m$). Carrying out the integration leads to the relativistic number density

$$n_{bosons} = \frac{\zeta(3)}{\pi^2} g T^3 \ ; \ n_{fermions} = \frac{3}{4} n_{bosons} \tag{2.32}$$

Also, noting that for relativistic particles $E \sim p$, hence for a relativistic fluid the equation of state using P/ρ from equation 2.28 gives

$$P = \frac{1}{3}\rho. \tag{2.33}$$

Moving to the other extreme, for a non-relativistic particle species, the number density becomes

$$n = g\left(\frac{mT}{2\pi}\right)^{3/2} e^{-m/T}. \tag{2.34}$$

This equation is important as it directly pertains to cold dark matter! The equation of state of a slow moving fluid in equilibrium is just the ideal gas law

$$P = nT. \tag{2.35}$$

2.1.2 Important Example: Neutrino Hot DM?

Neutrinos out of all the particles in the SM interact the weakest. Their method of interacting with the other leptons is via the weak force either by the neutral current (Z^0 boson exchange) or charged current ($W^{\pm}$ boson exchange). This means that from an equilibrium stand point with primordial plasma of the universe, the interactions that kept the neutrino in equilibrium with said plasma was [7, 9]

$$\begin{aligned} \nu_e + \overline{\nu}_e &\leftrightarrow e^+ + e^- \\ e^- + \overline{\nu}_e &\rightarrow e^- + \overline{\nu}_e \end{aligned} \tag{2.36}$$

The scattering Feynman diagram here has a NC and CC diagram. However, apart from couplings, both have the same overall factor

$$\sigma(\nu + e) \sim \frac{2m_e E_\nu}{\pi} G_F^2 \tag{2.37}$$

where the subscripts of the variables are obvious and G_F is Fermi's four-point interaction constant. In the center of mass frame, it can be seen that $s^2 \sim 2m_e E_\nu$ and since the neutrino is in thermal equilibrium with the primordial plasma, $s \sim T$, hence $\sigma \sim G_F^2 T^2$. The previous section review on statistical mechanics tells us that for the radiation era of the universe ($v \sim c$) we have the approximation $n \sim T^3$ for both neutrinos and electrons (self

interactions or scattering). Bring everything thing together

$$\frac{\Gamma(T_{fo})}{H(T_{fo})} \sim 1 \rightarrow T_{fo} \sim 1\ MeV \tag{2.38}$$

In a model where neutrinos instantaneously decouple from the primordial plasma, this would be the point where, just like the photons, there would be a surface of last scattering, and the surface would define the cosmic neutrino background (CνB). This is not the case, as the number density of neutrinos indicates that there was some small coupling to the primordial plasma due to the electron-positron pair annihilation causing some reheating. The process is the *incomplete neutrino decoupling era*, and in fact is the cause of the number of effective neutrinos not coming out to be $N_{eff} = 3$, but slightly higher. It was discovered that this was a perfect probe for new physics, allowing the neutrino oscillation paradigm to be incorporated and tested [9, 22].

Research has shown that neutrinos oscillate between each of the flavors under an oscillation probability. The mechanism that allows for such oscillation indicates that neutrinos must have at least a small mass. Incorporating this fact into the calculation of the energy density of neutrinos after freeze-out by modeling the neutrinos as a non-relativistic massive fluid and noting $\rho_{\nu_i} = m_{\nu_i} n_{\nu_i}$ gives us the expression [9, 22, 23]

$$\Omega_\nu h^2 = \frac{\sum m_{\nu_i}}{93.12eV} \tag{2.39}$$

where $i = 1, 2, 3$. Neutrino oscillation experiments [23] have been able to identify a lower limit on the sum of the neutrino masses $\sum m_{\nu_i} > 0.06eV$, and for upper limits the CνB analyzed via the Planck $\sum m_{\nu_i} < 0.13eV$. The upper limits leads to the expression (using $h \sim 0.7$)

$$\Omega_\nu < 0.003 \tag{2.40}$$

Its seems that relic neutrinos could make up only a tiny fraction of DM. Even at this instance,

we see that such a small mass would indicate that neutrinos would be associated with *hot relics* as they are still relativistic after freezing out. DM, under the standard cosmological models, is viewed as a *cold relic*. This means instead of using the relativistic equation of the number density, we must turn to the non-relativistic number density equation 2.34. This leads us into the realm of weakly interacting massive particles (WIMPs).

2.2 Weakly Interacting Massive Particles

2.2.1 Cold DM: From Equilibrium to Freeze-out

Before getting into WIMPs, understanding how cold DM freezes out in the homogeneous expansion of the universe is instructive as it serves the basis for any DM model to at least satisfy. This is done via statistical mechanics (obviously) and in particular, the use of the *Boltzmann equation*. We used the Boltzmann equation indirectly in the determination of the neutrino freeze out. In the process

$$1 + 2 \leftrightarrow 3 + 4 \tag{2.41}$$

where the arrows indicate the process can go both ways. If we fixate on understanding the evolution of particle 1, we need to establish how the number density of particle 1 can change. The obvious change is the expansion of space-time characterized by the scale parameter (a(t)) and, therefore, Hubble's parameter H(t) described in the last section. Looking at the interaction equation above, we can also see that particle 1 can annihilate with species 2 but also be subsequently created due to the reverse process; this means at a qualitative level, n_1 depends on the number densities n_3 and n_4 positively, and negatively on n_2. The Boltzmann equation, in its integral form, is expressed as

$$\left(\frac{\partial f}{\partial t}\right)_{coll} = -\int \prod_{j=2}^{4} d^3 p_j \delta^4(P_f - P_i)|T_{fi}|^2(f_1 f_2 - f_3 f_4) \tag{2.42}$$

This relationship takes the form [9]

$$\frac{1}{a^3}\frac{d(n_1 a^3)}{dt} = -\langle\sigma_{12}v\rangle\left[n_1 n_2 - \left(\frac{n_1 n_2}{n_3 n_4}\right)_{eq} n_3 n_4\right] \tag{2.43}$$

where $\langle\sigma_{12}v\rangle$ is the *thermally averaged cross section*. The quantity will become important for the rest of this dissertation as this quantity is used to understand the self-interaction cross-section of DM. The form of the Boltzmann equation is spread through all literature concerning the freeze out of DM. In order to do this, we need to understand what mechanisms could possibly keep DM in thermal equilibrium with the primordial plasma of the universe. Given the primary interaction we know it exhibits cosmological is gravitational, the mechanism keeping DM in equilibrium might have been its self-interactions. For example,

$$\chi + \overline{\chi} \rightarrow l + \bar{l} \tag{2.44}$$

where l can be a SM particle. There are plenty of DM models (including boosted dark matter (BDM), which is the model investigated in this dissertation) that have dark sectors to SM portals. However, since there is a lack of evidence that DM interacts with the SM particles in ways other than gravity, these portals have small couplings to the SM. Even though DM is considered in some literature *collisionless*, the self-interactions may still be larger. In the temperature regime $T \gg m_\chi$, these self-interactions could also produce more DM since the energy for production is available. After the temperature of the universe cools, production to SM particles can dominate the self-annihilation products of DM, thereby also accelerating DM's decoupling from the primordial plasma. Although there is some sense in this, there are many questions regarding big bang nucleosynthesis (BBN).

To understand the freeze-out of DM, there are some assumptions that have to be made. The equilibrium interaction products $l + \bar{l}$ must tightly couple to the primordial plasma. This is not a far fetch assumption if the equilibrium interactions for l are electromagnetic in nature. Under this assumption, the number density of l takes always its equilibrium form

$n_l = (n_l)_{eq}$. Assuming baryogensis and leptogensis happens after this point in time, we can take $n_\chi = n_{\overline{\chi}}$ and $(n_l)_{eq} = (n_{\overline{l}})_{eq}$. Plugging all this into equation 2.43 we obtain

$$\frac{1}{a^3}\frac{d(n_\chi a^3)}{dt} = -\langle\sigma v\rangle \left(n_\chi^2 - (n_\chi)_{eq}^2\right). \tag{2.45}$$

Last section we calculated that entropy is conserved with co-moving coordinates under the assumption of a homogeneous, isotropic universe. Also, we are assuming the chemical potential of each species is zero for now, hence this is explicitly told with equation 2.26. This means we now have two equations

$$\begin{aligned} \frac{dn_\chi}{dt} &= -3Hn_\chi - \langle\sigma v\rangle \left(n_\chi^2 - (n_\chi)_{eq}^2\right) \\ \frac{ds}{dt} &= -3Hs \end{aligned} \tag{2.46}$$

These equations can be combined by introducing a variable $Y = n/T^3$ and noting that in the relativistic regime (which is the time in which DM is speculated to have decoupled from the primordial plasma) we have $s \sim T^3$, which can be shown via equation 2.24. This means that at relativistic eras $Y \sim n/s$. Differentiating Y over time gives

$$\frac{dY}{dt} = \frac{1}{s}\frac{dn}{dt} - \frac{n}{s^2}\frac{ds}{dt} \tag{2.47}$$

Putting the previous expressions into this equation and noting that $\frac{d}{dt} = -HT\frac{d}{dT}$ and defining $x = m/T$ we obtain

$$\frac{dY}{dx} = \frac{\langle\sigma v\rangle\, s}{Hx}(Y_{eq}^2 - Y^2) \tag{2.48}$$

where all variables pertain to the particle χ. We can make this look even clearer by substituting for $s = n/Y$ and remembering that $\Gamma = n\langle\sigma v\rangle$

$$\frac{dY}{dx} = \frac{1}{xY_{eq}}\frac{\Gamma_{eq}}{H}(Y_{eq}^2 - Y^2). \tag{2.49}$$

Tracking what happens to Y is all about tracking Γ_{eq}/H. When we are tracking in the very early primordial plasma era ($\Gamma_{eq}/H \gg 1$) we have Y in essence "chasing" Y_{eq}. In fact, in the limit where $Y \sim Y_{eq} \rightarrow \frac{dY}{dx} \sim 0$, the temperature is high $x \ll 1$ and therefore we can use the relativistic number density from the previous section and note that

$$Y \sim Y_{eq} = \frac{n_{eq}}{T^3} = 3\zeta(3)/(4\pi^2) \approx 0.1 \tag{2.50}$$

where I used $n_{fermion} = n_{eq}$ assuming a fermionic dark matter particle. To analyze further, we can simplify $\frac{dY}{dx}$ by noting that

$$H^2(T) = \frac{\rho}{3M_P^2} \propto T^4 \rightarrow H(m) = H(T)/x^2 \tag{2.51}$$

$$\frac{\Gamma(T)}{Y(T)} = n \langle \sigma v \rangle \left(\frac{T^3}{n}\right) = T^3 \langle \sigma v \rangle = \frac{\Gamma(m)}{x^3} \tag{2.52}$$

therefore, the final formula for the evolution of Y now reads

$$\frac{dY}{dx} = \frac{\lambda}{x^2}(Y_{eq}^2 - Y^2) \tag{2.53}$$

where $\lambda = \Gamma(m)/H(m)$. We already looked at the case $Y \sim Y_{eq}$, what about the other extreme $Y \gg Y_{eq}$? This is the case after freeze out and the number density decreases according to the Boltzmann factor $n \sim e^{-x}$. In this extreme, Y evolves as

$$\frac{dY}{dx} \approx -\frac{\lambda}{x^2}Y^2. \tag{2.54}$$

Integration of both sides from freeze out time x_f to current time x_0 and noting again that dark matter freezing out early from the primordial plasma is characterized by $x_f \ll x_0$

$$Y_0 \approx \frac{x_f}{\lambda} \tag{2.55}$$

Recall that $\lambda = \Gamma(m)/H(m)$ which is an interaction rate of the DM particle with the primordial plasma. The higher the interaction rate, the less relic abundance there will be today, which makes intuitive sense.

2.2.2 The WIMP Miracle (or Lack Thereof?)

Everything from this chapter has been built up for this moment. We have an expression for the freeze out time for DM and we know from observations $\Omega_{DM} \sim 0.23$. The freeze out time x_f and the thermal average cross section can now be tuned in order to achieve Ω_{DM}. We know the freeze out time x_f follows the equation Y_0 for the present day and $n_{0\chi} \sim Y_{0\chi} T_0^3 \frac{g_*(T_0)}{g_*(m_\chi)}$, where χ is again the DM particle. In this equation g_* is the number of degrees of freedom for the primordial plasma taking into account all particles in the SM and our new particle χ. As each species decouples from the plasma, the number decreases. Hence the ratio $\frac{g_*(T_0)}{g_*(m_\chi}$ accounts for this change. This effect is implicitly related to the expansion of the universe. The definition of Ω_{DM} is

$$\begin{aligned} \Omega_{DM} &= \frac{\rho_{0\chi}}{\rho_{crit0}} \rightarrow \rho_{crit0} = 3M_p^2 H_0 \\ &= \frac{m_\chi n_{0\chi}}{3M_p^2 H_0^2} = \frac{m_\chi T_0^3}{3M_p^2 H_0^2} \frac{x_f}{\lambda} \frac{g_*(T_0)}{g_*(m_\chi)} \end{aligned} \tag{2.56}$$

plugging in all the variables obtained from the previous section we finally get the relic density of DM [7, 9]

$$\Omega_{DM} \sim 0.1 \frac{x_f}{\sqrt{g_*(m_\chi)}} \frac{10^{-8}\ GeV^{-2}}{\langle \sigma v \rangle} \tag{2.57}$$

Y has the range of the freeze out $x_f \sim 10....60$. Assuming DM froze out early ($x_f \sim 20$) and the self-interaction cross section is at the weak scale ($\langle \sigma v \rangle \sim 10^{-8} GeV^{-2}$), we achieve the relic density that of what is observed assuming DM exists $\Omega_{DM} \sim 0.2$ [9]. Due to the "right" relic density achieved by assuming cross section at the weak scale, this calculation is often called the "WIMP miracle".

This by no means results in DM having solely weak interactions. These findings indicate

that the cross sections that kept it in equilibrium in the early universe and its self-interaction are of the order of the weak scale provide the freeze paradigm laid out in this section is the majority of the story regarding DM's history in the early Universe.

2.2.3 The Search Continues

WIMPs fall under the cold dark matter (CDM) model as opposed to hot dark matter (HDM). If a particle falls under the CDM paradigm, the particle velocity distribution is non-relativistic. Typically, experiments search for WIMP-nuclear interactions. Due to the low kinetic energy associated with non-relativistic interactions $\mathcal{O}(keV - 100keV)$. However, progress has been made with the construction of more and more experimentally sensitive detectors. Since the start of the 21st century, a large effort has focused on detecting DM matter from the galactic halo. The idea is that as the solar system rotates around the Milky Way Galaxy, the Earth sweeps through the halo, having a greater possibility of accomplishing direct detection via DM-nucleon interaction. The various detectors used to search for WIMPs are defined by the material or element used as the detector medium for WIMP-nucleon interactions [24]:

- **Noble Element Scintillators** consist of a vessel with a noble element in a liquid state. The two common mediums are liquid argon (DEAP [25] at SNOLAB and DarkSide [26] at LNGS) and liquid xenon (ZEPLIN [27] detector and XENON1T [28] detector). If a WIMP particle were to interact with the nucleus of the medium, scintillation light is emitted the recoil atom and Photomultiplier Tubes (PMTs) are strategically placed to detect this light.

- **Crystal Scintillators** work similar to noble element scintillators. The difference is that the interaction medium now are crystals. The DAMA/LIBRA [29] experiment uses sodium iodide doped in Thallium. The DAMA/LIBRA experiment was designed to measure the annual modulation due to entering and exiting the galactic plane DM

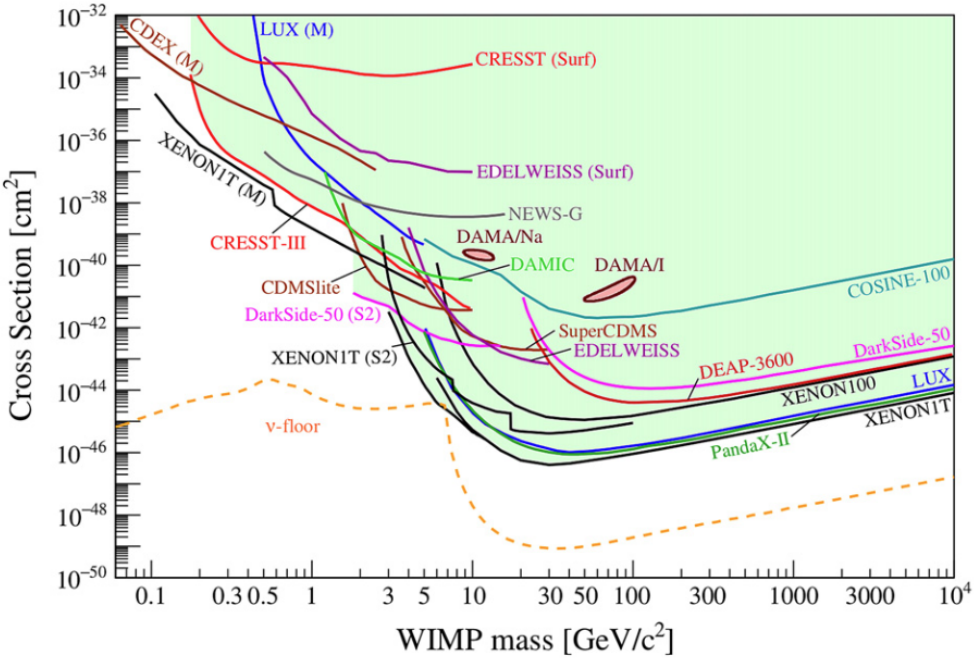

Figure 2.3: Sensitivity curves @ 90%C.L for various future experiments along with the current limit set by the large mint green area [24].

halo section.

- **Bubble Chambers** consist of a superheated liquid that can be ionized by traversing charged particles that vaporize the liquid surrounding the track. The superheated phase of the liquid is enabled by a movable piston that changes the pressure of the liquid inside a large cylinder. The vapor produced by the tracks creates bubbles that increase in size as the movable piston changes the pressure in the volume. Once the bubbles are visible enough, a camera takes pictures of tracks and reconstruction of events can begin. Magnetic fields are also used in order to obtain the charge sign of the particle leaving the track.

- **Time Projection Chambers** essentially combine aspects of scintillators by using a noble gas or noble liquid as the detector medium and PMTs as an autonomous triggering mechanism. Instead of using a camera to record particle tracks, a uniform electric field is applied to the active volume to drift ionization electrons to wire planes

for track reconstruction and calorimetric information. This dissertation makes use of this technology as will be discussed in chapter 3.

The parameter space WIMP Spin Independent/Dependent cross-section (σ_{SI} and σ_{SD} respectively) as a function of WIMP mass is explored, and typically the experimental sensitivity is measured by it's parameter space coverage. Figure 2.3 shows the current sensitivity for proposed experiments and limits (mint green area) for the σ_{SI}-WIMP mass parameter space.

The main difficulties in the search for WIMPs are having the energy sensitivity for low energy DM-nucleus interactions and having enough detector medium for low interaction cross sections. These limitations on current and future experiments are explicitly shown in Fig. 2.3 in the sub-GeV WIMP mass region. WIMP searches become increasingly difficult as one tries to explore the sub-GeV mass region. Since WIMP searches are done by waiting for its interaction with the nucleus, the recoil energy transferred to the nucleus decreases as the mass of the WIMP decreases. The parameter space excluded by experiments is already sensitive to nuclear recoil energies $O(keV)$, given the non-relativistic nature of DM.

2.3 Boosted Dark Matter and the Dark Photon

If DM is not composed of a single constituent, non-relativistic particle, then the non-relativistic, WIMP-like component can be indirectly probed by a kinetically boosted lower-mass component if the lower mass component is produced by self-annihilation of the WIMP-like component [30]. This scenario allows for a multi-particle dark sector. The dark sector can be secluded, where the only interaction between the dark sector and the Standard Model (SM) is gravitational. Alternatively, the dark sector can exhibit a non-gravitational portal for DM-SM interactions to take place. The freeze-out evolution of this scenario is described by the assisted freeze-out mechanism [31].

The Boosted Dark Matter (BDM) model has a dark sector composed of four particles: χ_0, χ_1, χ_2, and a new U(1)' gauge boson X known as the dark photon [30, 32, 33]. χ_0 is

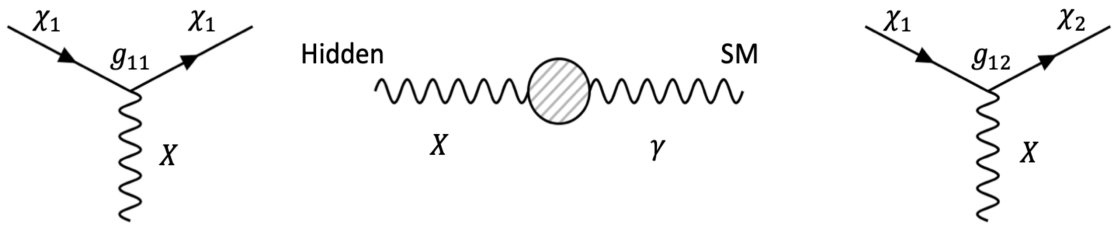

Figure 2.4: The Feynman diagrams for the flavoring conserving (left) interaction($\chi_1 x \rightarrow \chi_1 x$), kinetic mixing DM-SM portal (middle) interaction ($X \rightarrow \gamma$), and the flavor changing (right) interaction ($\chi_1 x \rightarrow \chi_2 x'$) allowed by the added terms to the SM lagrangian in eq. 2.59.

the abundant, WIMP-like DM component and is responsible for the observed gravitational anomalies. χ_1 is the lower-mass, kinematically boosted DM component produced by the χ_0 self-annihilation process $\bar{\chi}_0\chi_0 \rightarrow \bar{\chi}_1\chi_1$. We have the condition $m_0 \gg m_1$, where m_0 is the χ_0 mass and m_1 is the χ_1 mass. The outgoing χ_1 particles will be kinetically boosted with a possible increase to a total energy of $O(GeV)$. The main sources of χ_1 are predicted to be at the galactic center and the hypothesized galactic DM halos. Taking the galactic center as the main source for χ_1, we have the flux [30, 34]

$$F = 1.6 \times 10^{-4} cm^{-2} s^{-1} \left(\frac{\langle \sigma v \rangle_{0\rightarrow 1}}{5 \times 10^{-26} cm^3 s^{-1}} \right) \left(\frac{GeV}{m_0} \right)^2 \tag{2.58}$$

where $\langle \sigma v \rangle_{0\rightarrow 1}$ is called the thermally averaged cross-section times velocity of the self-annihilation process $\bar{\chi}_0\chi_0 \rightarrow \bar{\chi}_1\chi_1$. This value is rooted in the thermal relic density of DM observed by cosmological data that reflects the cosmic microwave background (CMB) via recombination and the production of light elements in the early universe via Big Bang Nucleosynthesis (BBN) [17]. χ_2 is the excited state during inelastic scattering involving χ_1. The mass hierarchy becomes $m_0 \gg m_2 > m_1$. The new Lagrangian terms to encapsulate the BDM dark sector are

$$\mathcal{L} \sim g_{11}\bar{\chi}_1\gamma^\mu\chi_1 B_\mu - \frac{\epsilon}{2} F^{\mu\nu} X_{\mu\nu} + g_{12}\bar{\chi}_2\gamma^\mu\chi_1 B_\mu + \frac{1}{2} m_X^2 B^\mu B_\mu. \tag{2.59}$$

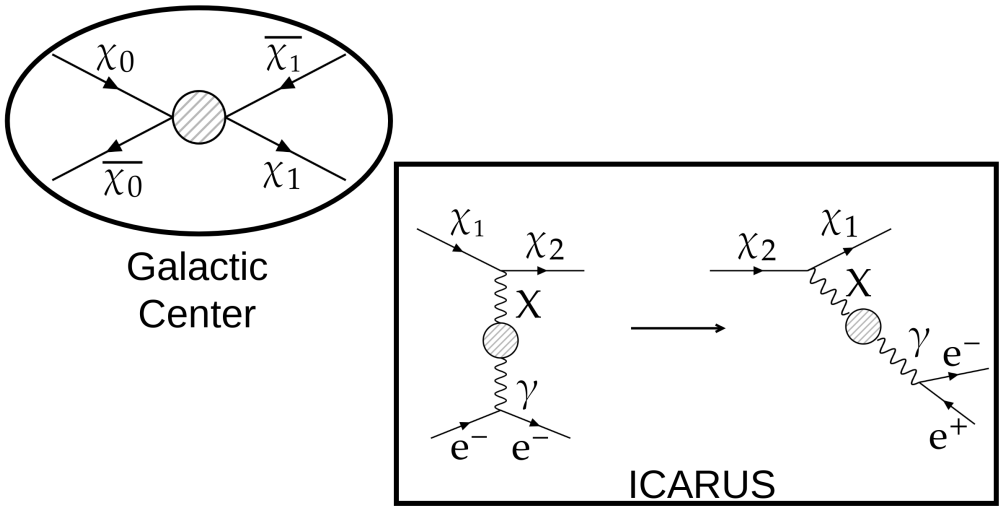

Figure 2.5: Diagram showing the creation of χ_1 via the self-annihilation of χ_0 in the galactic center and the eventual iBDM interaction in the detector.

where B_μ is the four-vector potential of the dark photon, $X^{\mu\nu}$ is the field strength tensor of the dark photon, $g_{11(12)}$ the elastic (inelastic) interaction coupling constants, ϵ is the kinetic mixing parameter, m_X is the dark photon mass, and the χ here are the spinors for the DM particles assuming fermionic DM. Figure 2.4 shows the various Feynman diagrams that relate to the terms in eq. 2.59. The first term is the left-most Feynman diagram. This term is part of elastic BDM processes. The middle Feynman diagram shows the hidden-to-SM sector portal via the kinetic mixing between the dark photon and the SM photon.

2.3.1 Elastic and Inelastic BDM

The first term in equation 2.59 allows for elastic scattering termed elastic boosted dark matter (eBDM) such as $\chi_1 e^- \rightarrow \chi_1 e^-$. Since χ_1 is produced via the self-annihilation of χ_0 and $m_0 \ll m_1$, the mass-energy is mostly transferred to kinetic energy on the order of $O(100\text{ MeV})$ (explored in Ch. 7). This allows χ_1 interactions to deposit energy much higher than a standard WIMP-like particle would through nuclear recoil. However, eBDM has the background from the elastic neutrino process $\nu e^- \rightarrow \nu e^-$. This paper will focus on the inelastic term, opting for $g_{11} \ll g_{12} \sim 1$. This scenario favors the flavor-changing interaction

called inelastic boosted dark matter (iBDM) and the general process takes the form

$$\chi_1 e^- \to \chi_2 e^- \to \chi_1(X^*)e^- \to \chi_1(l^+l^-/\bar{\chi}\chi)e^- \tag{2.60}$$

where X^* denotes the ability of the dark photon decaying on-shell ($m_X < m_1+m_2$) or off-shell ($m_X > m_1 + m_2$). The $l^\pm$ denotes a lepton flavor decay, and $\bar{\chi}\chi$ is the DM decay channel in the $m_X > 2m_1$ kinematic region. The iBDM process is separated into the primary interaction ($\chi_1 e^- \to \chi_2 e^-$) and the secondary interaction ($\chi_2 \to \chi_1 X^* \to l^+l^-$). In this dissertation, the iBDM process under consideration is the one in which the primary interaction is with an electron, and the secondary interaction results in the χ_2 decay into an electron-positron pair($\chi_2 \to \chi_1 X^* \to e^+e^-$).

iBDM is an inelastic process, and the kinematics of the χ_1 interacting with an electron set limits on the kinetically accepted values for m_2. The range of values are set by the center-of-mass (CM) energy $\sqrt{s}$ and the target particle mass m_e

$$\sqrt{s} - m_e \geq m_2 \to \sqrt{m_e^2 + m_1^2 + 2E_1 m_e} - m_e \geq m_2 \tag{2.61}$$

With parameter ranges and values in place, the differential cross-section for the primary interaction $\chi_1 e^- \to \chi_2 e^-$ can now be presented in the form [33]

$$\frac{d\sigma}{dE_e} = \frac{m_e}{8\pi\lambda(s, m_e^2, m_1^2)}\overline{|\mathcal{M}|}^2 \tag{2.62}$$

$$\lambda(x, y, z) = x^2 + y^2 + z^2 - 2xy - 2xz - 2yz \tag{2.63}$$

The general form of the matrix element squared $\overline{|\mathcal{M}|}^2$ is

$$\overline{|\mathcal{M}|}^2 = \frac{8(\epsilon e g_{12})^2 m_e}{(2m_e(E_2 - E_1) - m_X^2)^2} \times [\mathcal{M}_0(F_1 + \kappa F_2)^2 + \mathcal{M}_1[-(F_1 + \kappa F_2)\kappa F_2 + (\kappa F_2)^2(E_1 - E_2 + 2m_e)/(4m_e)]] \tag{2.64}$$

With $\mathcal{M}_0$ and $\mathcal{M}_1$ taking the form

$$\mathcal{M}_0 = [m_e(E_1^2 + E_2^2) - (\delta m)^2(E_2 - E_1 + m_e)/2 + m_e^2(E_2 - E_1) + m_1^2 E_2 - m_2^2 E_1],$$
$$\mathcal{M}_1 = m_e[((E_1 + E_2) - (m_2^2 - m_1^2)/(2m_e))^2 + (E_1 - E_2 + 2m_e)][(E_2 - E_1) - (\delta m)^2/(2m_e)]] \tag{2.65}$$

In these relations, $\delta m = m_2 - m_1$, all E_i are taken to be in the lab frame, and F_1 and F_2 are form factors for the different physics possibilities, i.e., nuclear or electron recoil. Note that the differential cross-section is with respect to the recoil particle energy in the lab frame. Since the 4-momentum product of initial momentum to final momentum is Lorentz invariant, the CM product is equal to the lab frame product and, therefore, rearranging terms gives recoil particle energy spectrum

$$E_R = \frac{1}{4sm_T}\{[(s + m_T^2 - m_1^2)(s + m_T^2 - m_2^2)] \\ - [\lambda^{1/2}(s, m_1^2, m_T^2)\lambda^{1/2}(s, m_2^2, m_T^2)]cos\theta_T\} \tag{2.66}$$

Where θ_T is the scattering angle of the recoil target. We can define E_R^{max} as $cos\theta_T = -1$ and E_R^{min} as $cos\theta_T = 1$. This means the primary interaction cross-section is computed via the integral

$$\sigma_{\chi_1 N \to \chi_2 N} = \int_{E_R^{min}}^{E_R^{max}} \frac{d\sigma}{dE_R}\, dE_R \ . \tag{2.67}$$

These expressions are integral for the computation of the expected number of iBDM events for an experiment, along with experiment-related parameters such as detector exposure time, medium, and dimensions.

Experiments such as the COSINE-100 collaboration, have established limits on the parameter space through the identification of iBDM in the detector [35] and eBDM in the detector [36] by using some benchmark mass parameter sets (m_0, m_1, m_2), and exploring the dark photon parameter space (m_X, ϵ). Exclusion limits have been set by the COSINE-100

collaboration, motivating the work in the dissertation even more.

There are scenarios where the dark photon itself can be boosted by being created during the self-annihilation of much heavier DM particles ($m_\chi \gg m_X$). These types of interactions have been studied, leading to possible future experiments to search for boosted dark photons [37].

Chapter 3

The ICARUS T-600 at Gran Sasso

The time projection chamber (TPC) was invented by David Nygren in 1974 at the Lawrence Berkeley National Laboratory (LBNL) [38]. The invention represented "a new approach to the problems of track recognition and momentum measurement of high energy charged particles" [38]. The TPC volume is filled with gas that gets ionized when charged particles traverse the gas. An electric field is applied to the sensitive part of the volume, called the active volume, in order to drift the ionization charge to an anode that is composed of a set of sensing planes, where the charge is collected. The signals produced by the sense planes due to the passage or collection of the ionization charge are recorded. The recorded signals provide two coordinates for each element of the track, allowing for the 2D trace out of the track of the traversing charged particles. In addition to the recording of the charge signal, the time of arrival is obtained by the measurement of the electron drift velocity in the type of gas used. The time-of-arrival provides the third, depth coordinate, thereby enabling the three-dimensional reconstruction of the trajectory [39].

In 1977, Carlo Rubbia increased the scope of the role of TPC technology with the proposal of the liquid argon time projection chamber (LArTPC) [39] as an alternative to Cherenkov detectors for astroparticle physics experiments, proton decay searches, and neutrino physics, providing both precision 3D tracking and the calorimetric energy measurement capabilities.

The TPC, previously implemented more as a tracking detector, now becomes the target and full-scale detector as an LArTPC. Several experiments have demonstrated the technological robustness of the LArTPC technology at various scales, demonstrating the stability of all subsystems with hundreds of tons of LAr [40, 41, 42]. The scalability and stability of the technology make it simultaneously a large target and sensitive detector. Developing LArTPCs from small-scale to kton-scale experiments has been the goal of the ICARUS project [40, 43, 44, 45] and the Deep Underground Neutrino Experiment (DUNE) far detector prototype experiments (ProtoDUNE) [41, 42]. The ICARUS project produced the first multi-hundred-ton LArTPC detector, *the ICARUS T-600 detector* [40]. The detector was installed and commissioned at the Gran Sasso Underground National Laboratory (LNGS), providing a large overburden for the suppression of cosmic rays in order to be highly sensitive to rare physics interactions such as neutrino interactions, proton decay and theoretical beyond Standard Model interactions such as dark matter interactions.

In this chapter, the LArTPC technology is presented. An overview of the ICARUS T-600 detector at the Gran Sasso Underground National Laboratory (LNGS) is presented. The key motivations for the search for inelastic boosted dark matter are explained at the end of the section.

3.1 LArTPC Overview

In this section, a brief overview of the various LArTPC components is presented. The beneficial properties of elemental argon are presented, demonstrating its superiority over the other noble gases. The main components of the TPC are described, leading to the presentation of the ICARUS T-600 detector at LNGS.

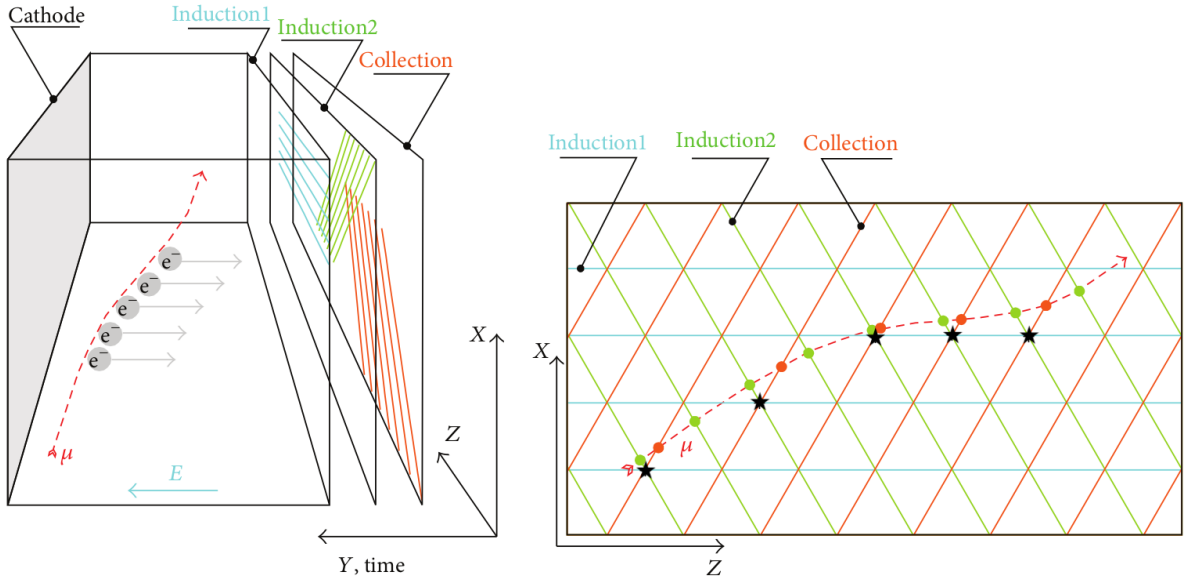

Figure 3.1: A cartoon showing the inner workings of one of a TPC in the ICARUS T-600 detector [46]. On the left cartoon, there is a depiction of a muon traversing the detector, ionizing the liquid argon around it, generating free electrons and argon ions(not depicted). The muon path is not straight because of multiple Coulomb scattering. The right image depicts how the induction and collection sense planes (depicted as *wire planes* here) define points along the projection of the track in the X-Z view (marked as black stars).

3.1.1 The LAr in LArTPC

Liquid argon (LAr) as the detector medium has advantages due to its abundance, density, electron mobility, and light scintillation properties [39, 40, 48, 49]. The relevant LAr properties are shown in Table 3.1 [47]. Further information and simulation of electron transport properties in gas argon (GAr) and LAr are studied in detail in Ref. [48]. Although the other noble elements can also be used as the detector medium, their cost outweighs any advantage when considering scalable detector technologies [39, 50].

Argon is the most abundant of the rare noble gases. The atmosphere is composed of roughly 1% argon and is the main source used in the industry for argon extraction [51]. Argon is readily liquefied by the use of liquid nitrogen because the LAr boiling point (87K) is higher than the liquid nitrogen boiling point (77K). Liquid nitrogen is typically cheap to produce, further making LAr the most abundant and cheap choice among all the noble

Quantity	Symbol	Value
Atomic Number	Z	18
Molar mass	M^{Ar}_{molar}	39.948 g/mol
Boiling Point(1 atm)	T_{BP}	87.26 K
LAr Density at T_{BP}	ρ_{LAr}	1396 kg/m^3
Ionization Energy	I_e	13.84 eV
Radiation Length	X_0	14 cm
Mean Specific Energy Loss per Length	$\left\langle \frac{dE}{dx} \right\rangle$	2.12 MeV/cm

Table 3.1: Table of liquid argon (LAr) properties [47]. The radiation length and mean specific energy loss are specific to minimum ionizing particles (mip) such as electrons (e) and muons (μ).

elements.

Due to the high electron mobility properties of LAr, there is low transverse diffusion of the ionization charge when drifted by an appropriate drift electric field strength. Studies on drift distance versus applied electric field have been conducted, showing the optimal electric field for a given drift distance [48].

The LAr is monitored by many methods, such as measuring the charge attenuation of through-going cosmic muon tracks along the drift direction to correct the charge signal on the TPC wires [52]. The LAr is continuously filtered and recirculated to remove the electronegative impurities, mainly oxygen, which capture the ionization electrons during the drift. s

3.1.2 The TPC in LArTPC

The two images in Fig. 3.1 show the essential pieces of a LArTPC (left image, without the field cage) and the methodology of the 2D reconstruction using the different sense planes (right image). The time projection chamber (TPC) consists of a cathode, an anode that consists of sensing planes to obtain the 2D information of the tracks and is situated opposite the cathode, and a field cage that consists of adjacent electrodes that envelope the volume in between. The volume enveloped by the field cage is referred to as the *active volume*.

The right image depicts 2D reconstruction using the sense planes. Matching the signals induced on the various sense planes (colored points) allows for the reconstruction of the track points (black stars). The angular displacement from the horizontal of the sensing elements on the sense planes (depicted as wires in Fig. 3.1) are tuned to optimize the track reconstruction.

The Drift Electric Field

An electric field is applied to the active volume by supplying a negative high voltage O(-75kV) to the cathode and supplying a voltage to the anode close to detector ground, with typical anode plane biasing ranges $\sim$ 0V-300V for each sense plane; this voltage difference generates an electric field between the cathode and the anode, enabling the drift of ionization electrons toward the anode. The resulting positive argon ions (Ar^+) from the ionization process drift toward the cathode.

The field cage consists of electrodes that wrap the active volume perpendicular to the drift direction. To achieve field uniformity, each electrode is biased according to its position along the drift direction to equate the equipotential of the drift electric field at that position. The electrodes are connected to each other by a chain of resistors. The voltage drop across the resistor chain is tuned to ensure that each electrode is set to the appropriate potential to give the desired uniform field between the anode and the cathode.

The Sense Planes

Generally, LArTPCs have three sensing planes: induction-1, induction-2, and the collection plane(Fig. 3.1). With an appropriately graded bias voltage, the first two planes, Induction-1 and Induction-2 planes, provide signals in a non-destructive manner. The charge of the ionization electrons is finally collected by the last plane, the Collection plane, for the measurement of the particle energy deposition. The sense plane configuration is shown in Fig. 3.1. The elements on the sensing planes are wires, therefore termed wire planes. For the

rest of this dissertation, wire planes will be the technology used for the sensing planes unless otherwise stated.

The passage of the electrons induces a bipolar signal on the Induction-1 and Induction-2 planes, while a unipolar signal on the collection plane. The wires for each plane are aligned at different angles in order to obtain precise 2D projection information. A simplistic example of how to obtain the 2D projection of the tracks in the detector is shown in the right image of Fig. 3.1. The ionization electrons first pass the induction planes, inducing signals on specific wires along each plane. The ionization charge is then collected on the Collection plane, relatively close to the wires induced in the induction planes. These wires are matched, and as a result, a reconstructed point is made (the black stars). Combining the arrival time of the signal on the wire planes with the drift velocity in addition to the corresponding induced wire positions, the adopted stereo-angle wire configuration provides three bi-dimensional projections of any charged particle tracks [40, 46].

The spatial resolution capability of the detector is determined by the distance between the planes and the wire pitch. The wire pitch is constrained to ensure both (1) enough charge is collected on each wire compared to the noise of the readout electronics to ensure an adequate signal-to-noise ratio and (2) that enough measurements are made to have the adequate resolution to reconstruct interaction vertices and perform accurate particle identification via analysis on the charge deposited per unit length by the traversing particles in the detector.

3.1.3 Particle Identification

The particles that create the tracks in the active volume are identified by performing a 3-dimensional track reconstruction to obtain the complete track length in the detector and analyze the charge deposition per unit length of the track [46, 50]. Measuring the charge deposited over segments of a track, dQ/dx, and converting the charge to energy, the resulting dE/dx measurement can be used for particle identification by using the Bethe-Bloch formula [14, 53, 54]

$$\left\langle -\frac{dE}{dx} \right\rangle \approx \frac{4\pi N_A r_e^4 m_e c^2 Z}{M_{mol}\beta^2} \left[\frac{1}{2} ln \left(\frac{2m_e c^2 \beta^2 \gamma^2 W_{max}}{I_e^2} \right) - \beta^2 - \frac{\delta(\beta\gamma)}{2} \right] \tag{3.1}$$

where c is the speed of light, N_A is Avogadro's number, Z is the atomic number of the medium, r_e is the classic radius of the electron in an atom, M_{mol} is the molar mass or atomic mass, γ is the Lorentz factor,$v = \beta c$ is the velocity of traversing charged particle where β is the fraction of speed of light of the velocity of the particle, I_e is the effective ionization potential of the medium, and W_{max} is the maximum energy transfer possible in a single collision expressed as

$$W_{max} = \frac{2m_e c^2 \beta^2 \gamma^2}{1 + 2\gamma m_e/M + (m_e/M)^2}. \tag{3.2}$$

where M is the mass of the particle that is traversing the TPC active volume. This expression is still an approximation for kinetic energy ranges comparable to that of electrons in the LAr, where radiative losses become important [14]. For example, the electron and the muon are considered minimum ionizing particles (m.i.p). The muon, with a higher mass M (200 times more than the electron), can travel further into the material for a given energy with minimal radiative losses. However, electrons with enough energy experience radiative losses much earlier in the track, enabling electromagnetic showers. For this reason, electrons are easily identified by an (m.i.p) signature at the beginning of the track, followed by an electromagnetic shower. Alternatively, muons are long straight tracks, with a consistent m.i.p signature throughout the track.

The m.i.p signature of electrons in muons will be explored further in Ch. 4.

3.1.4 Scintillation Light and its Collection

In addition to ionization, traversing charged particles can excite the LAr atoms. Eventually, these atoms de-excite, resulting in the emission of *scintillation light* [49]

$$Ar^* + Ar \rightarrow Ar_2^* \rightarrow 2Ar + \gamma(\lambda = 128nm) \tag{3.3}$$

Additionally, some ionization electrons will recombine with argon ions (Ar^+), resulting in additional emission of scintillation light [49]

$$Ar^+ + Ar \rightarrow Ar_2^+ + e^- \rightarrow Ar_2^* \rightarrow 2Ar + \gamma(\lambda = 128nm) \tag{3.4}$$

The excited Ar_2^* can either be in a singlet or triplet state, depending on the configuration of the electrons. The result of this variation is that the scintillation light has a fast ($\sim$ 5ns) and slow ($\sim 1\mu$s) component [49].

The scintillation is used as a trigger to indicate the beginning of an event called the t_0. The start time t_0, coupled with the measured drift velocity of the ionization charge in LAr for a given drift electric field, enables the reconstruction of the depth information of the track (distance relative to the wire planes).

Given that scintillation light will be emitted before the ionization charge can drift to the wire planes, the t_0 enables the assessment of impurities in the detector. Studies on the drift velocity of ionization charge in a given drift electric field are all for comparison with data. These comparisons aid in the correction for charge attenuation due to capture by any impurities in the argon when ionization charge is drifted to the wire planes [55].

The capture of scintillation light is performed with a set of *photomultiplier tubes* (PMTs). a wavelength shifter is required to shift the light to a wavelength to which the PMTs are sensitive because the scintillation light wavelength is VUV (λ $\sim$128 nm). The wavelength shifter is applied to the window of the PMT, or a material capable of wavelength shifting is attached in front of the PMT face. PMTs have the capability of triggering on cosmic events down to energies in the keV range [50]. However, its implementation is dependent on the collective efficiency of the PMTs [56].

3.2 The ICARUS Project

The ICARUS project outlined the strategy to achieve the stability and scalability of LArTPCs to detect rare physics processes, such as neutrino physics and beyond Standard Model physics [40]. The ICARUS collaboration planned, tested, and implemented the first renditions of the LArTPC technology, with the efforts guided by Carlo Rubbia [40, 43, 44, 45]. Achieving the required performance with scalability and stability for each of the components took approximately 15 years of R&D, testing LAr purification methods, read-out electronics, and the drift high voltage (drift HV) on small scale :

- **The 3 ton** [43] LArTPC operated for more than four years at CERN. It was exposed to cosmic rays and gamma-ray sources. The experiment showed that ultra-pure LAr is an excellent detector medium capable of $\mathcal{O}(MeV)$ energy resolution. The cryogenic filtering system was designed and tested with results that showed the LArTPC technology could match the resolution of the bubble chamber with room for improvement.

- **The 50 liter** [44] detector also operated at CERN and was exposed to the neutrino beam in its 1997 operational period. This detector's focus was on the viability of reconstructing neutrino events such as $\nu n \rightarrow p\mu^-$, with the goal of testing the detector's capability of resolving nuclear interaction fragments. A study to distinguish electron tracks from photon showers, such as photons from pion decay($\pi^0 \rightarrow \gamma\gamma$), was initiated [44].

- **The 10 m^3** [45] detector had about 14 tons of LAr, coming in as the largest mass of the aforementioned demonstrators. The goal was to study the feasibility of a cryogenic system designed to purify reliably a large LAr detector. It was a significant advancement in the realization of a stable multi-hundred-ton detector.

The R&D of the 3-ton, 50-liter, and 10 m^3 detectors tried and tested the LArTPC technology at the multi-ton stage and proved to have the resolution capabilities for particle

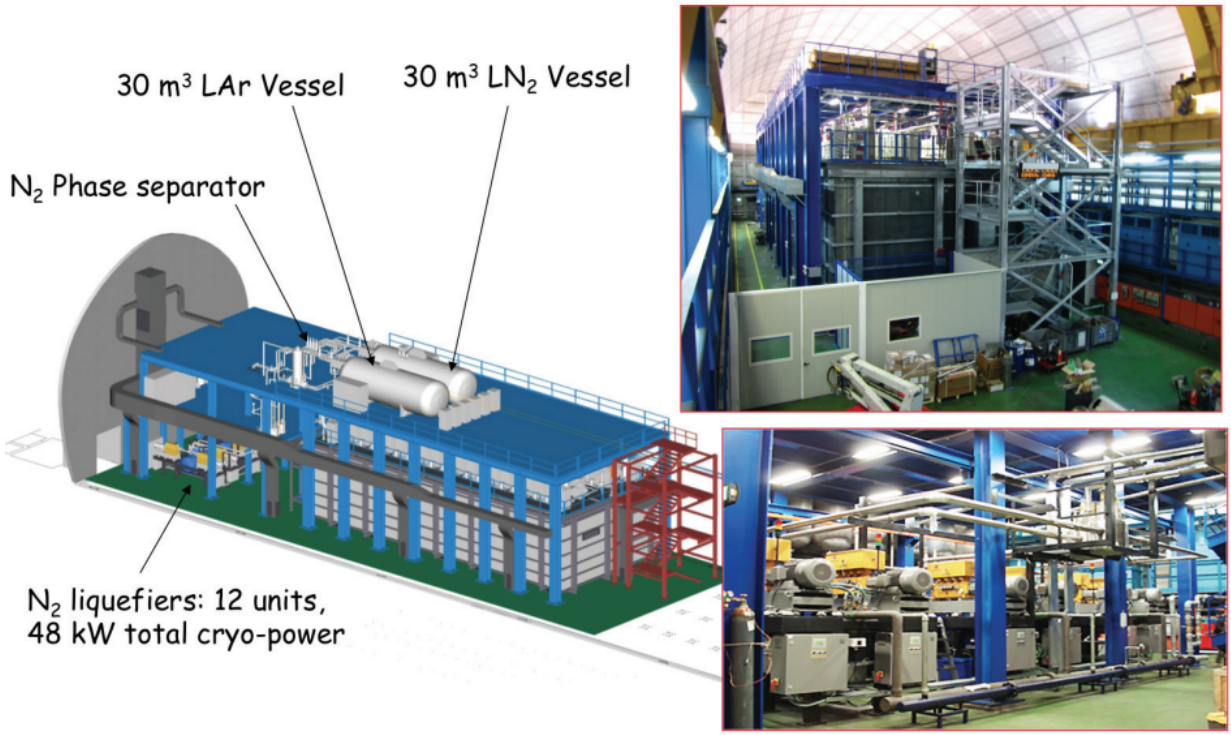

Figure 3.2: A graphic showing the cryogenic system components (left) and the exterior of the two detector modules (right two images) [57].

track reconstruction and particle identification through dE/dx. The next step was a several hundred-ton demonstrator, the ICARUS T-600 detector.

3.3 The ICARUS T-600 Detector

The ICARUS T-600 detector was located at the Gran Sasso Underground National Laboratory (LNGS), before its re-purpose for the Short Baseline Neutrino (SBN) program at the Fermi National Accelerator Laboratory (Fermilab). The ICARUS T-600 LArTPC detector has a total of 760 tons of ultra-pure LAr operated and took data at the Gran Sasso Underground National Laboratory of INFN [40, 58] in 2011 – 2013. The detector consists of two independent T-300 cryostat modules with the internal dimensions 3.6 m (W) × 3.9 m (H) × 19.9 m (L). Each module includes two TPCs which share a common semi-transparent cathode plane in the center of the module.

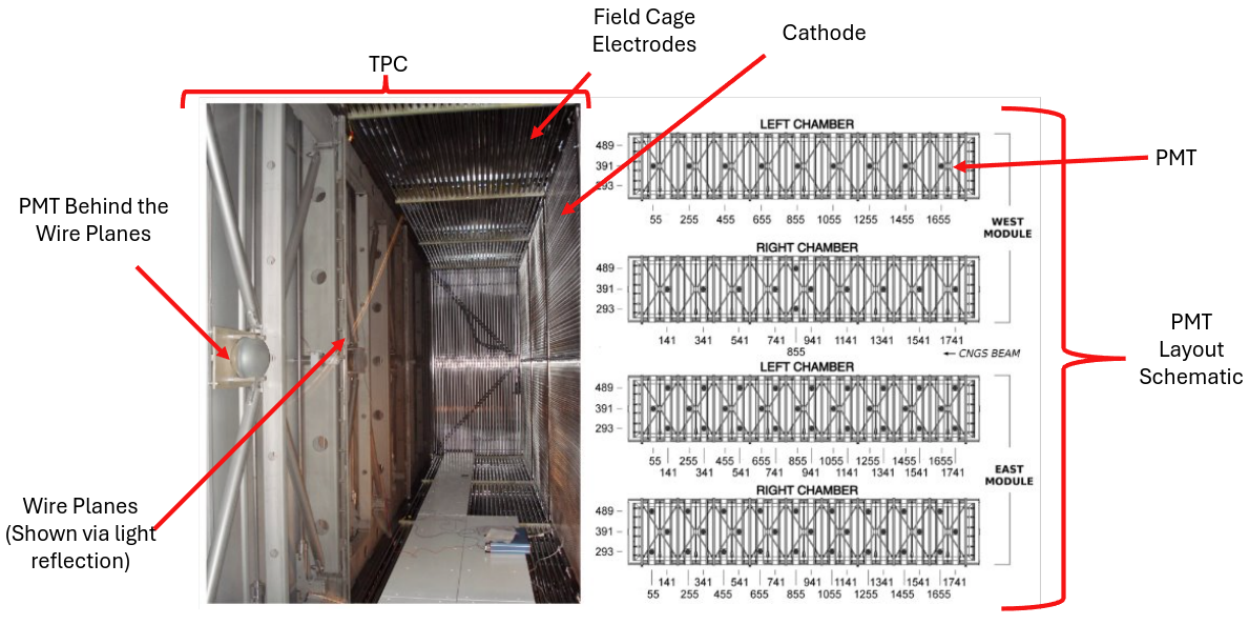

Figure 3.3: A section of a TPC in one of the modules (left) with captions indicating the various TPC components. On the right image is a PMT schematic map indicating the placement in each respective TPC [40, 50].

LAr was continuously filtered and recirculated to remove the electronegative impurities, mainly oxygen, which capture the ionization electrons during the drift. The residual LAr impurities were kept below 50 ppt O_2 equivalent throughout the entire data-taking period, corresponding to $\sim 12\%$ maximum charge attenuation at the longest drift distance [52]. The LAr purity was monitored by measuring the attenuation of the through-going cosmic muon tracks along the drift direction to correct the charge signal on the TPC wires.

3.3.1 Wire Plane System

The TPC anode is composed of three parallel wire planes, 3 mm apart, positioned on either side of the cathode plane and facing inward to the active volume with the 1.5 m drift path. A total of 53,248 wires with lengths up to 9 m are installed in the ICARUS-T600 detector, providing precision tracking capability. [59]. The wires of the Induction-1 plane face the cathode and run horizontally along the length of the detector. The Induction-2 wire plane, 3 mm behind the Induction-1, has a wire orientation of 60° with respect to the orientation of

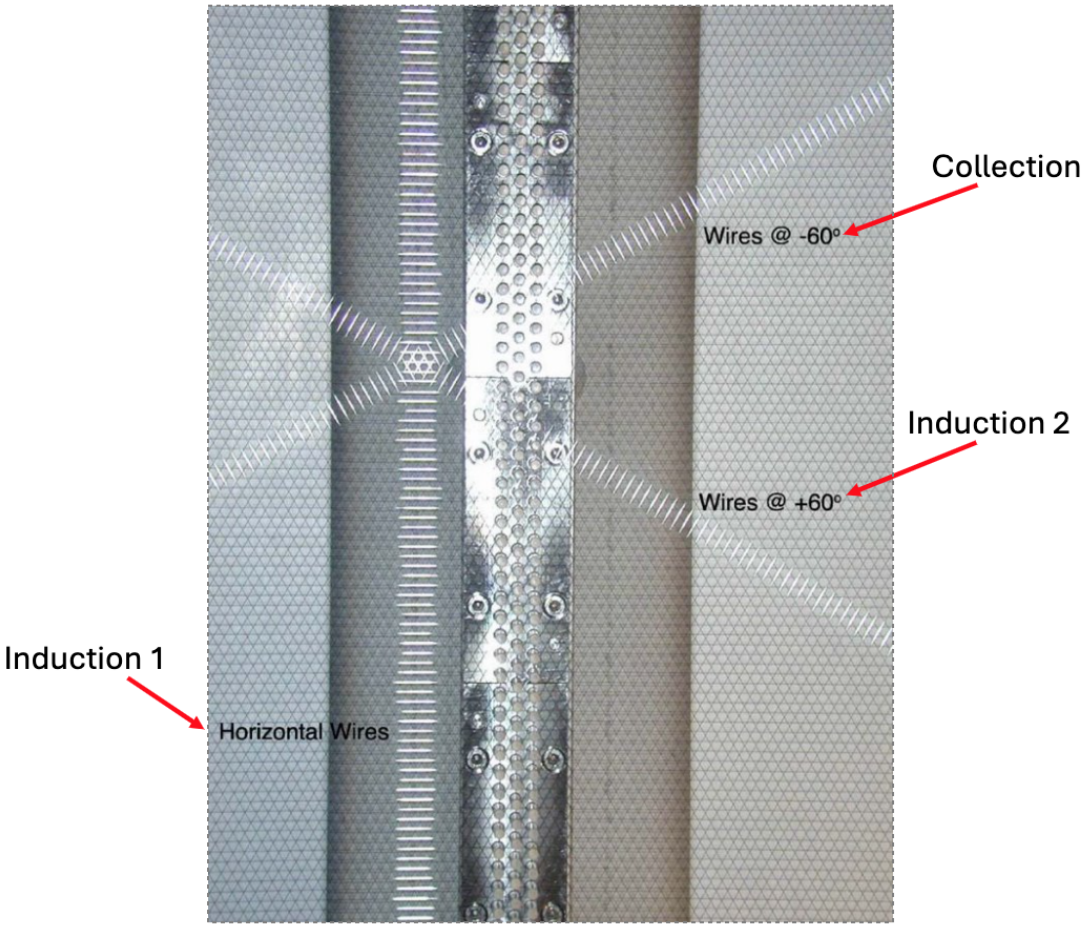

Figure 3.4: A picture of the wire planes seen by the reflection of light on the wires. The three views and their angle with reference to the horizontal is indicated by the reflection of light. Induction 1 is the "Horizontal wires", induction 2 is "Wires @ $+60^o$", and collection is "Wires @ -60^o" [40].

the Induction-1 wires. The wires of the Collection plane are oriented $-60°$ with respect to the Induction-1 wire direction. Figure 3.4 shows the angular orientation of the wire planes from the reflection of a light flash. Each orientation is accompanied by a descriptor that indicates which wire plane the wires correspond to. Combining the arrival time of the signal on the wire planes with the corresponding wire position, the adopted stereo-angle wire configuration provides three bi-dimensional projections of any charged particle tracks.

The wires are biased -220 V, 0 V, and 280 V for Induction-1, Induction-2, and Collection, respectively. The spacing between wire planes and spacing between the individual wires

(wire pitch) is 3 mm. The wire planes are 1.5 m from the cathode, which indicates the maximum ionization charge drift distance in the active volume. The wires are in tension by a movable frame along the mechanical structure of the supports in the cryostat. These are movable for the ability to adjust the wire tension as needed. The 3 mm wire pitch and the 3 mm wire plane separations provide the 3D event reconstruction with ~ 1 mm^3 spatial resolution [40, 46].

3.3.2 PMT System

The scintillation light is collected by the 8" diameter PMTs, coated with a wavelength shifter to allow for the detection of vacuum ultra-violet (VUV) scintillation light that has the wavelength of $\lambda = 128$ nm. Two arrays of 20 and 54 PMTs are installed in the 1$^{\text{st}}$ and 2$^{\text{nd}}$ T300 module, respectively, behind the anode wire planes and outside of the active volume to provide the initial time (i.e., t_0) of an event and the trigger signal. The PMT layout schematic can be seen in Fig. 3.3, along with a photo of the TPC with the wire planes on the left and cathode on the right. An example of a PMT behind the wire planes is indicated in the left image.

The surface diameter of all the PMTs is 8 inches. A layer of a wavelength shifter called Tetra-Phenyl-Butadiene (TPB) is applied to the surface of each PMT. The TPB shifts the scintillation light from VUV to the PMT-sensitive spectrum. The coating has a thickness of 0.2 mg/cm^2 and the process of coating started by sandblasting the window surface of the PMTs, followed by a coat of TPB dissolved in toluene on the sandblasted surface [40]. This thickness and method of application enable a wavelength shifter efficiency better than 90% [40, 56].

The PMTs, as a collective, act as a trigger system for an event. This applies to both cosmic-induced events and beam-induced events. The analog sum of the PMT signals on each TPC is used for the trigger whose efficiency is determined using the combined PMT trigger efficiency [56]. The efficiency of the PMT sum signal depends on the total energy

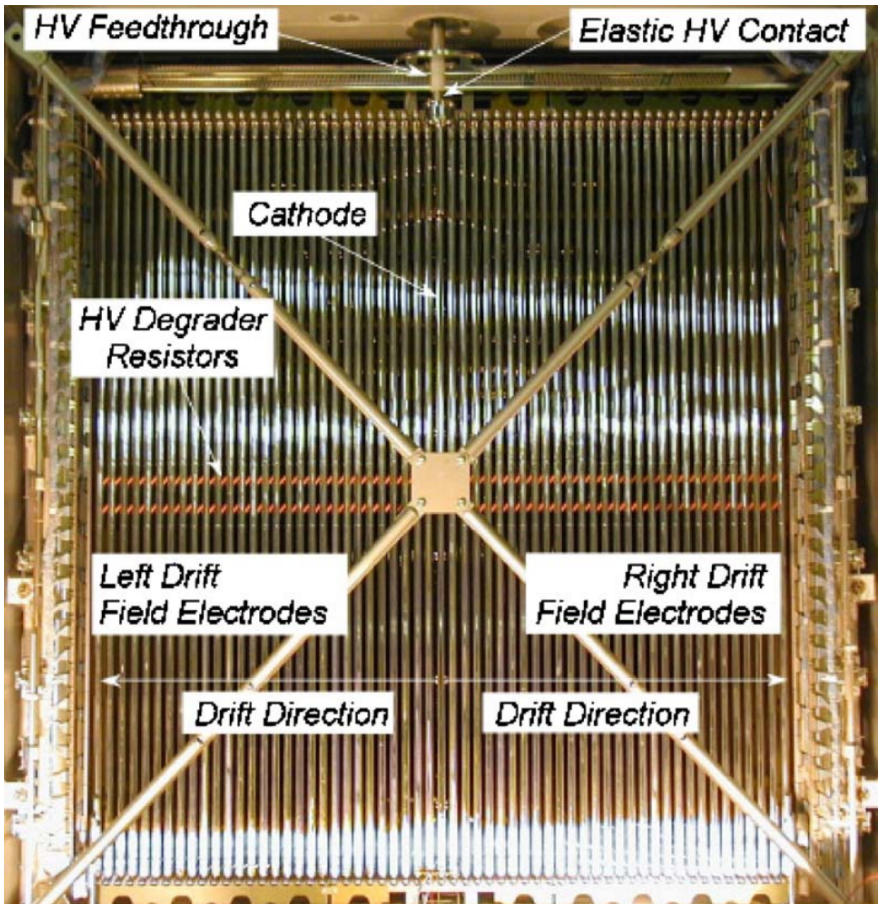

Figure 3.5: A picture outside two TPCs, perpendicular to the drift directions. The various components are indicated in the image [40]. The cathode (identified in the center of the image) indicates the division between the two TPCs and extends into the page.

deposit in the event and the distance from the event to the cryostat walls on which the PMTs are mounted. The efficiency is minimally affected by the smaller number of the PMTs in the first module. Overall, the PMT sum trigger efficiency varies between 80% – 100% for the events that deposit energy in the detector greater than 200 MeV ($E_{\text{dep}} > 200$ MeV) [56].

3.3.3 Drift HV System

The drift HV system is composed of two HV power supplies(HVPS),the cathode, the anode consisting of the three wire plane, and the field cage. The wire planes are described in Sec. 3.3.1, therefore here the other components are described:

- **The cathode** is composed of 9 panels made of hole-punched stainless steel. The

holes are for weight reduction and scintillation light transparency for the PMTs that are positioned behind the wire planes along the walls of the cryostat. The potential supplied to the cathode is -75kV to produce a field of 500 V/cm between the cathode and the wire planes.

- **The field cage** is composed of racetrack electrodes that are connected sequentially by four 100 MΩ resistors in parallel. Figure 3.5 shows the electrodes as the metallic rods extending vertically and the resistors in the middle section with an orange color. The electrodes in Fig. 3.5 are along the drift direction. There are 29 electrodes per TPC spaced 49.6 mm center-to-center. The last electrode is connected to a voltage divider where the measurement across the divider gives an understanding of the condition of the drift HV of the respective TPC. The electrodes are shaped like rectangular rings, with the longest side extending along the longest dimension of the TPC (18.1 × 3.2 m^2). The rings are tubes with a diameter of 34 mm with a thickness of 0.8 mm. The resistors act as degraders, making the potential of each electrode match that of the field produced by the cathode-wire plane system at the cross-sectional point in the sensitive volume where the electrode is located. This ensures constant drift of the electrons, with the field being as uniform as possible in the drift volume.

- **The HVPSs** are connected to each ICARUS module via HV feed-throughs that are held at a potential of -75kV for a 500 V/cm electric field in the active volume.

3.4 ICARUS T-600 iBDM Search Outlook

The LArTPC technology and the ICARUS T-600 detector were described in this chapter. The detector has several advantages that lend itself suitable for dark matter searches, namely

1. **Large Rock Overburden:** The detector is at LNGS that is under 1400 meters of rock(∼3400 meters of water equivalent (m.w.e)) [60], suppressing possible cosmic backgrounds (more on this in Ch. 6)

2. **Large Detector Volume:** The detector contains two cryostats, totaling 420 tons of active volume, making the detector a large target and for rare beyond Standard Model processes such as the iBDM interaction.

3. **Sensitive to iBDM Signature:** The signal for iBDM is now determined to be two electromagnetic showers produced by the recoil electron from the primary interaction and the electron-positron pair from the secondary interaction, which can be systematically searched for in LArTPCs by a visual track inspection (Ch.5) and subsequently verified through a dE/dx analysis(Ch. 4).

The points above illustrate that ICARUS's underground position is instrumental for it's success in exploring the iBDM model parameter space.

There is, however, also the quality and type of data that was recorded by the ICARUS detector during its 2010-2013 operational run at Gran Sasso. In addition, the ICARUS detector was able to trigger neutrinos coming from the CERN neutrinos at Gran Sasso (CNGS) beam and atmospheric neutrinos. Neutrino charged-current (νCC) and neutrino neutral current (νNC) interactions present a potential background because electrons are outgoing particles from these processes.

The next chapter will address the ICARUS data that is used for this dissertation and demonstrate that the atmospheric neutrino data is the perfect place to find the iBDM signal.

Chapter 4

The Data Sample: Atmospheric Neutrino Study

In this chapter, the dataset for the iBDM search is presented. In the previous chapter, the ICARUS detector at Gran Sasso was presented. The geographic location of the detector makes it a prime candidate for performing rare searches such as beyond Standard Model searches. This can be attributed to its large natural overburden of 3400 meter water equivalent (m.w.e), the detector's large active volume of 476 tons of LAr in the active volume, the detectors spatial resolution of $\sim$ mm^3, and The energy resolution for the reconstructed e.m. shower was evaluated to be $\sigma/E(\text{GeV}) = 3\%/\sqrt{E} \bigoplus 1\%$ [58] by the ICARUS collaboration, studying the reconstruction of the π^0 events [58]. The spatial and energy resolution enables accurate particle identification for electron showers and cosmic ray muons, and the large overburden enables the suppression of cosmic ray muons.

The iBDM process, presented at the end of Ch. 2, consisted of a primary interaction

$$\chi_1 e^- \rightarrow \chi_2 e^- \tag{4.1}$$

and a secondary interaction

$$\chi_2 \rightarrow \chi_1(X^*) \rightarrow \chi_1(e^+e^-) \tag{4.2}$$

where X^* kinetically mixes with the SM photon, enabling a dark sector to Standard Model portal through the interaction $(X^*) \rightarrow \gamma \rightarrow e^+e^-$. The final states of the primary and secondary interaction have outgoing particles that are capable of ionizing argon, and, therefore, the iBDM interaction produces a signal in the ICARUS detector. The outgoing particles that are visible, leaving ionization tracks and electromagnetic shower activity, are the recoil electron from the primary interaction and the electron-positron pair from the secondary interaction. Electrons and positrons produce electromagnetic showers after traveling some distance in the detector due to Bremsstrahlung interactions, producing photons that then interact with the argon nuclei and pair produce, causing a shower cascade. The goal, then, is to identify data collected by the ICARUS detector that contains two separate electromagnetic showers.

The ICARUS collaboration at Gran Sasso performed an analysis to identify atmospheric ν_e and ν_μ charged-current (ν_eCC and ν_μCC respectively) interactions [61]. The ν_eCC interactions, in particular, result in an outgoing electron that subsequently showers. For this reason, the ICARUS collaboration developed a software filter algorithm that selects events with evidence of electromagnetic shower activity. If there are iBDM interactions in the data, then the filtered data set will contain the iBDM events.

4.1 Data Overview

The atmospheric neutrino data was taken during the 2012-2013 operational period of the ICARUS detector at Gran Sasso. The full data set for the atmospheric neutrino study corresponds to 0.43 kton·year exposure. The data that was available for this iBDM study corresponds to 0.13 kton·year.

ICARUS neutrino events are categorized as either the neutrinos delivered by the CERN neutrinos at Gran Sasso (CNGS) [62] beam or the atmospheric neutrinos for both ν_eCC and ν_μCC interaction studies [61]. The analysis of both the CNGS beam and atmospheric

neutrino events demonstrated the unique capability of triggering, collecting, and accurately reconstructing neutrino events using the ICARUS LArTPC detector.

A cosmic ray trigger was implemented outside the beam spills of the CERN neutrinos at Gran Sasso (CNGS) beam. The separation of the beam trigger and cosmic trigger was made possible by the innovative "Early Warning" system [56], combined with the sum of the PMT signals as the scintillation light trigger.

The "Early Warning" system was a signal that CERN sent to LNGS notifying of an imminent proton extraction from the Super Synchrotron, which was two spills of 10.5 μs time width, separated by 50 ms, every 6 seconds [56]. A 60 μs width CNGS-gate signal was opened according to the predicted neutrino spill arrival, enabling the full acquisition of the CNGS neutrino interaction events.

The synchronization between CERN and Gran Sasso "early warning" signals had 1%-4% inefficiencies due to missed signals. However, these signals are still on record within a CERN database. Therefore, any cosmic triggers that overlap with the times in the CERN database can be separated, enabling a reduction in efficiency down to less than 1%. This, then, allows for the acquisition of cosmic events with no CNGS background interactions.

4.2 Atmospheric Neutrino Study

The atmospheric neutrino interactions that were identified were of the ν_eCC type

$$\nu_e n \rightarrow p e^- \tag{4.3}$$

and ν_μCC type

$$\nu_\mu N \rightarrow \mu^- X. \tag{4.4}$$

Equation 4.3 indicates that the outgoing visible tracks for ν_eCC are the electron and proton. For ν_μCC, eq. 4.4 indicates that the visible tracks will be left by muons and any nuclear

interaction by-products which are encapsulated by N. Both neutrino interactions exhibit multiple particles coming from a single interaction vertex [61].

Although the overburden of ICARUS at Gran Sasso enabled a great reduction in cosmic ray muons, the number of comics triggers that contained muons was not zero. However, the rate was substantially lower than that seen with surface detectors, with a reduction factor on the order of 10^6 [61, 63]. Cosmic muons that reach the detector can produce delta rays. Delta rays are electrons that are knocked off the argon atoms, producing tracks of their own alongside the muon track. Cosmic muons that enter the detector-sensitive volume at low energies can mimic electron tracks.

The method by which each triggered event was evaluated was through human scanning. The tracks recorded in the wire readout window are visually inspected by a human called a scanner. The scanners are trained to identify neutrino interactions, reaching an efficiency of 80% [61]. The amount of triggered events is on the order of thousands. Therefore, for the sake of efficiency, a filter algorithm was developed to identify neutrino events.

4.2.1 ν_e and ν_μ Filter Algorithm and Efficiency

The filter algorithm works by using the charge deposited on the collection plane, called hits, to form clusters based on a defined distance threshold between hits [61]. Applying this threshold with geometrical and calorimetric data, the largest clusters are identified. This type of filter works efficiently for identifying ν_e(see Table 4.1). Strong rejection criteria, in particular for straight tracks for muon rejection, favor electromagnetic shower events. The filter is applied to Monte Carlo events to identify the efficiency of the filter. The filter efficiencies obtained were $\xi_{filter} \sim 80\%$ for ν_e and $\xi_{filter} \sim 26\%$ for ν_μ(Table 7.1) [61]. The discrepancy comes from the strong criteria on rejected straight tracks to reject cosmic muons, which in turn also reject the ν_μCC-induced muons. Further breakdown of the methodology of this study is in Table 4.1.

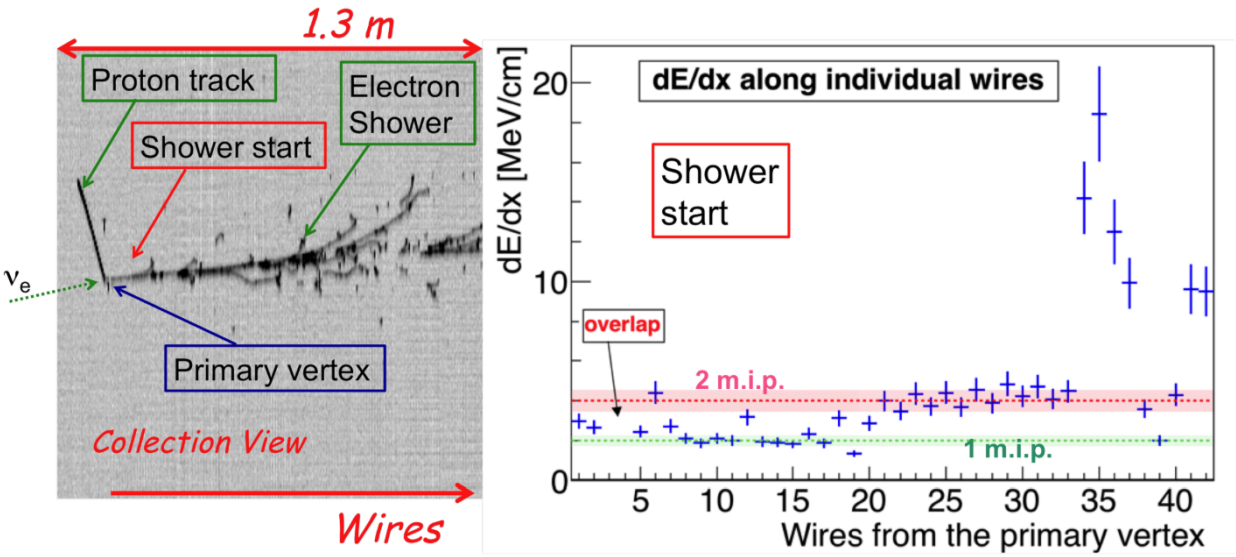

Figure 4.1: An example of an atmospheric ν_e event with the event display (left) and dE/dx as a function of wires from primary vertex (right) [61].

4.2.2 Trigger Efficiency

The trigger system for the cosmic trigger relies on the scintillation light produced by the cosmic ray particles traversing the detector. The detector's PMTs collect the scintillation light. The number of PMTs for each module is asymmetrical(52 PMTs in one cryostat and 20 PMTs in the other), resulting in one cryostat having a slightly higher efficiency across all metrics (Fig. 4.2). The PMT sum signal efficiency is affected by energy, distance from the wall where the PMTs are mounted (behind the wire planes, for picture reference, see Fig. 3.3), and the z position, which is perpendicular to the drift direction [56]. The dependencies of the trigger efficiency on these parameters can be seen explicitly in Fig. 4.2. The values were obtained by studying data with cosmic muon tracks [56].

4.2.3 Scanning Efficiency

Events that pass both the trigger stage and the filter stage are subject to the visual scanning stage. Visual scanning is done by using visualization software to map the wire signal versus time, typically called an event display. A task force was created and trained via Monte

Stages of the Analysis	ν_μ CC	ν_e CC
$N_{evt}^{Expected}$ per kton·year	96.2	78.2
$N_{evt}^{Expected}$ for 0.43kton·year exposure	41.4	33.7
Including the Fiducial Volume	37.8	30.8
Including the Deposited Energy > 200 MeV	24.9	24.2
Filter Efficiency(ξ_{filter})	25.7%	81.4%
Including the filter efficiency	6.4	19.7
Trigger efficiency($\xi_{trigger}$)	86.7%	84.7%
Including the trigger efficiency	5.5	16.7
Including scanning efficiency($\xi_{scanning}$= 80%)	4.4	13.3
Final $N_{evt}^{Expected}$	**4.4**	**13.3**
Number of observed events	**6**	**8**

Table 4.1: Comparisons of the expected number of events, $N_{evt}^{Expected}$ at each stage of the ICARUS atmospheric neutrino study at Gran Sasso [61]. Each row successively applies the detector acceptance and the selection efficiencies, with the final expected number of neutrino events at the application of the scanning efficiency highlighted. The actual number of observed events, highlighted in the bottom row, is consistent with the final expected number of events within the statistical uncertainty.

Carlo-generated events to visually recognize the various topologies for atmospheric neutrino interactions. By looking at the various views, the event display software also allowed for spatial reconstruction (up to 3D spatial reconstruction). The calorimetric and spatial reconstruction lead to the calculation of the total energy and also the measurement of dE/dx. Figure 4.1 shows an example of an electron neutrino event and the dE/dx analysis of the event. Indications of m.i.p signals are present on the graph, which corresponds to the beginning of the electron. The electron eventually showers, which then changes the dE/dx since there are now several m.i.p tracks. The proton is not a m.i.p and can be seen by the darker imprint on the event display.

The scanning efficiency for this study was obtained by generating neutrino Monte Carlo events and going through the detector simulation chain. This output event displays something similar to the real data. The scanners that were part of the task force were trained and evaluated based on the Monte Carlo samples. The efficiency was obtained, and the scanners had an average 80% scanning efficiency.

4.3 Study Results

The full methodology and results of the atmospheric neutrino study are outlined in Table 7.1. Each row represents a procedural step in the analysis. The number of expected ν_e and ν_μ events are shown for a kton·year exposure. As mentioned in the opening of this chapter, the total exposure was 0.43 kton·year. Therefore, the actual expected events before any cuts from the fiducial volume and efficiencies are applied are 41.4 ν_μCC events and 33.7 ν_eCC events.

The fiducial volume is the sensitive volume to the study, which is smaller than the active volume. There was a cut of 5cm in all dimensions, which reduced the sensitive volume to $\sim 91\%$ of the active volume.

The deposited energy cut at 200 MeV is in response to the trigger efficiency. The first row of graphs in Fig. 4.2 shows that at energies below 200 MeV, the PMT sum signal efficiency is well below 80% for one of the cryostat's TPC. For this reason, expected neutrino events with deposited energies greater than 200 MeV were considered.

Lastly, all efficiencies are applied in succession, leaving the final expected number of atmospheric neutrino events to be 4.4 ν_μCC events and 13.3 ν_eCC events.

Once the full data scanning had been conducted, 6 ν_μ and 8 ν_e events were observed. An example of a ν_e event can be seen in Fig. 4.1. The event display on the left shows a vertex with two tracks. The straight, darker, upward-going track is a proton. The rightward-going shower track is an electron leaving from the vertex and then showering. This is a clear $\nu_e n \rightarrow p e^- \bar{\nu}_e$ interaction and is further supported by the dE/dx analysis on the right of the event display showing the m.i.p signature of the beginning of the track that showers.

4.4 Using Data and Methodology for iBDM Search

The atmospheric neutrino study is really a case study for iBDM and a background study. The background component will be further explored in Ch. 6. The filter algorithm identifies events with electromagnetic showers, and there is no restriction on the number of showers per event. This leads perfectly to an iBDM search. However, the degree to which an iBDM produces a shower that is identifiable by the filter has to be evaluated, in essence producing a filter efficiency distribution across various iBDM free parameter sets. Based on events that can pass the filter, a visual scanning team will have to be trained and their efficiency will need to be evaluated.

All other components of the atmospheric neutrino study, such as volume fiducialization, trigger efficiency, and other hardware-related aspects, are directly translatable to the iBDM search. This means a road map to successfully evaluate the detector for an iBDM search, and the execution for such a search is already favored because of the success of the atmospheric neutrino study.

In the coming chapters, the iBDM signal simulation, detector sensitivity for an iBDM interaction search, and visual data scanning results will be presented, demonstrating the impact the iBDM search with ICARUS at Gran Sasso has for future experiments.

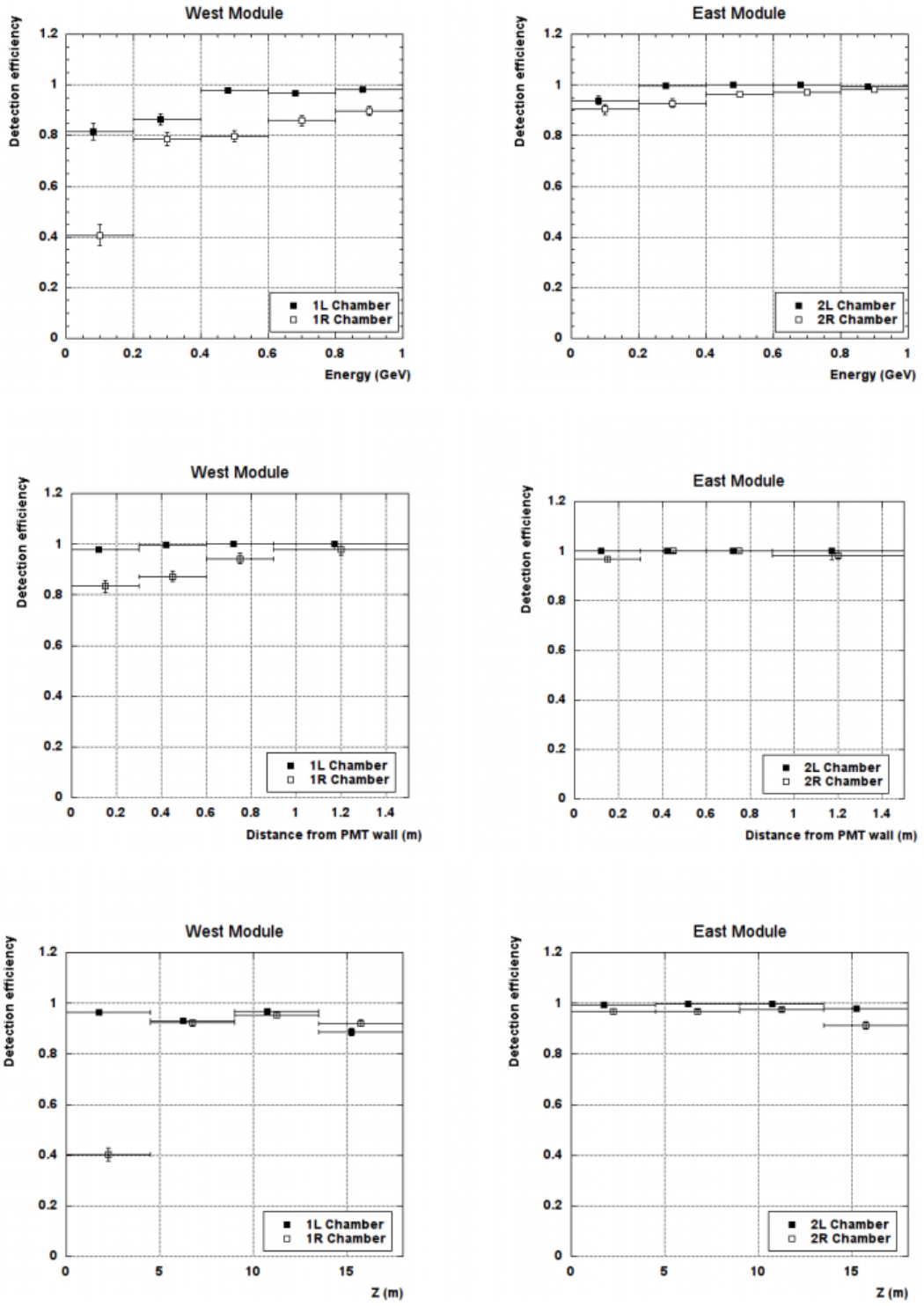

Figure 4.2: The PMT light detection efficiency as a function of energy(top), distance to PMT wall(middle), and along the Z direction of the detector(bottom) [56]. The efficiencies bin dependence at low energies ($\leq$ 400MeV) and distance to the PMT can be seen here. The west module has the lesser efficiency because this module had less PMT multiplicity compared to the east module, which, in general, has a more consistent efficiency across bins.

Chapter 5

iBDM Signal Simulation

The goal of this chapter is to present the methodology and tools necessary to simulate the wire response of the ICARUS detector due to an iBDM interaction inside the detector-sensitive volume called the fiducial volume (FV). The FV is a reduced volume in reference to the active volume and is implemented to circumvent detector inefficiencies close to the edge of the active volume or possible leakage of particles from outside interactions just outside the active volume. The production of simulated iBDM events and their corresponding detector response simulation is used for the detector sensitivity analysis (Ch. 7) and the visual scanning done for the real data (Ch. 8).

The ICARUS detector data readout works according to the principle that charged particles traversing the detector-sensitive volume ionize the liquid argon (LAr). An electric field applied to the sensitive volume will drift the ionization charge to wire planes. Resolving the ionization charge signals on the wires allows for a 3D reconstruction of the tracks with some reference initial time t_0. As the charge passes the induction planes and collects on the collection plane, the signals produced are registered as hits and are mapped to a Time vs Wire graph called an *event display*, creating the visual tracks. The mapping is done with detector-specific software that can take the wire signals, fit the charge vs time curve from the collection plane with a fit function, and label the peak as a registered hit [46, 61].

From Ch. 2, the complete iBDM process was presented. The full process takes the form:

$$\chi_1 e^- \rightarrow \chi_2 e_R^- \rightarrow \chi_1 (X^*) e_R^- \rightarrow \chi_1 (e^+ e^-) e_R^-. \tag{5.1}$$

The charged particles that produce visible tracks are the primary interaction ($\chi_1 e^- \rightarrow \chi_2 e_R^-$) recoil electron, e_R^-, and the secondary interaction ($\chi_2 e_R^- \rightarrow \chi_1 (X^*) e_R^- \rightarrow \chi_1 (e^+ e^-) e_R^-$) electron-positron pair ($e^+ e^-$). Depending on the energy allotted to the primary and secondary interaction, the tracks can be followed by electromagnetic showers and are labeled as the primary (e_R^-) shower and the secondary ($e^+ e^-$) shower. This signature is similar to the electron-neutrino charged current interaction explored in the atmospheric neutrino study in Ch. 4 Fig. 4.1. Electrons are minimum ionizing particles (m.i.p), and this characteristic is evident in the dE/dx at the beginning of the track before showering begins. However, in the case of both electron-neutrino and muon-neutrino charged-charged current interactions, there are more than one track leaving the interaction vertex. Most notably, the electron neutrino charged current interaction with the nucleus of the argon atom produces an ongoing electron that will shower, but also a non-m.i.p, higher dE/dx track that is the signature of a proton track [46]. All electron-neutrino events in the dataset for the present iBDM search that have been identified have more than one track leaving the interaction vertex [61].

The chapter starts with the components necessary to simulate the iBDM interaction in the ICARUS detector. Each step is then elaborated, with the culmination of the chapter being a demonstration of an event display showing the tracks left behind in the detector from an iBDM interaction.

5.1 Simulation Chain

To study the topology of the iBDM interaction in the ICARUS detector, a Monte Carlo simulation of the signal and detector response is performed with various programs/software so an event display for each wire plane can be constructed. The first step is to generate

the kinematics of the particles participating in the iBDM interaction and then subsequently transport the particles through LAr to obtain the detector response from the wire planes. The necessary software tools to perform these simulation tasks are categorized as the following:

- iBDM event generator: With the parameters of the model as input, a Monte Carlo for the kinematic information of iBDM events is developed via the characteristic distributions of the model (see Ch. 2).

- Particle Transport Simulator: using the kinematic information from the iBDM event generator, the particles are propagated in LAr, taking care of $Ar - e^{\pm}$ interactions, obtaining the ionization charged produced by the charged particles traversing the LAr.

- Detector Response Simulator: The ionization charge obtained from the transport simulation is then used to simulate induced signals on the wire planes with data-driven LAr purity and wire noise.

5.2 iBDM Event Generator

The iBDM event generator was created exclusively for LArTPC-type detectors. The team behind its creation used the code for a BDM sensitivity study for the future Deep Underground Neutrino Experiment (DUNE) far detector [64]. This paper contains the sole reference to the code used for this study. Minimal change to the code was necessary, requiring only changes in detector size and changes to the relative coordinate system. The latter is related to the particle transport discussed in the next section. The iBDM event generator code is compiled in C++ and has four main files:

- **width.h**: Contains functions for calculating the probability distributions for the BDM model

- **functions.h**: More functions relating to the parameter card, like detector characteristics and properties for the detector medium for the primary interaction cross-section

(for this study, argon).

- **param_card.txt**: The parameter card that contains the parameter values for the Monte Carlo generation such as the dark sector masses (m_0, m_1, m_2, m_X), the kinetic mixing parameter ϵ, the interaction couplings g_{11} and g_{12}, target type (e^-), the detector type (e.g cylindrical or parallel-piped), the detector dimensions, and the declaration of the number of simulated events desired.

- **main.c**: The main program that contains the event generation logic. The program calls upon all functions and parameter values from the headers files and the parameter card.

The libraries necessary to perform the event generation are contained in the CERN ROOT software libraries. ROOT is a C++ analysis package used to perform data analysis and simulations for high energy physics experiments [65].

The *main.c* program will simulate the number of events defined in the parameter card for set physics parameters ($m_0, m_1, m_2, m_X, \epsilon$) and save the event information in a text file in the high energy event format (HEPevt) [66]. Each Monte Carlo event has a set of rows in the text file, with the first row indicating the event number and the number of particles simulated. The following number of rows depends on the amount of particles simulated in each event. For iBDM, you either have 5 or 6 simulated particles, depending on the on-shell or off-shell condition for the dark photon(on-shell: $m_X < m_2 - m_1$).

Each row after the event number row contains the particle data group (PDG/pdg) code [14] and the kinematic information of the particle such as the particle four-momentum $p^\mu = (E, p_x, p_y, p_z)$ with momentum components first, mass, position in the defined volume, and the time of production ($t_0 = 0s$). Here is an example of an event in a file (figure 5.1)

```
3 5
-1 1000002 0 0 0 0 -1.514507537243185 1.184959599046706 0.5369400336803603 1.996629142200623 0.018999999938905741 -229.0947178796292 -146.6033183719447 532.0603970205411 0.0
0 1000001 0 0 0 0 -0.8264136783111063 0.6473063104590022 0.2952410449925378 1.090519280849061 0.0099999999776482582 -277.8742836662909 -108.4378993860148 549.3542704759876 2.145078518846036
1 11 0 0 0 0 -0.001485049559177423 0.003315395673897528 0.001269046219358788 0.003881857799376522 0.00051100000000004 -229.0947178796292 -146.6033183719447 532.0603970205411 0.0
1 11 0 0 0 0 -0.5355939524729203 0.4149952222882146 0.1897867752767516 0.7036342783282787 0.000511 -277.8742836662909 -108.4378993860148 549.3542704759876 2.145078518846036
1 -11 0 0 0 0 -0.1524999064591585 0.1226580662994891 0.05191221341107097 0.2024755830232834 0.000511 -277.8742836662909 -108.4378993860148 549.3542704759876 2.145078518846036
```

Figure 5.1: A screenshot of one event's data in a Monte Carlo generated HEPevt text file.

The pdg codes seen on the left-hand of Fig. 5.1 are defined as follows:

$$\mathbf{1000001} = \chi_1,\ \mathbf{1000002} = \chi_2,\ \mathbf{1000003} = X,\ \mathbf{11} = e^-,\ \mathbf{\text{-}11} = e^+. \tag{5.2}$$

In Fig. 5.1, the 1000003 pdg code for the dark photon is not shown because the parameter set used for this batch of events contained off-shell ($m_X > m_2 - m_1$) dark photons.

The sections filled with zeros are reserved to indicate how many parent or daughter particles are in the respective row. Although these columns are included for consistency when the file is eventually fed into detector simulation software packages that depend on the HEPevt file format, they never change from null.

A Python script was developed to take parameter lists as input, overwrite the parameter card, and run the Monte Carlo generator C++ executable for each parameter set. At the same time, for more efficient event generation, Python scripts run in parallel in the terminal to span various DM (m_0, m_1, m_2) masses over the (m_X, ϵ), and vice versa.

5.3 Detector Simulation

The detector simulation uses the kinematic information generated by the iBDM event generator to simulate the behavior of particles in the LAr and the response of the wire planes on the ionization charge liberated by the interactions of the charged particles with LAr. The detector simulation chain has the following main components:

1. Particle Transport in LAr
2. Format Conversion for ICARUS at Gran Sasso
3. Wire Response and Noise Simulation

The ultimate goal of the simulation chain is to have sample iBDM events to study topologically and kinematically for the assessment of the selection efficiency given some established

selection criteria, trigger efficiency, filter algorithm efficiency, and scanning efficiency. Each of these factors affects the detector's sensitivity in the mass (m_0, m_1, m_2) and dark photon (m_X, ϵ) parameter space.

In the following sections, the three detector simulation components will be elaborated on. The chapter will culminate with an event display of a simulated iBDM event, displaying the expected topology of the iBDM signal in this study's dataset.

5.3.1 Particle Transport

The particle transport simulation software used by ICARUS during its operation at LNGS was outdated. Fortunately, the ICARUS collaboration at Fermilab has adopted the modern, general LArTPC detector simulation package named LArSoft [67]. The working group for this software proposes the goal of housing a cohesive analysis framework for future LArTPC experiments [67].

The LArSoft version for the ICARUS detector is named *ICARUScode*. The specific ICARUScode version used for the analysis was v09_75_00. The software contains a particle transport simulation developed at CERN called Geant4 [68]. Geant4 requires a detector geometry file and detector medium characteristics. To this end, ICARUScode contains configuration files based on Fermilab's Hierarchical Configuration Language (FHiCL) with the extension "*.fcl*". These configuration files call upon the detector geometry files, which have a "*.gdml*" extension. Since Geant4 is integrated into ICARUScode, a configuration file encapsulates the following simulation actions

1. Run G4 configuration file on the iBDM event HEPevt file

2. The configuration file calls upon detector characteristics via other configuration files, setting up the detector environment

3. Using the kinematic information from the HEPevt file, Geant4 simulates LAr-$e^{\pm}$ interactions and obtains the ionization charge.

The output of Geant4 simulation is a "*.root*" file with ionization charge information produced during the transport of charged particles traversing the detector. In the case of iBDM, the charged particles that are transported are the recoil electron from the primary interaction and the electron-positron pair for the secondary interaction.

5.3.2 Detector Wire Simulation

The output *.root* file containing the information on the ionization charge caused by the propagation of charged particles through LAr (in the case of iBDM $e_R^- + e^+ e^-$) is subsequently fed to the wire simulation of the ICARUS detector at Gran Sasso. The conditions of the hardware is not exactly the same as the ICARUS at Fermilab, therefore, the wire simulation used during the detector's operational run at Gran Sasso must be used.

The legacy wire simulation software exists in a virtual machine saved by the ICARUS collaboration and was passed down to UTA to simulate the wire response from the ionization charge simulated in the G4 stage. Several Python scripts to automate the process for large batches of G4 *.root* files was developed. The output folders from the scripts would contain the necessary file format for the legacy software in the virtual machine. Once the legacy software was run on the simulated ionization charge data, wire signals labeled as "hits" were simulated from the ionization charge information. This stage of the simulation takes the most time, averaging 12 hours for 5000 events, which can vary from computer to computer due to the possible difference in hardware specs. Running multiple instances with a multi-core, multi-threaded computer allowed for a reasonable time of completion and exploration of multiple $(m_0, m_1, m_2, m_X, \epsilon)$ parameter space points unexplored by previous experiments. Details on how the parameter space is explored are explained in Ch. 7.

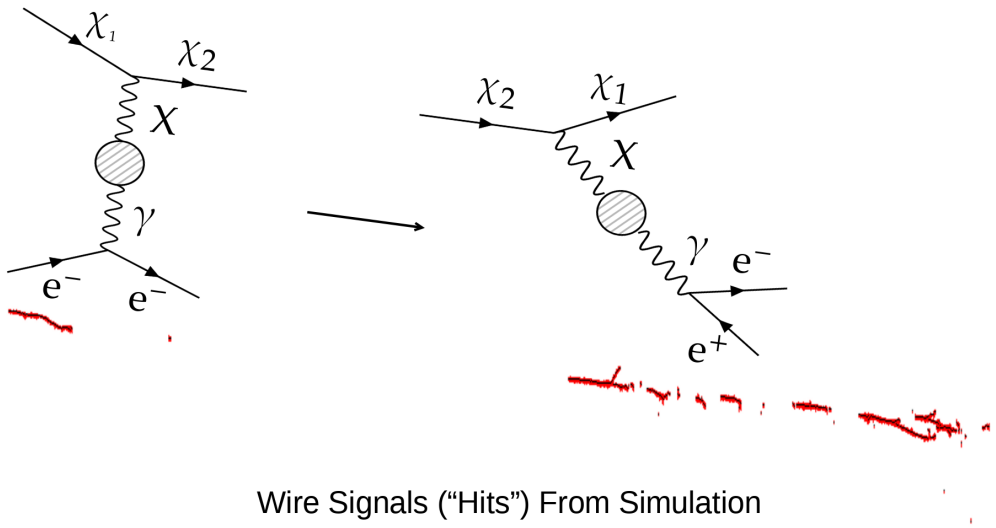

Figure 5.2: Simulated iBDM event with the wire noise removed in the event display for faster simulation and less memory usage. The right-most interaction is the primary interaction $\chi_1 e^- \to \chi_2 e^-$ followed by the left-most interaction, which is the secondary interaction $\chi_2 \to X^* \to e^+e^-$. X^* indicates that the dark photon can be on-shell ($m_X < m_2 - m_1$) or off-shell($m_X > m_2 - m_1$).

5.4 Event Visualization

After each event goes through the wire and noise simulation stage, the output information is the wire signal, and the format is an *.root* file. This file can be analyzed to graph the wire hits on a 2D plane that maps the wire signal on with Time vs Wire called the event display. The software used for this analysis was the same software used for the majority of ICARUS Gran Sasso analysis, *Qscan*. The program is very versatile, allowing for hit finding and reconstruction, the latter possible by referencing a point in all wire plane event displays. This is done by cross-referencing the hits on the wire planes with the time they were recorded.

Figure 5.2 shows an example of an iBDM event display using Qscan. The event display was stripped of its wire noise and the wire hits have been highlighted in red. For clarity, the portions of the display pertaining to the different iBDM interactions are labeled (primary (e_R^-) and secondary (e^+e^-) interactions). The event display in Fig. 5.2 This is an example of an iBDM event where the recoil electron is identifiable by a dE/dx analysis of the beginning

of the track as an m.i.p, and the electron-positron pair is also identifiable by its 2 m.i.p signature. This is possible due to a minimum separation between the primary and secondary interaction vertex. The declaration and implementation of selection criteria are presented in Ch. 7. The full event display with wire noise and detector boundaries are the examples trained on by scanners for the eventual iBDM search in the real dataset.

Chapter 6

Background Estimate

Chapter 5 describes how to simulate the iBDM interaction and obtain wire signals in the detector. An example of what results at the end of the simulation chain is seen via the event display in Fig. 5.2. The particles visible in the detector are the recoil electron e_R^- from the primary interaction and the electron-positron pair e^+e^- from the secondary interaction. The figure shows the primary and secondary interaction Feynman diagrams next to the corresponding hit signals induced by the ionization charge drifting to the collection plane.

High energy cosmic rays (CRs) still reach the ICARUS detector, causing the trigger to activate, despite the $\sim 10^6$ reduction of CR flux enabled by the 3400 m.w.e overburden of the Gran Sasso mountain rock over LNGS [61]. Muons are a significant background for the search of the iBDM interaction in the ICARUS detector because muons can produce electromagnetic showers by way of bremsstrahlung photons and delta rays. Additionally, the overburden can significantly reduce the incoming energy of muons, enabling muons to "sneak" into the detector-sensitive volume and mimic electron tracks [34].

Atmospheric neutrino interactions can also induce background signals from electromagnetic showers from electrons through ν_eCC interactions and muon backgrounds from ν_μCC interactions. In the atmospheric neutrino analysis, ν_eCC and ν_μCC events were filtered by the application of filter algorithm identified [61]. The same filtered dataset used to identify

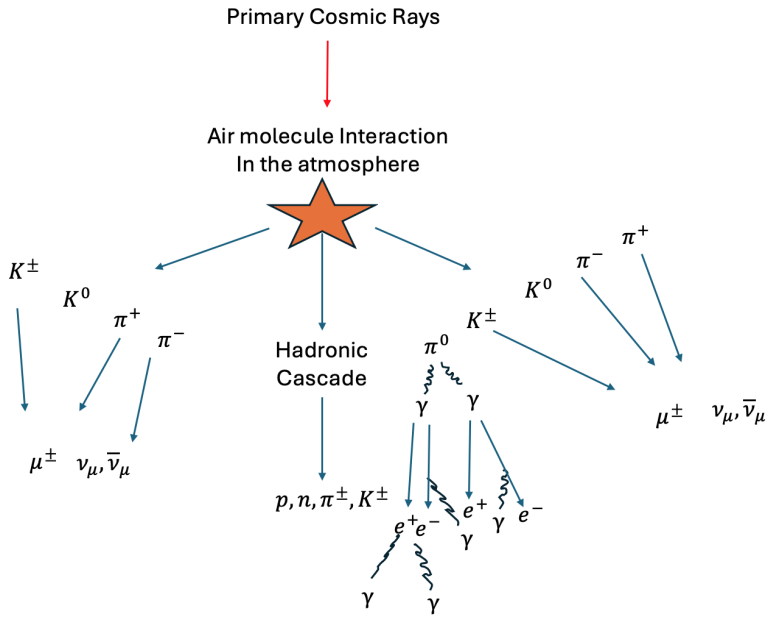

Figure 6.1: A Diagram showing the process of how primary CRs, such as protons, interact with nuclei of molecules in the atmosphere to produce the secondary CR particles. The secondary particles include CR muons (μ) and atmospheric neutrinos (ν_μ and ν_e).

the charged-current neutrino events for the atmospheric neutrino study is used as the dataset for the iBDM search.

This chapter outlines the backgrounds on the iBDM signal in the ICARUS detector at LNGS from CRs muons, atmospheric neutrinos, and the CERN Neutrinos at Gran Sasso (CNGS) beam neutrinos and describes the background mitigation strategies that enable a background-free dataset.

6.1 Origins of Cosmic Ray Backgrounds

CRs (CR) are split into two categories, primary and secondary CRs. Primary CRs are the particles that interact in the atmosphere and create secondary particles, such as kaons ($K^{\pm}$) and pions ($\pi^{\pm}$) [63]. This process is shown in Fig. 6.1, after the primary CRs interaction with the nuclei of the atoms that make up Earth's atmosphere. The kaons and pions decay to produce *CR muons*, *atmospheric neutrinos*, and electromagnetic showers [63] from the

photons produced by neutral pion decay ($\pi^0 \rightarrow \gamma\gamma$). Although ICARUS at LNGS had a rock overburden of 3400 m.w.e, the weak coupling of neutrinos with matter and the high energy penetration power CR muons enable these particles to penetrate the large overburden and enter the detector sensitive volume [61, 63, 69].

6.2 Background Signals

Neutrinos and muons interact with the LAr with the potential of inducing shower activity from interactions such as:

- Neutrino Charged-Current and Neutral Current Interactions [61]: Neutrinos can interact with the nucleus of the argon atom through charge-current interactions (ν_eCC and ν_μCC). This process takes the general form $\nu_l N \rightarrow lN' + X$, where l is the lepton flavor of the neutrino ($l = e, \mu, \tau$), N is the nucleon, and X are nuclear fragments from the interaction. There can also exist neutral current interactions such as $\nu e \rightarrow \nu e$. There are two possible sources of neutrinos in ICARUS at Gran Sasso: The CERN Neutrinos at Gran Sasso (CNGS) beam and the atmospheric neutrinos.

- Delta Rays [70]: In addition to creating ionization charge, muons that traverse the detector can knock off electrons from the argon atoms that create their own ionizing tracks in the detector. These electrons are called delta rays and can mimic the iBDM primary interaction and produce subsequent showers that mimic the iBDM secondary interaction.

- Sneak in Muons [34]: muons with low enough energy can have electron-like tracks. Electrons and muons are both minimum ionizing particles (m.i.ps). The only difference (generally) is that muons will appear linear, as opposed to the scattering an electron takes while traversing the LAr. At low enough energies, the muon track still has the m.i.p signature and gains the scatter-like behavior of electrons traversing the LAr.

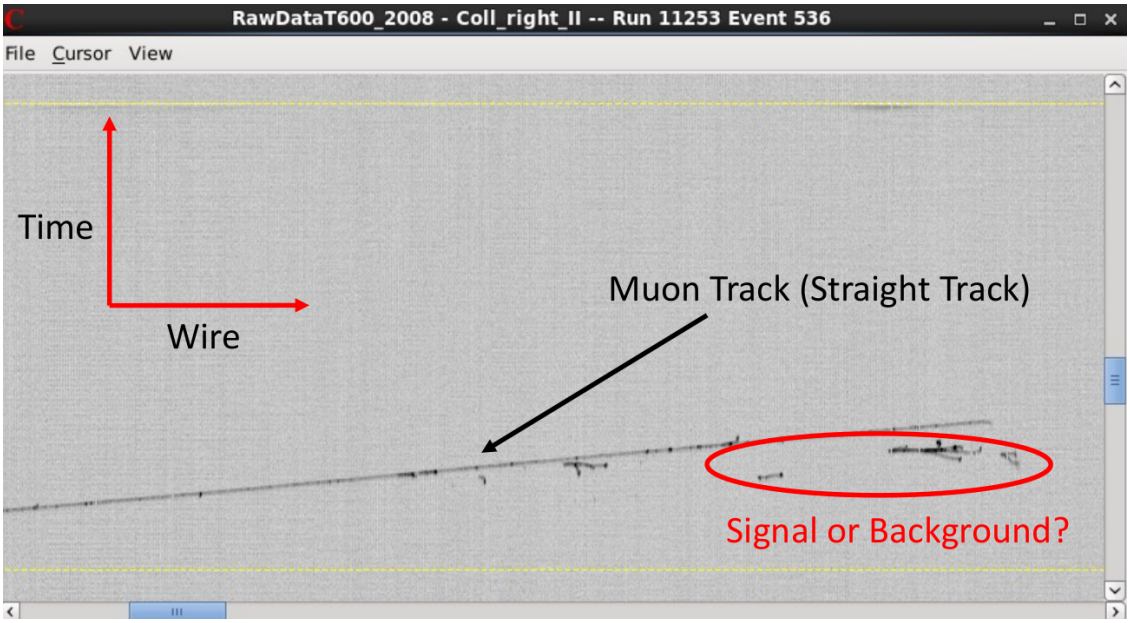

Figure 6.2: Run 11253 Event 536 Collection view event display with the Qscan software. Compared to the simulated iBDM event in figure 5.2, the tracks circled in red above have the visual signature of iBDM. The long straight track is a cosmic muon. The δ rays seen around the track have a possible primary interaction signature. This is a clear example of why it is necessary to reject events with an identified muon.

Each type of background above has an outgoing electron in the final part of the processes, leading to potential showers and there for potential backgrounds for both the primary and secondary iBDM interaction.

In this chapter, the backgrounds are explored and their impact on the analysis is presented.

6.3 Cosmic Ray Muons Background Estimate

CR muon tracks are straight tracks that enter the extremities of the detector. CR muons either have enough energy to go through the entire detector TPC volume (through-going muons) or after traveling some distance in the TPC volume, the muon decays into an electron and neutrinos, $\mu^- \rightarrow e^- \nu_\mu \bar{\nu}_e$ (stopping muons).

An example of a through-going muon crossing the detector TPC with delta rays sur-

rounding the track is shown in Fig. 6.2. The wire plane information is displayed here using an event display. Event displays graph the Time vs Wires of each wire plane, which in the case of Fig. 6.2 is the Collection plane. Wires along each wire plane will have a signal induced on them from the event, and it is the procedure of processing the signal of the wires over time that gives an image of a particle track in the detector.

Delta rays, which are knocked-off electrons caused by muons interacting with the argon electrons, are generally present along the muon track, indicating the direction of travel of the muon [70] for both through-going muons and stopping muons. Delta rays with energies that are equal to or greater than the trigger threshold energy of 200 MeV have the ability to create shower activity comparable to the primary or secondary iBDM interaction and mimic the iBDM signal. Delta rays with energies above 200 MeV are rare but significant at the level of other rare interactions, such as the iBDM interaction. The tracks circled in red in Fig. 6.2 are tracks that resemble the iBDM signal simulation example presented in Fig. 5.2. Without further information, it is difficult to ascertain whether these tracks are delta rays or an iBDM candidate event.

Muons that "sneak" into the detector are a potential background because they appear in the detector seemingly without crossing the detector boundaries, mimicking how the iBDM primary interaction appears in the detector. If the "sneaking in" muon has enough energy to interact electromagnetically with an argon nucleus and induce bremsstrahlung photons that subsequently electromagnetically shower, that mimics the iBDM secondary interaction, therefore producing a scenario where the complete iBDM interaction is mimicked. The MicroBooNE collaboration, a LArTPC operating at Fermilab under the Short Baseline Neutrino program, performed a study [71] concerning off-beam, fully contained tracks, about 0.9% of these tracks fit the description of a "sneaking in" type of cosmic muon. The MicroBooNE LArTPC is a surface-based detector, making it susceptible to a higher muon flux, as opposed to the underground nature of ICARUS at LNGS. The underground nature of the ICARUS detector suppresses the "sneaking in" muon background to essentially zero.

All in all, CR muons interact with LAr in a few ways that leave tracks similar to the iBDM track signatures in the detector-sensitive volume. The backgrounds that are significant in the search for iBDM in the ICARUS detector are the delta rays that are energetic enough to produce the iBDM primary and secondary interaction signatures and "sneak" in muons, which can subsequently interact with the LAr nucleus through bremsstrahlung, enabling the production of a hard photon mimicking the primary interaction ("sneak" in muon) and secondary interaction (hard photon).

If the muon is identified in an event, the conservative approach is to reject the event automatically to avoid the delta ray background presented in Fig. 6.2. Given the rarity of "sneak" in muons and the energies at which they interact with the detector [71], this background can be circumvented by implementing an appropriate fiducial volume [34].

The probability of randomly finding a CR muon in any readout window is given by the CR muon rate multiplied by the duration of the trigger readout window. ICARUS at LNGS obtained the rate of identifiable CR muons reaching the detector [61]. The cosmic muon rate measured in each ICARUS module over the operational period of 2012-2013 is shown in Fig.) 6.3. The different colors represent the two ICARUS T-300 modules. Each module has its own PMT trigger system, where one module has more PMTs. This is evident in Fig. 6.3 because of the difference in rates recorded. The module with more PMTs has a more sensitive trigger, thereby enabling a more efficient trigger overall.

Taking the combined rate for both T-300 modules, the total muon rate for the whole ICARUS detector is $\Gamma = 32mHz$ [61]. Using the readout window $t_{drift} = 10^{-3}s$ and $\Gamma = 32mHz$, gives an estimate on the probability of a muon reaching ICARUS within a readout window

$$P(\mu|t_{drift}) \sim \Gamma t_{drift} = 3.2 \times 10^{-5} \tag{6.1}$$

This means that rejecting all events with an identified muon reduces the exposure by $\simeq 3$ parts in 100,000. Given the significant risk of backgrounds produced by muons, it was decided to reject any event in which a muon is identified. This would have minimal impact

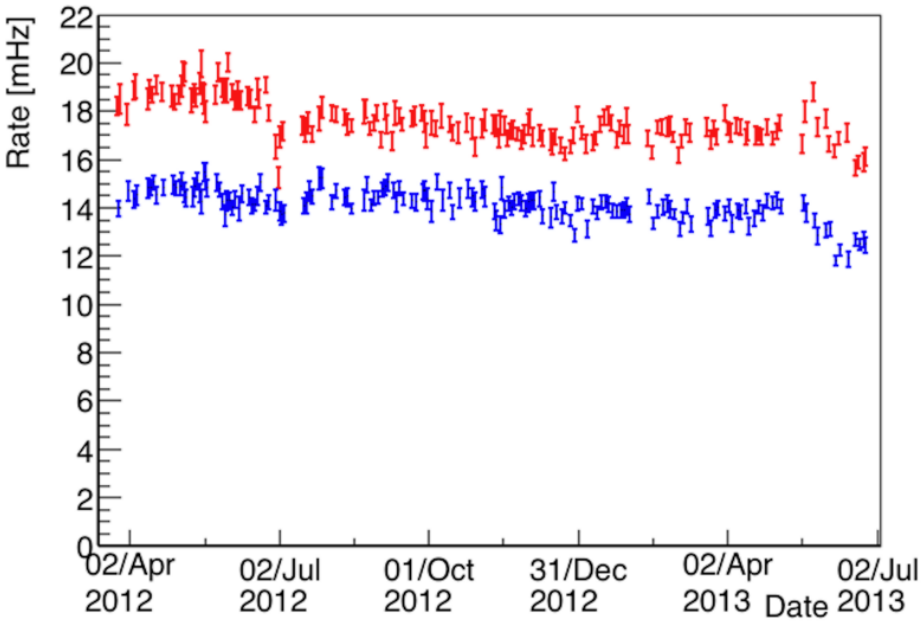

Figure 6.3: Muon rates measured by ICARUS at Gran Sasso [61]. The red points are the east cryostat, and the blue points are the west cryostat. The west and east modules have different numbers of PMTs (Fig. 3.3), resulting in slightly different efficiencies (Fig. 4.2).

on the overall detector exposure.

As a cross-check, the MACRO experiment [72] was also located at Gran Sasso and the experiment reports a muon flux of 1 muon $m^{-2}h^{-1}$ in the underground laboratory. Multiplying this by the X-Z area of the East and West ICARUS detector modules gives a muon rate of 44mHz. This rate is within 25% of ICARUS's measured muon rate and supports the decision to exclude any events with a muon with minimal impact on the exposure.

6.4 Atmospheric Neutrino Background Estimate

The atmospheric neutrino study performed with the ICARUS detector at Gran Sasso identified neutrino charged-current interactions that include $\nu_e n \to p e^-$ and $\nu_\mu N \to \mu^- X$, where X here is other particles that arise from the nuclear break up(Ch. 4). Noting that the exposure for this iBDM search is 1/3 that of the atmospheric neutrino study (0.13 kton·year) and applying the data from Table 7.1, a total of 1.3 ν_μCC, 4 ν_eCC, and 0.4 NC interactions

are expected in the data sample used the this iBDM search. Conservatively, the atmospheric neutrino background is estimated at 6 events, mostly due to ν_eCC interactions.

The ν_eCC interaction that has been identified in the atmospheric neutrino study is $\nu_e n \rightarrow pe^-$. The interaction is an event with two tracks originating from a single vertex. One track is an electron track, which subsequently showers, and the second track is a proton track that has a higher dE/dx compared to m.i.p characteristic of the electron track (Fig. 4.1). If the proton is not visible, there still needs to be a e^+e^- conversion after the electron track to be considered as background. There was only one case in the atmospheric neutrino study where an electron produced a shower in the middle of the detector with no visible proton at the vertex. However, there is no subsequent secondary interaction to label this event as an iBDM candidate.

The charged current muon-neutrino ν_μCC interaction shows up in the detector as a long muon track leaving an interaction vertex, along with other particles labeled as nuclear fragments. Therefore, both ν_eCC and ν_μCC are identifiable with extra vertex activity from just an electron track or muon track. This fact makes the neutrino charge-current interaction distinguishable from the iBDM interaction signal.

The $\nu e^- \rightarrow \nu e^-$ elastic scattering case results in a single electron track like an iBDM primary interaction. The electron can radiate a photon, which converts some distance from the primary shower, producing the second shower, mimicking the iBDM signature ($e^- + e^-e^+$). This is a potential background for the elastic-boosted dark matter (eBDM) case. In fact, no events of this kind were reported by the ICARUS collaboration for the atmospheric neutrino study.

6.5 CNGS Beam Background Estimate

The ICARUS experiment collected CNGS beam neutrino interactions with a dedicated trigger system that utilized the sum of PMT signals together with the CNGS beam "early warn-

ing" signal of an imminent proton extraction from the Super Proton Synchrotron, 2 spills of 10.5 μs time width, separated by 50 ms, every 6 seconds [56]. The time synchronization between CERN and Gran Sasso had 1% – 4% inefficiencies due to missing "early warning" messages, causing potential beam neutrino events incorrectly tagged as those recorded out of the 60 µs readout window, such as the atmospheric neutrino events. These events, however, were recovered and correctly tagged as the CNGS neutrino beam events through an offline procedure that compares the event timestamp with the beam spill extraction time database. Since the total readout window for the CNGS neutrino the beam was 120 µs, every 6 seconds, the total fractional loss of the acceptance of the iBDM data sample is 2 $\times 10^{-5}$ with the associated inefficiency much less than 1%. Given the negligible acceptance loss, we take the conservative approach and removed any events triggered within the CNGS beam data readout time window to fully eliminate the backgrounds from CNGS neutrino interactions.

Chapter 7

Detector Sensitivity Analysis

The topology and kinematics of the iBDM interaction depend on the 7 parameters of the BDM model [30]

$$m_0, m_1, m_2, m_X, \epsilon, g_{11}, g_{12}. \tag{7.1}$$

In order to evaluate the detector sensitivity for the search of iBDM, a systematic method to span the various model parameters was devised. A parameter group structure was implemented to easily manage a fix-and-vary strategy. The parameters groups are labeled as the DM masses (m_0, m_1, m_2), the dark photon parameters (m_X, ϵ), and the interaction couplings (g_{11}, g_{12}). Each of these parameters can be

The chapter starts off with the strategy to explore the mass parameter sets that maximize the ICARUS detector sensitivity in the dark photon space. The results for the ICARUS detector sensitivity study in the (m_X, ϵ) parameter space for various (m_0, m_1, m_2) mass sets that are identified as optimal mass parameter sets are presented and show that the ICARUS T-600 at the Gran Sasso Underground National Laboratory is capable of exploring new parameter space for multiple mass sets.

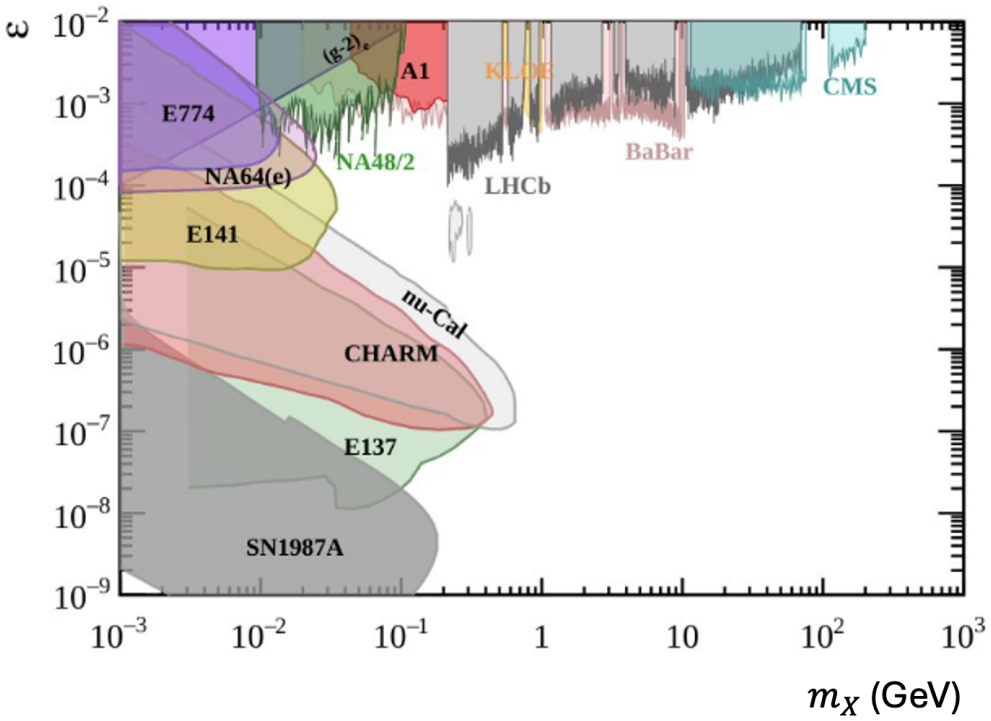

Figure 7.1: The covered(colored regions with experiment abbreviations) and available (white space) parameter space in the kinetic mixing vs dark photon mass space [32]. The colored regions are parameter space already explored by the respective experiment abbreviated.

7.1 Parameter Constraints

The interaction couplings identify with the type of interactions possible, namely elastic boosted dark matter (eBDM) for g_{11} and inelastic boosted dark matter (iBDM) for g_{12}. In this analysis, the χ_1 and χ_2 DM particles take the two chiral fermion scenario as a benchmark physics case [33]. The results of this analysis remain applicable to generic iBDM models. In this type of scenario, the relative proportion of the interaction couplings (g_{11}, g_{12}) depends on the eigenvalues of the DM masses (m_1, m_2), which consist of a Marjoana component and a Dirac component. The sum of the two interaction coupling parameters squared normalized by the dark-sector cooling g_D is equal to one [33]:

$$\left(\frac{g_{11}}{g_D}\right)^2 + \left(\frac{g_{12}}{g_D}\right)^2 = 1. \tag{7.2}$$

There is a possible scenario in which the g_{11} parameter is suppressed($g_{11} \sim 0$). In this scenario, the interaction couplings take the values $(g_{11}, g_{12}) = (0, 1)$, making iBDM the dominate interaction. By fixing the interaction couplings, there are now 5 free parameters: the DM masses (m_0, m_1, m_2) and dark photon parameters (m_X, ϵ).

Despite the wide range of values available for the mass parameters and dark photon parameters, there are limits based on the results of the current experiments on the interaction of DM with the detector medium, both for direct detection [73] and indirect detection. Due to the fact that χ_1 DM particles are produced by the self-annihilation of χ_0 ($\overline{\chi_0}\chi_0 \rightarrow \overline{\chi_1}\chi_1$), the mass parameter sets are inter-dependent, with m_0 dictating the energy range χ_1 and, therefore also its mass m_1. The χ_0 particle is the abundant DM, responsible for the gravitational anomalies, as seen at various scales of the Universe. Ascribing WIMP-like properties to χ_0(Ch. 2) [24,30], it is of interest to indirectly search for masses in the 1-10 GeV mass range(Fig. 2.3). The iBDM primary interaction involves a DM inelastic up-scattering interaction. This interaction involves a DM flavor change $\chi_1 \rightarrow \chi_2$, thereby also making the χ_2 mass dependent on the kinematics of χ_1 with the electrons of the argon atoms in the detector.

Figure 7.1 shows the (m_X, ϵ) parameter space already covered by various experiments looking for dark photons decaying into visible decays (SM particles) [32]. The dark photon parameters have been explored by many experiments for the search of visible decays. Visible decays are processes in which the dark photon decays to charged Standard Model particles such as an electron-positron pair, or a muon-antimuon pair. Invisible decays are those in which the dark photon produces dark sector particles, $X \rightarrow \overline{\chi}\chi$. The focus of this analysis is the iBDM interaction in which the dark photon decays visibly; in particular, the primary interaction reads $\chi_1 e^- \rightarrow \chi_2 e_R^-$, and the secondary interaction reads $\chi_2 \rightarrow \chi_1(X^*) \rightarrow \chi_1 e^+ e^-$. The electrons and the positron create tracks through ionization and shower through bremsstrahlung.

7.2 Study I: The Primary Interaction

The primary interaction is an up-scattering, inelastic interaction that enables χ_1 to flavor change into the excited state χ_2. The χ_2 particle is unstable and will inevitably decay back to a χ_1 via $\chi_2 \to \chi_1(X^*) \to \chi_1 e^+ e^-$. Therefore, the secondary process is guaranteed if the primary interaction takes place.

The m_0 mass, due to its self-annihilation, sets the kinematics for the whole iBDM interaction. The first step in the analysis is, therefore, to understand the possible coverage of the ICARUS detector in the (m_X, ϵ), assuming all primary interactions lead to a full iBDM event that can be identified and reconstructed as an iBDM event. This will effectively show the maximum sensitivity for a given (m_0, m_1, m_2) in the dark photon space and serve as a reference for the different analyses presented in the rest of the chapter. The evaluation of the detector sensitivity in the dark photon space is performed by requiring a 90% Confidence Level (C.L) condition using Poisson statistics, which states that the number of iBDM events exceeds or equals 2.3 events with a no background assumption.

The conditions for this analysis are:

1. The primary and secondary interaction can be seen, despite their possible large distances from each other

2. The properties of the detector, such as electrons in the fiducial volume (FV) and detector exposure time, are used to have an estimate for the number of primary interactions

3. The detector and following reconstruction analysis is viewed to be 100% efficient with only the FV under consideration, thereby making this sensitivity analysis an upper limit in the (m_X, ϵ) parameter space.

The theoretical number of primary interactions is given by

$$N_{primary} = N_e \times t_{exposure} \times \mathcal{F}_{\chi_1} \times \sigma_{\chi_1 e^- \to \chi_2 e^-} \tag{7.3}$$

where N_e is the number of target electrons, $t_{exposure}$ is the detector exposure time in seconds, $\mathcal{F}_{\chi_1}$ is the flux of χ_1 from the galactic center, and $\sigma_{\chi_1 e^- \to \chi_2 e^-}$ is the primary interaction cross section.

The number of available electrons for the primary interaction N_e is set by the number of argon atoms in the fiducial volume (FV). The FV is the sensitive detector volume that implements cuts to the active volume. These cuts incorporate background considerations and detector inefficiencies at every dimension extremum. These considerations lead the atmospheric neutrino study to implement a reduction for all active volume dimensions of each ICARUS module by 5 cm, resulting in FV dimensions for each module as:

$$\begin{aligned} X &= [-353.73,\ -66.7]\ cm \to 287.03\ cm \\ Y &= [-176.86,\ 134.96]\ cm \to 306.82\ cm\ \ (Fiducial\ Volume) \\ Z &= [-889.95,\ 889.95]\ cm \to 1780.00\ cm \end{aligned} \tag{7.4}$$

With the fiducial volume dimensions, the number of electrons available N_e for the primary interaction is obtained using the LAr density properties at 89K [40].

The data used for this analysis is 1/3 the filtered dataset of the atmospheric neutrino study amounting to 0.13 kton· year [61], which corresponds to $t_{exposure} \sim 0.3$ years. The filter algorithm used for the atmospheric neutrino study is already applied to this dataset, therefore the filter efficiency for each iBDM parameter set must be obtained to calculate the number of expected events properly. The application of the filter is postponed to the end of the chapter when the detector efficiencies will be established.

The χ_1 flux from the galactic center is [30, 34]

$$\mathcal{F}_{\chi_1} = 1.6 \times 10^{-4}\ cm^{-2} s^{-1} \left(\frac{\langle \sigma v \rangle_{0\to 1}}{5 \times 10^{-26} cm^3 s^{-1}} \right) \left(\frac{GeV}{m_0} \right)^2 \tag{7.5}$$

where $\langle \sigma v \rangle_{0\to 1}$ is the thermally averaged cross section for the annihilation process $\overline{\chi}_0 \chi_0 \to \overline{\chi}_1 \chi_1$. The thermally average cross section takes the typically observed value $\langle \sigma v \rangle_{0\to 1} \sim$

$5 \times 10^{-26} cm^3 s^{-1}$ [7,30,34]. This parameter can be kept fixed, regardless of the effective scale of the BDM theory as the scale can be reinterpreted provided that there are no asymmetries in the DM particle species [30]. Also, the mass range for m_0 is kept at the same order of magnitude, therefore, fixing $\langle \sigma v \rangle_{0 \to 1}$ at the same magnitude for the whole analysis as well. The χ_1 flux from the galactic center is inversely proportional to the square of χ_0 mass (eq. 2.58). This implies that increasing the abundant dark matter mass m_0 will ultimately reduce the detector sensitivity space by a $1/m_0^2$ factor. In direct DM searches, a larger mass is preferred due to the associated nuclear recoil energies [73]. However, this analysis is looking for the lighter DM component χ_1 that has a significantly lower mass ($m_0 \gg m_1$), but is boosted, capable of interacting electromagnetically through the kinetic mixing of the dark photon and the Standard Model Photon [33].

Lastly, the primary interaction cross-section is expressed as

$$\sigma_{\chi_1 e^- \to \chi_2 e^-} = \int_{E_R^{min}}^{E_R^{max}} \frac{d\sigma}{dE_R} \, dE_R \tag{7.6}$$

where E_R is the recoil electron energy, E_R^{min} and E_R^{max} are the possible minimum and maximum recoil electron energy, and $\frac{d\sigma}{dE_R}$ is the primary interaction differential cross section explicitly expressed in Ch. 2, Eq. 2.62 [33].

The above discussion encapsulates all parameters necessary to estimate $N_{primary}$ for the primary interaction. Imposing a Poissonian 90%C.L condition on $N_{primary}$, the outcome sensitivity looking at only the number of events expected from the primary interaction in the (m_X, ϵ) parameter space. We pick some reference values for the mass parameter sets (m_0, m_1, m_2). Here is the procedure for this preliminary study:

1. The WIMP low mass range is of particular interest due to direct detection experiments having trouble resolving sub-keV energy depositions [73], which can be seen in Ch. 2, Fig. 2.3. Therefore, we select $m_0 =$ 1 GeV, 2 GeV, 5 GeV, 10 GeV.

2. We use the χ_1 and χ_2 mass reference values (m_1, m_2)= (10 MeV, 15 MeV), (20 MeV, 25 MeV),

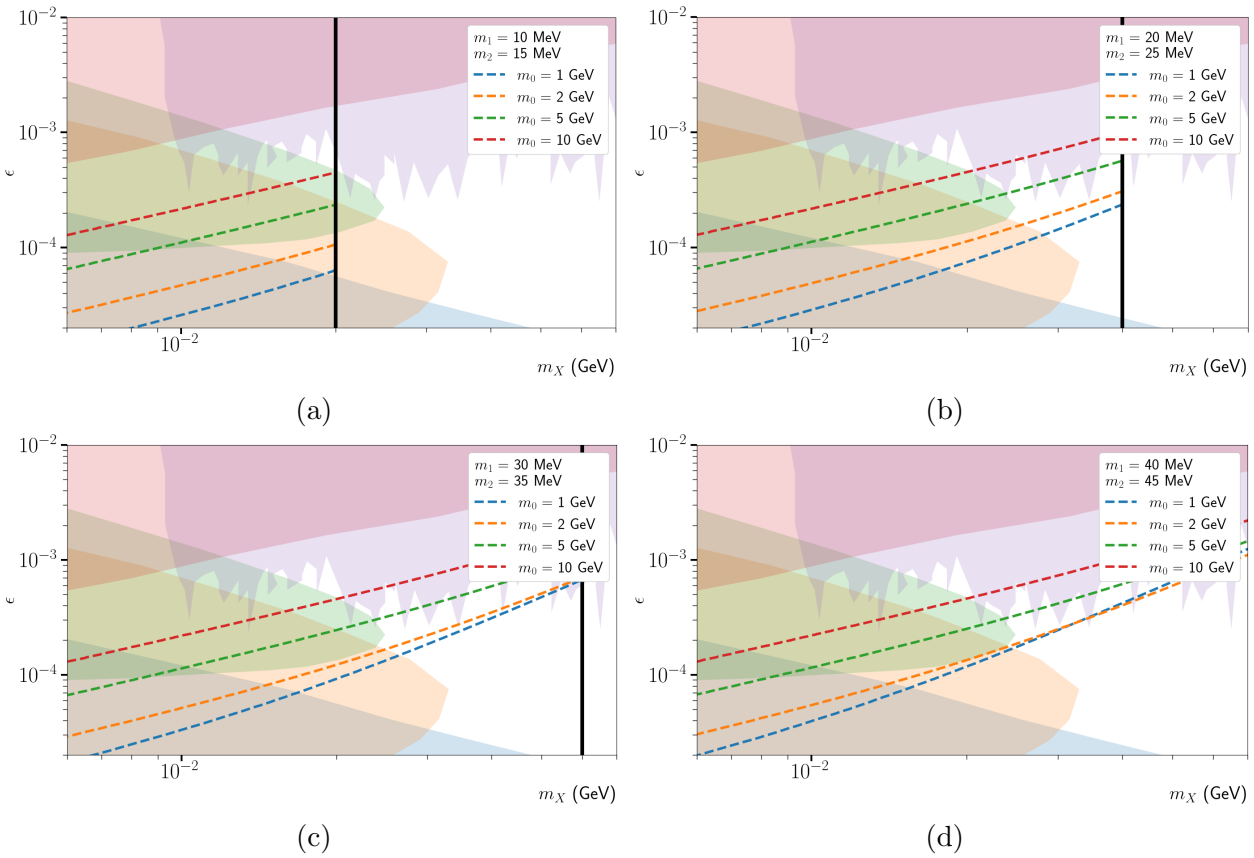

Figure 7.2: Sensitivity plots for the 0.13 kton· year exposure for (m_1, m_2) mass sets indicated in the legend of the graphs. Each colored dashed line is a different m_0 mass indicated in the legend. Each line represents the 90% C.L, The colored areas were digitized from the data of Fig. 7.1 and consist of beam dump experiments (e.g., nu-Cal [74], E141 [75])and collider/fixed target experiments (e.g., NA64(e) [76], NA48/2 [77]). The experiment associated with each colored area is indicated in the legend.

(30 MeV, 35 MeV), (40 MeV, 45 MeV).

3. Calculate $N_{primary}$ for a given (m_X, ϵ) point.

4. Draw sensitivity curve satisfying 90% C.L under the assumption of Poisson statistics, no observed events $N_{obs} = 0$, and $N_{primary} \geq 2.3$.

The results of the analysis are in Fig. 7.2. The four plots show the primary interaction sensitivity curves for four sets of (m_1, m_2) defined in (2) above, and each of the dashed lines corresponds to one of the four values of m_0 from 1GeV to 10GeV defined in (1). The shaded regions are excluded parameter space that was digitized from the graph in Fig. 7.1 with

the experiments nu-Cal [74], E141 [75] and collider/fixed target experiments NA64(e) [76], NA48/2 [77].

The sensitivity curves in Fig. 7.2 are the maximum reach for their respective (m_1, m_2) because the incorporation of the detector was only the number of electrons in the FV, and there are no limitations on the primary and secondary interaction distances.

The main observation is that as m_0 increases, the detector sensitivity is reduced significantly. This effect is due primarily to the flux of χ_1 from the galactic center because of the inverse proportionality $F_{\chi_1} \propto 1/m_0^2$. In addition, the difference in detector sensitivity between $m_0 = 1$ GeV and $m_0 = 2$ GeV reduces as the (m_1, m_2) masses increase at the higher m_X mass ranges. At this region of the dark photon parameter space, the primary interaction cross-section $\sigma_{\chi_1 e^- \to \chi_2 e_R^-}$ is impacted by the smaller energy range available for the recoil electron e_R^-, as well the higher mass of m_X.

It is clear from the sensitivity curves for m_0 that the masses with the most coverage potential are $m_0 = 1$ GeV, 2 GeV. Although in this analysis, the (m_1, m_2) mass pairs are not tuned by any procedure apart from a reasonable mass separation seen in literature [33, 34], the impact of increasing the masses is apparent by the $m_0 = 1$ GeV and $m_0 = 2$ GeV reduction in sensitivity at when spanning higher m_X.

This preliminary study shows clear indications that for $m_0 = 1$ GeV, 2 GeV, 5 GeV, 10 GeV, the ICARUS detector has enough detector mass to be sensitive for iBDM interactions to make contributions to the unexplored regions of the dark photon (m_X, ϵ) parameter space. However, since the detector has fixed dimensions, hardware efficiencies and The next section explores the selection criteria, and its application to the sensitivity of the detector.

7.3 Study II: Secondary Interaction

Study I shows how the detector sensitivity trends when varying m_0, concluding that the χ_1 flux $\mathcal{F}_{\chi_1}$ dominates the sensitivity with this aspect. In addition, at large dark photon mass

m_X values, $m_0 = 1$ GeV and $m_0 = 2$ GeV sensitivity approach each other. However, there are differences in the amount of primary events $N_{primary}$, therefore any real selection criteria and detector efficiencies can these sensitivity curves.

While there are many ways of exploring the iBDM model space due to the multi-parameter nature of iBDM, we decided to focus on the maximum reachable space of both the dark sector mass parameters (m_0, m_1, m_2) and the dark photon parameters (m_X, ϵ) for the ICARUS experiment. The procedure for determining these spaces follows the steps below successively:

1. Fix the dark photon parameters set (m_X, ϵ) at the present exclusion limit

$$(m_X, \epsilon)_{\text{limit}} = (12 \text{ MeV}, \ 0.0008)$$

   and identify the optimal (m_0, m_1, m_2) mass sets that maximize the number of expected events at the given $(m_X, \epsilon)_{\text{limit}}$, passing an established selection criteria.

2. Identify the maximum ICARUS coverage in the (m_X, ϵ) parameter space by evaluating the detector performance through the full detector simulation on the optimal mass parameter sets, (m_0, m_1, m_2) determined in Step 1 above, scanning over the dark photon parameter space near the current exclusion limit.

The optimal mass parameter sets that maximize the number of expected events at (m_X, ϵ) have a greater resistance to the effects of the selection criteria, thereby enabling more sensitivity in the unexplored regions.

In the next section, the selection criteria are presented with an analysis of mass parameter sets with just the selection criteria applied to the iBDM event Monte Carlo pre-detector simulation. Optimal mass sets in the (m_0, m_1, m_2) are then chosen in order to perform the full detector simulation to evaluate the filter algorithm used to obtain the real data used for this analysis [61], in addition to the application of the PMT trigger efficiencies to obtain the

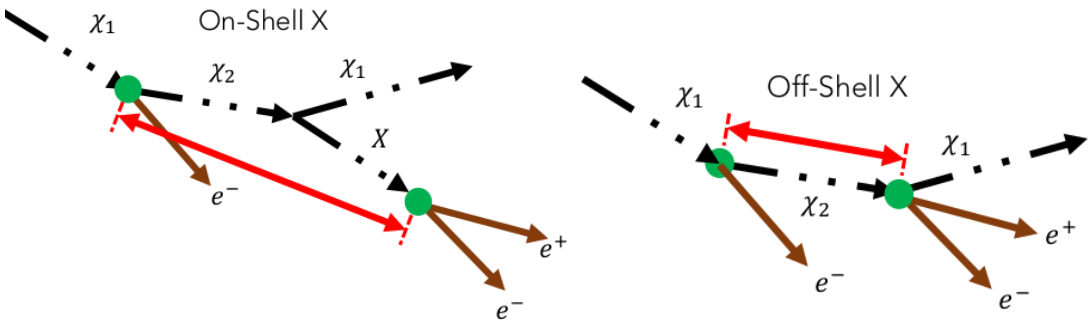

Figure 7.3: A diagram of the topological features of an iBDM primary and secondary interaction. The colors help guide the reader as the selection criteria uses the colors as references for the topological acceptance criteria.

final sensitivity for the ICARUS detector at LNGS for the search of iBDM events that pass selection criteria, filter algothrim, and PMT trigger.

7.3.1 Selection Criteria

An effective set of event selection criteria takes into account (1) the detector constraints and detector efficiencies, along with the event topology that is unique to iBDM and (2) the background that could mimic the signal. An ideal iBDM event would appear as two showers because of the primary interaction recoil electron e_R^- and the secondary interaction e^+e^- pair in or around the center of the detector FV. The iBDM signal was introduced and simulated in Ch. 5, with an example of the iBDM event signal topology in Fig. 5.2. The backgrounds to this type of signal were discussed in Ch. 6, with the potential backgrounds shown to be electromagnetic showers produced by cosmic ray muons and muons from ν_μCC interactions due to delta ray showering, as well as ν_eNC and ν_eCC interactions due to a direct electron shower that can be followed by a photon to e^+e^- conversion.

Due to the PMT collective signal trigger energy limitations, to keep trigger efficiencies at or above $\sim 80\%$(Fig. 4.2), the energy threshold for the events is set to $E_{thres} \geq 200$ MeV [56, 61]. The total energy of the iBDM interaction in the detector then has the following total

energy E_{tot} condition:

$$E_{thres} \leq E_{e_R^-} + E_{e^+e^-} = E_{tot}. \tag{7.7}$$

where $E_{e_R^-}$ is the recoil electron total energy and $E_{e^+e^-}$ is the electron-positron pair total energy. The total energy E_{tot} is the available energy to deposit in the detector; therefore, E_{tot} is an effective metric for preliminary studies to incorporate a minimum trigger cut-off.

In summary, the following selection criteria for iBDM are implemented:(reference Fig. 7.3 for reference to iBDM interaction and color matching)

- FV Containment(Green points): The primary and secondary interaction vertex is contained within the fiducial volume (FV).
- Primary-Secondary Displacement(Red Displacement): The primary and secondary interaction vertex is at least 3cm apart. This aids in the identification of the recoil electron through its minimum ionization particle (m.i.p) properties.
- $E_{thres} \leq E_{depo}$(Brown Arrows):The inequality 7.7 is satisfied for the visible particles.
- Vertex Activity: No hadronic activity, no muons, and no charged particles entering the active volume from the outside are present in the event.

The second requirement can be more explicitly reasoned when considering Fig. 4.1. It is clear that around 15 wires (wire pitch 3mm, hence $\sim$ 45mm travel distance), the electron starts to produce many showers, and the m.i.p identification is lost. This is why a 3cm cut is theoretically imposed. In addition, the last selection criteria impose no activity other than two showers that have an m.i.p signature for the primary interaction and a 2 m.i.p signature for the secondary interaction.

The definition of the selection criteria now enables the application of the first three above (FV containment, 3 cm primary-secondary distance, and $E_{tot} \geq 200$ MeV) in order to understand the selection criteria efficiency ξ_{criteria} for a given mass set at (m_X, ϵ).

7.3.2 Optimal (m_0, m_1, m_2) Mass Sets

The detector sensitivity line in the (m_X, ϵ) parameter space is defined along a set of dark photon parameter points that satisfy the 90% C.L condition, where $N_{primary} \geq 2.3$ for zero observed events and a no background assumption. The graphs in Fig. 7.1 and 7.2 show that the limit of the available (m_X, ϵ) (white space). This point is

$$(m_X, \epsilon)_{\text{limit}} \sim (12\ MeV, 0.0008) \tag{7.8}$$

To explore the unexplored, the minimum requirement is that the ICARUS detector covers this point for a given mass parameter set either by having a point on the sensitivity line or a point in side the region encapsulated by the sensitivity curve that indicates the number of events at the points is more than 2.3. The greater the number of events at (m_X, ϵ), the larger the sensitivity region that is encompassed by the sensitivity curve. This will yeild high-event iBDM parameter sets, incorporating the selection criteria. Therefore, this analysis defines a mass parameter set *accessible* to the ICARUS detector if the 90%C.L condition is satisfied, more explicitly

$$N_{\text{expected}}(m_0, m_1, m_2, (m_X, \epsilon)_{\text{limit}}) \geq 2.3 \tag{7.9}$$

where N_{expected} incorporates the selection criteria efficiency ξ_{criteria}. The BDM model parameter groups must be addressed, fixing the others. The approach here is to address the BDM mass group (m_0, m_1, m_2) at the limit of the space $(m_X, \epsilon)_{\text{limit}}$. In summary,

$$(g_{11}, g_{12}) = (0, 1) \tag{7.10}$$

$$(m_X, \epsilon) = (0.012MeV, 0.0008) \tag{7.11}$$

$$m_0 = [1GeV, 10GeV] \tag{7.12}$$

$$m_1 = [10MeV, 140MeV] \tag{7.13}$$

where I have now also defined the range of values for m_1. This is important to establish as well since the target (e^-) mass is known $m_e = 0.511MeV$ and therefore, the inequality for m_2 can now be brought back to the forefront from chapter 2

$$\sqrt{s} - m_e \geq m_2 \rightarrow \sqrt{m_e^2 + m_1^2 + 2E_1 m_e} - m_e \geq m_2. \tag{7.14}$$

To obtain N_{expected} from a known process cross-section, detector medium and volume, detector efficiencies, and identification efficiencies, the formula looks like

$$N_{\text{expected}} = N_{primary} \times \xi_{GE} \times \xi_{scanning} \geq 2.3 \tag{7.15}$$

$$\xi_{GE} \equiv \xi_{\text{trigger}} \xi_{\text{filter}} \xi_{\text{criteria}} \tag{7.16}$$

where ξ_{GE} is the global efficiency that is equal to the combined effects of:

- $\xi_{scanning}$: efficiency related to the ability of the scanners to identify visually an iBDM event
- ξ_{trigger}: efficiency of the collective ability of the PMTs to trigger an event, which can vary depending on the deposited energy
- ξ_{filter}: efficiency of the shower recognizing algorithm that was part of atmospheric analysis applied to iBDM events
- ξ_{criteria}: selection criteria efficiency that represents the fraction of iBDM Monte Carlo events, pre-detector simulation, satisfying the first three selection criteria.

For study presented in this section, the trigger, filter, and scanning efficiency. The selection criteria efficiency ξ_{criteria} is obtained by simulating thousands of iBDM Monte Carlo events via the iBDM Monte Carlo event generator presented in Ch. 5. A python script incorporting the Monte Carlo event generator with a kinematic analysis logic to determine ξ_{criteria} was designed and is implemented.

With all the prerequisite information in place, the procedure for finding accessible mass parameter sets can be presented:

1. Assuming a fixed m_0 with value $\mathcal{O}(1-10\text{ GeV})$, impose $0.010\text{ GeV} \leq m_1 \leq 0.150\text{ GeV}$ and span with a granularity of $\Delta m_1 = 10$ MeV.

2. Make kinematically allowed [30,64] (m_1, m_2) pairs, with a m_2 granularity of $\Delta m_2 = 1$ MeV.

3. Generate iBDM events and apply selection criteria to events to obtain ξ_{criteria}.

4. Identify all (m_0, m_1, m_2) mass sets that have $N_{\text{expected}} \geq 2.3$ and identify where N_{expected} is maximum in the (m_0, m_1, m_2) space at $(m_X, \epsilon)_{\text{limit}}$ to obtain the optimal mass parameter sets for a given m_0 assuming $\xi_{\text{filter}} = 1$, $\xi_{\text{trigger}} = 1$ and ξ_{scanning}.

Figure 7.4 shows the results of this analysis. Each row contains two plots for $m_0 = 1$ GeV, 2 GeV, 5 GeV, and 10 GeV, as indicated on the plot. The plots on the left column show δm vs m_1, where $\delta m = m_2 - m_1$. The red $(m_1, \delta m)$ points on the plots are inaccessible to ICARUS, in which the expected number of events N_{expected} after all selection criteria are applied is less than 2.3, the limit that fails to satisfy the 90% C.L. limit at the present dark photon exclusion limit, $(m_X, \epsilon)_{\text{limit}}$. All other colored points in these plots are the accessible mass parameter sets to ICARUS in which $N_{\text{expected}} \geq 2.3$, assuming ξ_{trigger}, ξ_{filter} and ξ_{scanning} are all equal to 1. The color scale of the non-red points indicates the value for N_{expected}. The color scale is saturated at 300 on purpose to allow points with a smaller number of N_{expected} can be visible. In other words, all combinations of masses with N_{expected} above 300 on Table 7.1 which lists a few optimal (m_0, m_1, m_2) sets which result in rather large number of N_{expected} are all in yellow on the plots.

The plots on the right column show the total energy E_{tot} of the visible, outgoing particles from the iBDM primary (e_R^-) and secondary (e^-e^+) interactions. The boundary between the orange and blue shaded areas indicates the 200 MeV energy threshold. The plots show that as m_0 increases, the total energy of the visible particles in the detector increases, and the

fraction above the 200 MeV threshold increases. It, however, is clearly seen on the vertical scale of the plots that the number of expected events, N_{expected} passing all other criteria, decreases as m_0 increases. This is due to the fact that the F_{χ_1} is inversely proportional to the m_0 mass squared, therefore, N_{expected} is also scaling as $1/m_0^2$. This is also visible in corresponding plots on the left, where the scale of non-red points decreases as m_0 increases.

Focusing on $m_0 = 1$ GeV and 2 GeV, the exclusion of some combinations can be easily traced to the adopted selection criteria. The m_2 masses in which $\delta m > m_X$ create on-shell dark photons, producing iBDM interactions with prompt χ_2 decay and a subsequent prompt X decay, with the average decay lengths < 1 cm for $(m_X, \epsilon) = (12$ MeV, 0.0008) [**?**]. This condition makes the events fail the 3 cm minimum distance selection criteria between the primary and secondary vertices.

Alternatively, the whole bottom row of red points for small δm has a large fraction of events with χ_2's with long lifetimes, which fail to be selected, since they likely are decaying outside the fiducial volume [64]. Lastly, for a large m_1, a significant fraction of the kinetic energy is used for the m_1 and m_2 masses, and although many events could be above the threshold energy E_{thres}, the number of expected events are too small to satisfy the 90% C.L. ($N_{\text{expected}} < 2.3$).

For $m_0 = 5$ GeV and 10 GeV, the energy threshold affects little the large mass regions of $(m_1, \delta m)$ due to the sufficient energy supplied to χ_1 as is seen in the energy spectrum for the respective m_0 masses. However, both the on-shell dark photon effect ($m_X < \delta m$), which causes the events to fail the 3 cm minimum primary-secondary vertex separation requirement, and for the small δm region, a large fraction of events fail the full event fiducial volume containment requirements create the boundaries to the blue and red points. Thus, these mass points are inaccessible to ICARUS.

The energy distributions in Fig. 7.4 show that increasing m_0 decreases the number of expected events overall, reducing the dark photon parameter space coverage by the ICARUS detector. Conversely, the energy range increases as m_0 increases, enabling more energetic

interactions in the detector. Since only ξ_{criteria} is applied to these events, ξ_{filter} and ξ_{trigger} still need to be considered. For $m_0 = 1$ GeV and $m_0 = 2$ GeV, the number of events per 10 MeV energy bin is significantly higher than $m_0 = 5$ GeV and $m_0 = 10$ GeV. This behavior is mainly attributed to the χ_1 flux and m_0 inverse relationship as in Eq. (2.58).

All in all, both $m_0 = 1$ GeV and $m_0 = 2$ GeV enable the search of iBDM in the unexplored (m_X, ϵ) parameter space, making these masses optimal m_0 values. In addition, Table 7.1 shows which m_2 makes N_{expected} maximum for a given (m_0, m_1) mass pair. The number of events is significantly greater for all (m_1, m_2) mass pairs for $m_0 = 1$ GeV and $m_0 = 2$ GeV. Due to the χ_1 flux factor having an inverse relationship with m_0 [see Eq. (2.58)], the number of events for $m_0 = 5$ GeV and $m_0 = 10$ GeV are significantly less, therefore when the filter and trigger efficiencies are applied, the parameter space span will be significantly reduced.

Given the number of events for both $m_0 = 1$ GeV and $m_0 = 2$ GeV, if there are any performance improvements at the level of the filter algorithm, it is minimal compared to the impact of the selection criteria efficiency ξ_{criteria} due to the lower energies at $m_0 = 1$ GeV. The dark photon mass m_X has a significant impact on the lifetime of χ_2, therefore affecting both the FV vertex containment criteria and 3 cm primary-secondary distance criteria. The $m_0 = 2$ GeV extended energy distribution in the tail enables the primary-secondary vertex separation criterion to be respected by more events every m_X while not allowing an overextension to also respect the FV containment requirement. These observations motivate us to choose $m_0 = 2$ GeV as the reference parameter for this analysis.

7.4 Simulation Study III: Sensitivity in (m_X, ϵ)

The selection criteria efficiency $\xi_{criteria}$ for different mass sets made a significant impact on which (m_1, m_2) mass pair is optimal for each m_0. Using $m_0 = 2$ GeV as the benchmark mass for χ_0, Table 7.1 indicates that the optimal masses for χ_1 and χ_2 for maximum coverage in the (m_X, ϵ) parameter space are (m_1, m_2) = (10 MeV, 19 MeV), (20 MeV, 28 MeV),

m_0 (GeV)	m_1 (MeV)	m_2 (MeV)	N_{expected}
1	10	18	940
1	20	26	720
1	30	36	511
1	50	55	231
2	10	19	313
2	20	28	278
2	30	37	249
2	50	56	182
5	10	20	61
5	20	29	58
5	30	39	55
5	50	58	51

Table 7.1: The list of optimal DM mass parameter sets for which N_{expected} is maximum for $(m_X, \epsilon) = (12 \text{ MeV}, 0.0008)$, the present exclusion limit of the dark photon parameter space. Selection criteria are imposed on events; hence, ξ_{criteria} is applied, whereas trigger, filter, and scanning efficiencies are assumed 100%.

(30 MeV, 37 MeV). In this final simulation study, the ICARUS detector sensitivity at LNGS is evaluated under these mass sets, demonstrating that the detector is sensitive to iBDM interactions with trigger efficiency ξ_{trigger}, filter efficiency ξ_{filter} and the selection criteria efficiency ξ_{criteria} applied to obtain the global efficiency ξ_{GE}.

In the previous section, the selection criteria efficiency ξ_{criteria} is obtained by simulating 5000 events and imposing the selection criteria on each event, and the resulting events divided by the total events give ξ_{criteria}. This methodology was applied to different mass sets at the current limit of dark photon parameter space point $(m_X, \epsilon)_{\text{limit}}$ and the resulting N_{expected} was calculated assuming the filter and trigger efficiencies were 100% at $E_{\text{tot}} \geq 200$ MeV. For this section, we take the opposite approach given we found mass sets that optimize the coverage in the (m_X, ϵ) parameter space. The sample points in the dark photon parameter

space for this study are in the unexplored region around $(m_X, \epsilon)_{\text{limit}}$:

$$\begin{aligned} \epsilon = 4 \times 10^{-4} &\rightarrow m_X = [18 \text{ MeV}, 21 \text{ MeV}] \\ \epsilon = 5 \times 10^{-4} &\rightarrow m_X = [15 \text{ MeV}, 24 \text{ MeV}] \\ \epsilon = 6 \times 10^{-4} &\rightarrow m_X = [14 \text{ MeV}, 27 \text{ MeV}] \end{aligned} \tag{7.17}$$

where the brackets for the m_X parameter indicate an inclusive range. and the arrow from the ϵ value to the range indicates that every m_X in the range is paired with that ϵ parameter value. The iBDM event generator simulates 5000 events for each (m_X, ϵ) in the sample space above for the three optimal mass sets belonging to $m_0 = 2$ GeV. The FV containment and 3 cm primary secondary distance selection criteria are applied to each of the iBDM-generated events, and the resulting events that satisfy these two criteria are saved in a separate file.

The kinematic information of the 5000 iBDM events is converted from HEPevt format [66] to the ArtRoot format [67] to be processed with the ICARUS specific LArsoft code, ICARUScode. Lastly, the iBDM events are processed by the particle transport simulator GEANT4 [68], which propagates the particles in the detector TPC, simulating particle interactions with the LAr, which for the iBDM interaction are the recoil electron from the primary interaction and the electron-positron pair from the secondary interaction. For the particle transport via ICARUScode v09_75_00, the configuration files used were

1. Convert HEPevt.txt File → ArtRoot File: modified_prodtext_standard_icarus.fcl

2. Run Events Through G4 Stage: modified_g4_cosmics_purity_8ms.fcl

The output from the GEANT4 simulation is the ionization charge information for each event and the necessary information for the simulation of the wire signals, thereby enabling the detector response.

The *.root* file output from the GEANT4 is converted to a batch of text files (one text file for each event) for the detector response simulation that uses the original code from the atmospheric neutrino study. The detector response simulation is run through a virtual

machine with a Scientific Linux operating system due to the legacy state of the detector response software. The virtual machine image, along with the software for the detector simulation and the filter algorithm, is used with the permission of the INFN collaborators. The prerequisites for this step of the analysis are the GEANT4 root file and a text file with the event numbers that satisfy the fiducial volume and the primary-secondary distance requirement. These events were ultimately the ones that are evaluated by the filter algothrim since these events satisfy the selection criteria. The true energy was not used because the detector simulation will contain the information about the deposited energy via the GEANT4 ionization charge information. At the final stage of the detector simulation, the filter algorithm is applied, and events that pass the filter are marked and put into a file.

Once the detector simulation stage is completed, a set of ROOT .c programs are executed in order to divide the events into energy bins. The filter efficiency ξ_{filter} is given per energy bin. This information is then copied to a spreadsheet where the detector simulation results are recorded. Along with the filter efficiency per energy bin, the trigger efficiency was also incorporated, therefore all elements for the global efficiency ξ_{GE} were obtained, except the scanning efficiency ξ_{scanning}. Assuming $\xi_{\text{scanning}} = 1$, figure 7.6 shows the ξ_{GE} for the indicated mass parameter sets on the legend.

The global efficiency ξ_{GE} behavior across multiple parameter sets has many nested effects. At low m_X and high ϵ, the containment of the events is more satisfied since the decay rate $\Gamma_{\chi_2} \propto \epsilon^2/m_X^2$. As the graph moves toward high m_X and low ϵ, the same relationship shows that the decay rate reduces, and since we are working with the same 5000 events per file, the statistics are reducing for each energy bin. Therefore, in both of these cases ξ_{criteria} is impacted.

The other effect is energy deposition in the detector. The truth information reveals that as you increase the ϵ while keeping m_X fixed, the energy distribution moves to higher energies. Also, increasing the m_X leads to an increase in deposited energy. Hence, the higher their two parameters become, the better the filter algorithm and trigger are going to perform.

With figure 7.6 and, subsequently, the value for N_{exp}, a preliminary sensitivity plot can now be presented. Applying Poisson statistics at 90% C.L on N_{exp}, and assuming $N_{obs} = 0$. The calculated sensitivity is shown in Fig. 7.7. There are two vertical bars, signaling the two kinematic constraints. The left-most constraint has been discussed during the mass parameter study which is the on-shell dark photon mass, and the right-most constraint imposes that only visible decays qualify (Standard Model particle decays).

The sensitivity plots in Fig. 7.7 show motivation that ICARUS can explore the dark photon parameter space that has not yet been excluded by previous experiments. With the signal simulated and studied and the detector sensitivity evaluated showing great motivation for an iBDM search with the ICARUS detector, the presentation of the data scanning results can now be presented.

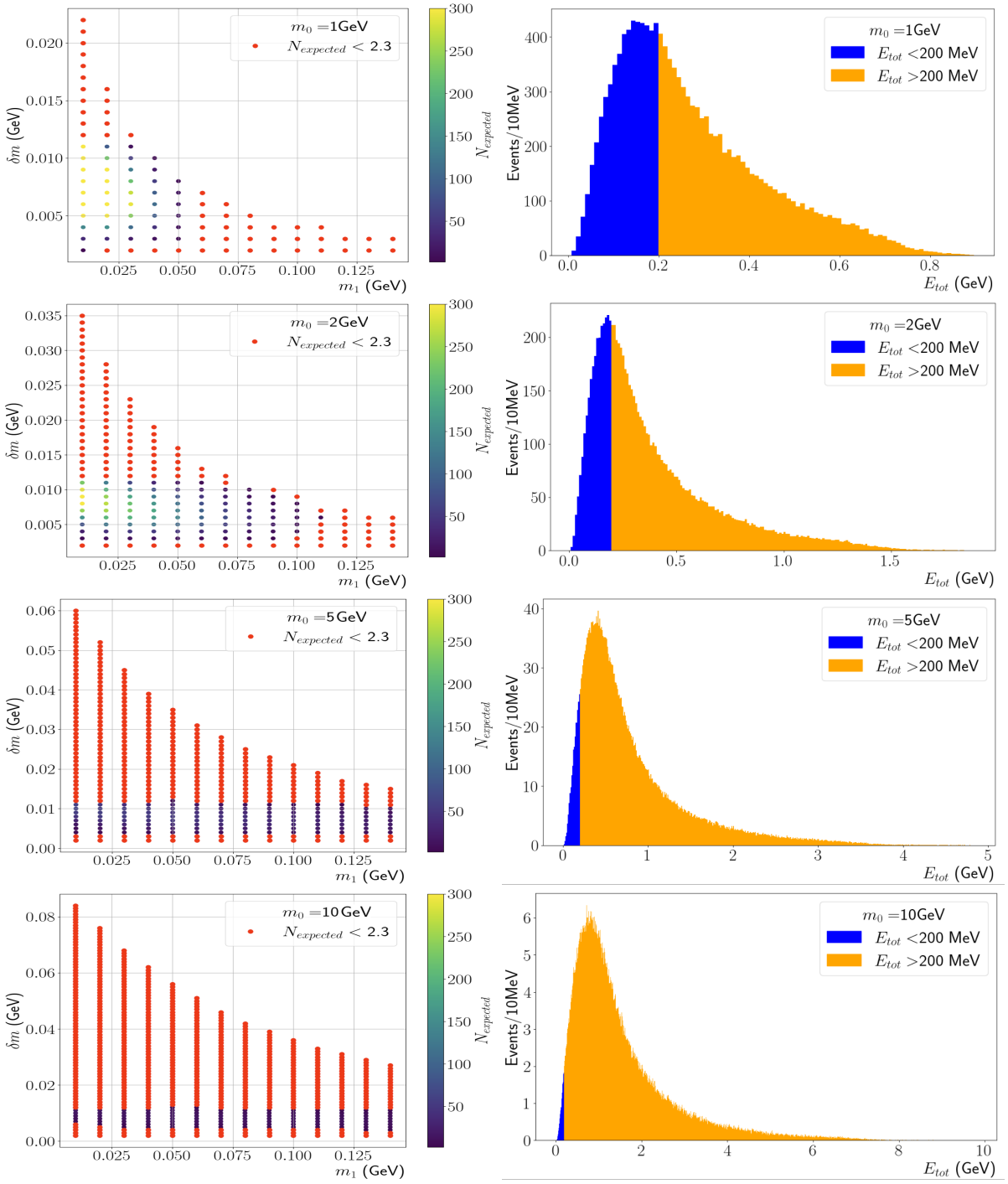

Figure 7.4: The plots on the left are the $(m_1, \delta m)$ mass phase space with red points signifying $N_{\text{expected}} < 2.3$ and colored points signifying $N_{\text{expected}} > 2.3$, where the color grading represents N_{expected}. The N_{expected} value is saturated to 300 to show $(m_1, \delta m)$ points where N_{expected} is maximum. Here, the points in red are categorized as inaccessible under the 90% C.L. assumption with the selection criteria imposed. The color distribution indicates the number of events expected for $t_{\text{exposure}} = 0.3$ year that pass the selection criteria. Recoil electron + electron-positron pair total energy distribution (right) for points $N_{\text{expected}} > 2.3$ (all non-red points) normalized to the total number of expected events for all non-red points $N_{\text{tot}} = \sum_{\text{points}} N_{\text{expected}}$.

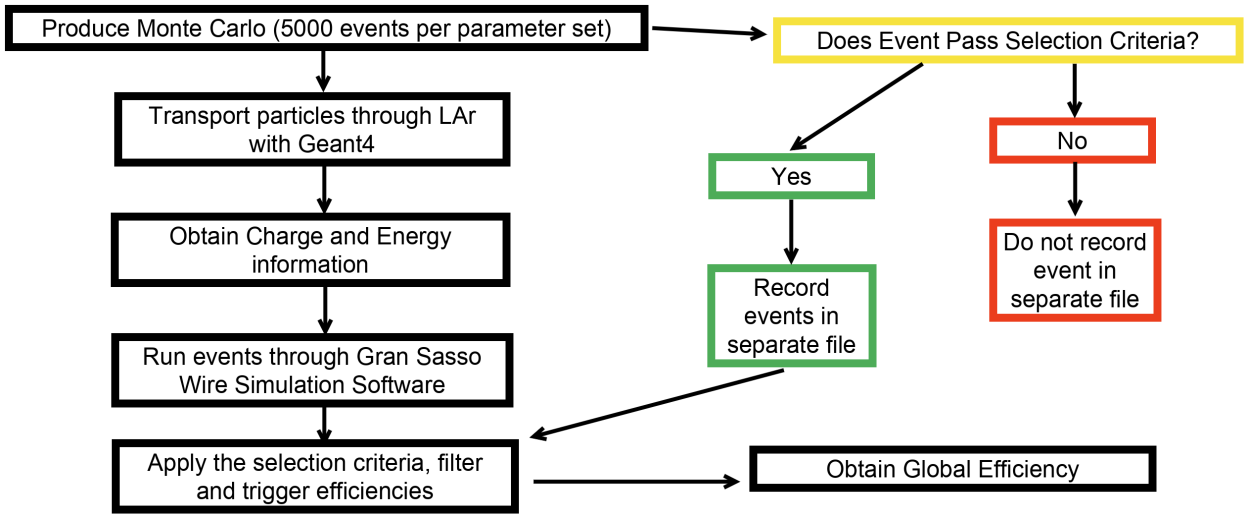

Figure 7.5: The complete flow chart detailing the simulation chain for the detector response to generated iBDM events in the (m_X, ϵ) sample space defined in Eq. 7.17 for the optimal mass parameter sets corresponding to $m_0 = 2$ GeV in Table 7.1. The selection criteria for the simulation chain only apply the FV containment and 3 cm primary-secondary minimum vertex distance as the energy threshold is applied at the filter and trigger stages to decide based on the energy deposition of an iBDM event.

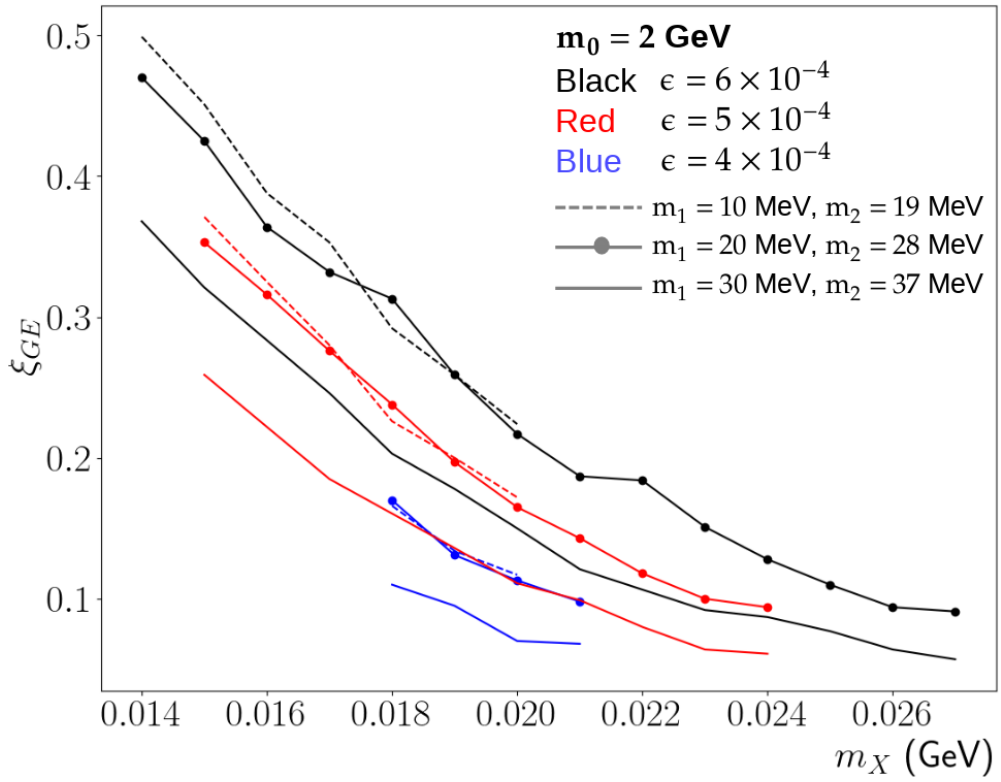

Figure 7.6: This plot shows the global efficiencies ξ_{GE} as a function of the dark photon mass m_X (x-axis), kinetic mixing parameter ϵ (line color), and optimal (m_1, m_2) mass pairs for $m_0 = 2$ GeV (line type).

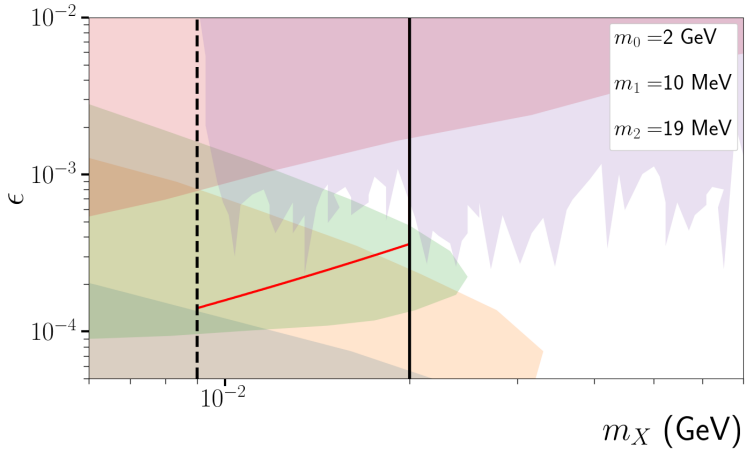

(a)

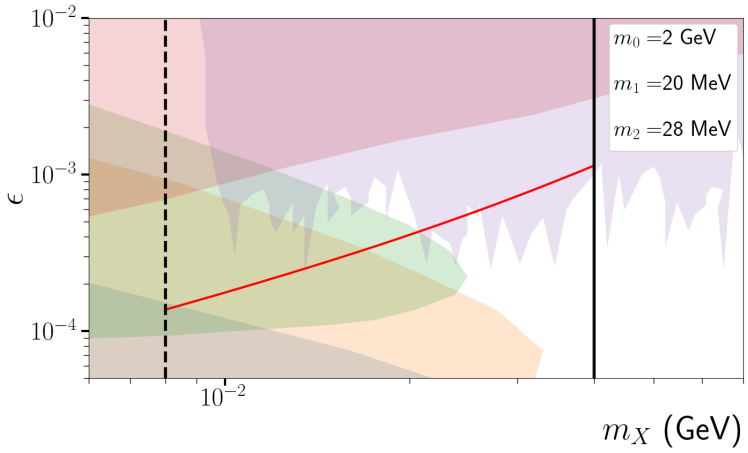

(b)

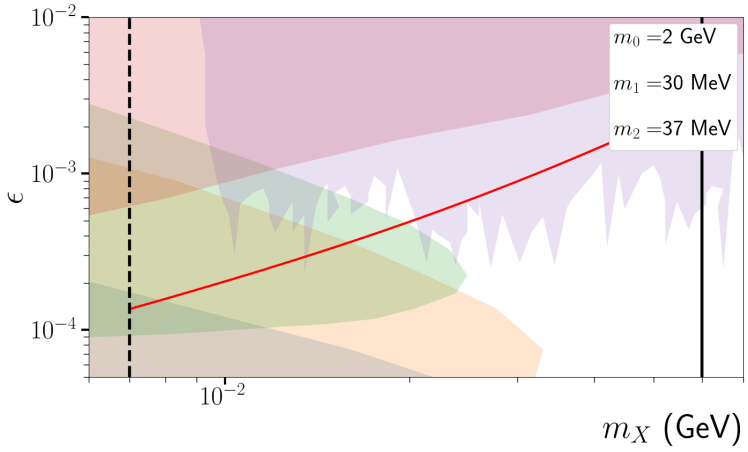

(c)

Figure 7.7: The ICARUS detector sensitivity in the (m_X, ϵ) parameter space for select (m_0, m_1, m_2) mass sets from Table 7.1 incorporating the global efficiency ξ_{GE}. The limit of the sensitivity is indicated by the red 90%C.L boundary and the black dashed and solid kinematic boundaries (on-shell dark photon kinematic limit and visible decay kinematic limit, respectively).

Chapter 8

Data Analysis

The ICARUS dataset used for the search of iBDM is the atmospheric neutrino filtered dataset collected by ICARUS at the Gran Sasso Underground National Laboratory (LNGS) during the detector's 2012-2013 operational run [61]. The data was collected by the application of a cosmic ray (CR) trigger that activated between the CERN neutrinos at Gran Sasso (CNG) beam spills [56, 61]. The CR trigger activates when the PMTs achieve a sum signal from the scintillation light produced when the charged particles traverse the TPC volume through argon de-excitation and recombination [49, 56].

During the trigger readout window of 1 ms, the ionization charge is liberated by the charged particles traversing the TPC volume and is drifted to the anode wire planes, inducing signals on the Induction-1 and Induction-2 planes, after which the charge gets collected on the Collection plane. The wire signals on all the wire planes recorded at the end of the readout window define a full event.

After the recording of the events (the raw unfiltered dataset), the atmospheric neutrino filter algorithm [61] was applied, and the events were flagged for shower activity consistent with ν_eCC interactions [61]. In the simulation analysis presented in Ch. 7, the filter efficiency ξ_{filter} is incorporated in the global efficiency ξ_{GE}, in addition to the evaluation of the selection criteria efficiency $\xi_{criteria}$ and the trigger efficiency $\xi_{trigger}$ for the (m_X, ϵ) sample parameter

space defined in Eq. 7.17, giving the overall analysis and detector performance for the search of iBDM events that are possible for the parameter sets shown in the legend of Fig. 7.6. The analysis of the global efficiency ξ_{GE} leads to the estimation of the ICARUS detector sensitivity in the (m_X, ϵ) for the mass sets $(m_0, m_1, m_2) =$ (2 GeV, 10 MeV, 19 MeV), (2 GeV, 20 MeV, 28 MeV), (2 GeV, 30 MeV, 37 MeV).

The sensitivity analysis shows that regions in the dark photon parameter space that are unexplored by other experiments are explorable under the aforementioned mass sets for an iBDM search in the ICARUS detector by analyzing the filter dataset with the selection criteria defined in Ch. 7. In this chapter, the different stages of the filter data are presented and the classification system is defined with examples of the classification system in action at the end of the chapter.

8.1 Data Visualization and Scanning Stages

The full atmospheric neutrino dataset amounts to a detector exposure of 0.43kton· year [61]. The data for this analysis amounts to a detector exposure of approximately 0.13kton·year. This exposure was the data recoverable by the INFN group at the time of this analysis. The exposure is equivalent to 4134 events, each of which was identified by the filter algorithm. The large number of events warranted the creation of a scanning workforce in order to divide the data for parallel scanning. This also enables cross-checks by re-scanning to ensure the accuracy of the classification.

To view the wire signals of each wire plane as a function of time, the software Qscan is used (see Ch. 5 for more information). Qscan opens the data files and graphs the wire information as a function of time for each wire plane. To perform a search for iBDM with this data, each event is opened in the Qscan visualization program (event display). A scanning workforce was assembled to evaluate each event at the University of Texas at Arlington (UTA) by inspecting the event display of all wire planes and identifying events with showers

that show no signs of association with other interactions in the same event.

The data analysis can be broken down into two main stages: (1) The visual scanning and identification of events with showers that topologically resemble an iBDM interaction and (2) The dE/dx analysis of the final iBDM candidates to confirm 1 m.i.p primary interaction and 2 m.i.p secondary interaction. Stage (1) has three sub-stages in order to perform a conservative search for events with iBDM-like track/shower topologies:

- Preliminary Scan: Scan all 4134 events and identify isolated showers or showers that could be unassociated with muons if present.
- Final Muon Rejection: If a muon track is confirmed to be part of an event flagged with showers that look unassociated with the muon, reject the event
- iBDM Candidate Selection: From the remaining isolate shower events, identify events with clear iBDM-like topologies that have indications of only a primary and secondary interaction.

These sub-stages for the visual scanning ensure that at every decision-making point of the scanning chain, the filtering process to identify isolated iBDM-like shower events is as conservative as possible.

CR muon tracks and electromagnetic showers are not the only types of activity that a scanner can encounter in each event. Given the data used is the filtered dataset for the atmospheric neutrino study, there will be neutrino interactions that induce showers and muon tracks accompanied by nuclear fragmentation. In the next section, a classification is presented to make the data accessible for filtering at the various visual scanning sub-stages.

8.2 Classification System and Training

A triggered event in the TPC has an associated Run and Event identifier. Figures 8.1- 8.3 shows two event displays (Collection (Coll) at the top and Induction-1 (Ind1) at the bottom)

that are the output of the Qscan software and each event display window shows the Run and Event at the top of each window. The Run and event identifiers are the values that are referenced throughout the analysis when classifying the events.

Every Run has its own spreadsheet, where each row represents each event in that Run. There are three columns the represent the Event number, the classification, and a brief description to accompany the classification for clarification or comments about the event. The classification system opted for in this analysis is a number system that spans the possible event cases in the data but also allows for the nuances of each event. In the case where a scanner does not understand the tracks of the event, an "unsure" classification is also integrated. This prompts further investigation from other scanners in order in order to understand the possible underlying process. The classification system needs to be robust when trying to filter for different kinds of events and efficient for scanners to classify as many events as possible. The classification system numbers are defined as:

- **1**: event with only noise from wires
- **2**: event with an identified muon with no isolated showers
- **3**: event with a vertex from which multiple tracks emerge
- **4**: event with an isolated shower
- **5**: event that requires further investigation

Vertex events can be nuclear fragmentation from neutrino ν_eCC and ν_μCC interactions [61] [61]. Vertex interactions are distinguishable from the iBDM interaction due to the additional activity at the vertex of the interaction, apart from an electron track that either stays as a track or subsequently showers for the primary interaction or the electron-positron tracks that subsequently showers for the secondary interaction. Muon events are clear straight tracks that pass through the detector, originate from sections very close to the border of the detector, or originate from a vertex in the detector via ν_μCC interactions.

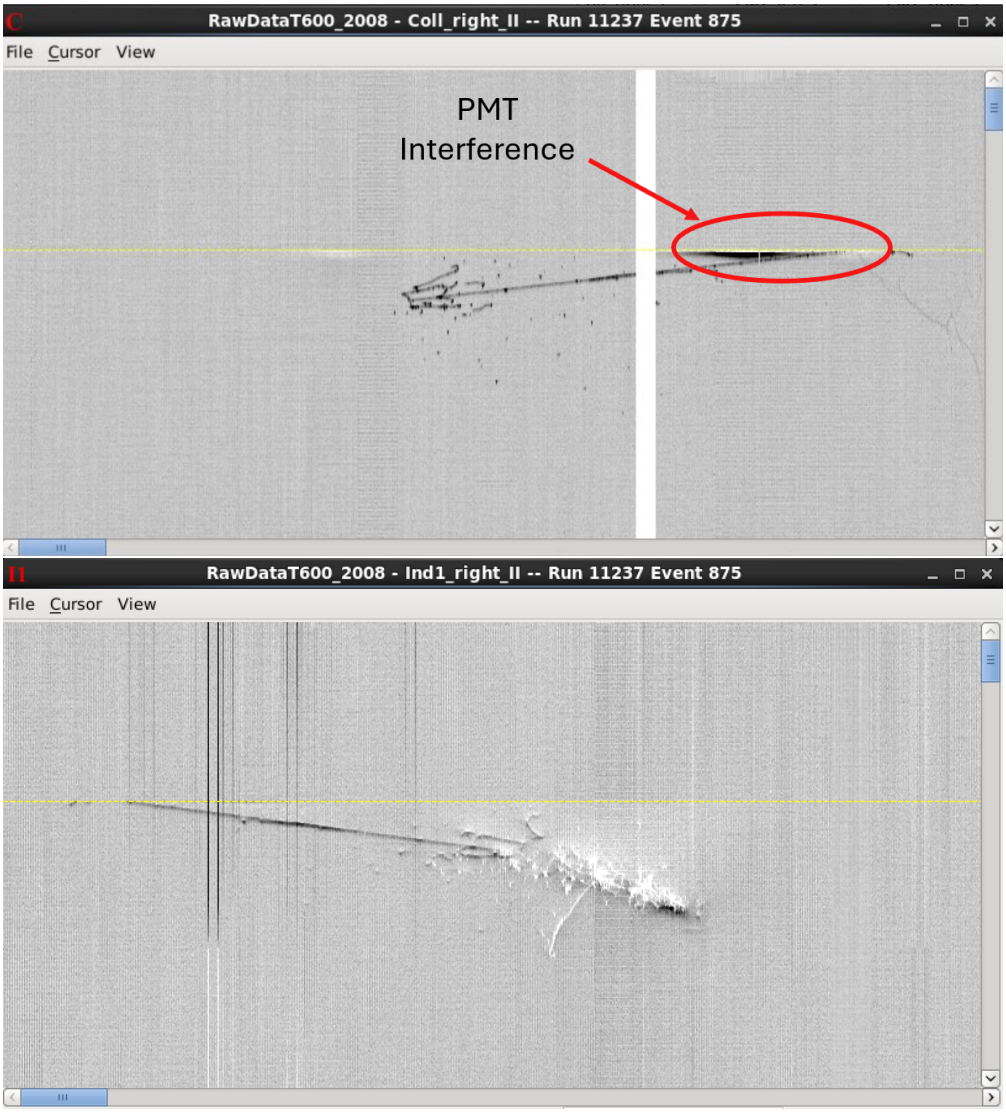

Figure 8.1: Run 11237 Event 875 is a muon event (1 classification). The white-induced tracks visible in the induction 1 view (ind1 window here) indicate that part of the track was happening outside the TPC, behind the wire planes. There is also further evidence of interaction outside the TPC via the PMT interference seen in the collection view (coll window here) as a dark, smeared-out spot.

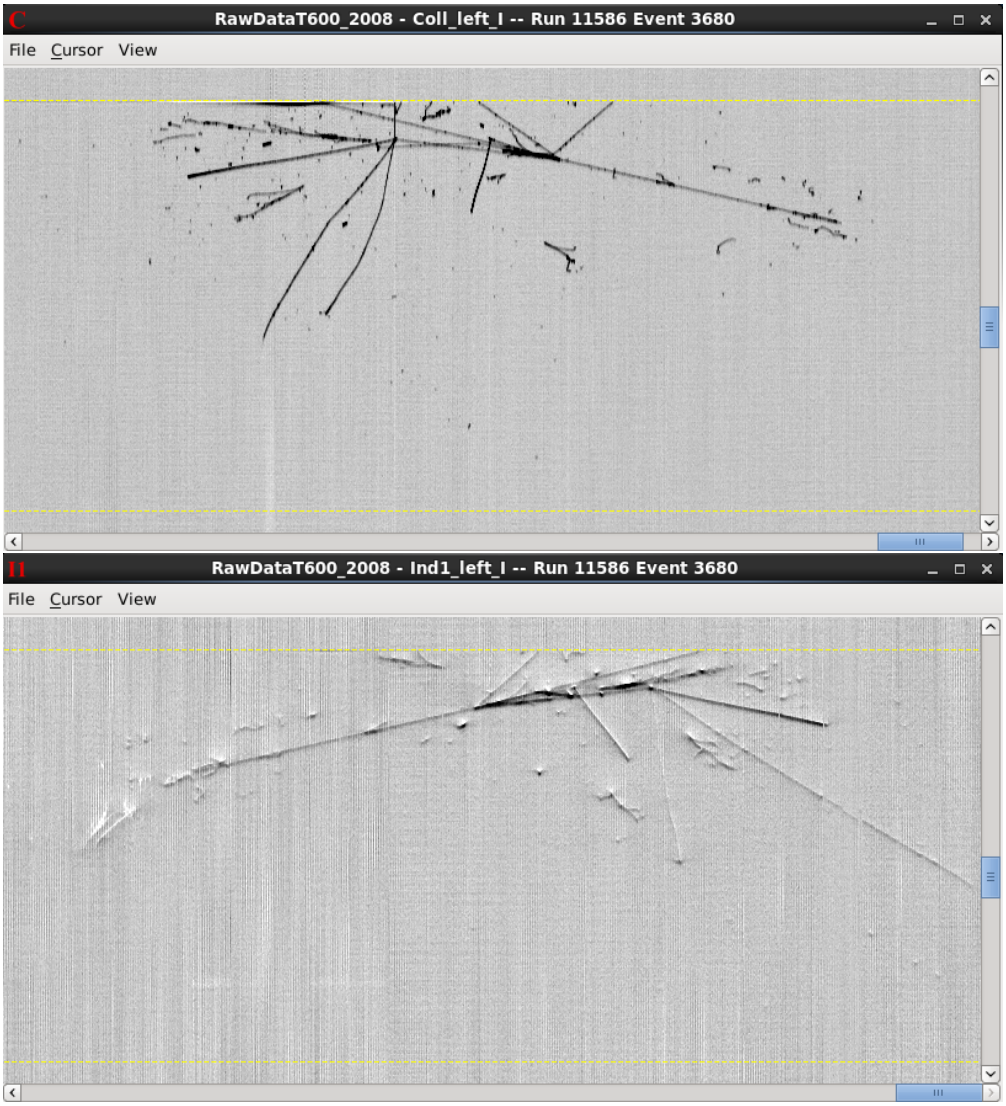

Figure 8.2: Run 11586 Event 3680 is classified as vertex event(3 classification). There is again the PMT interference seen in the collection view (coll window). This event might have been the result of a nuclear interaction.

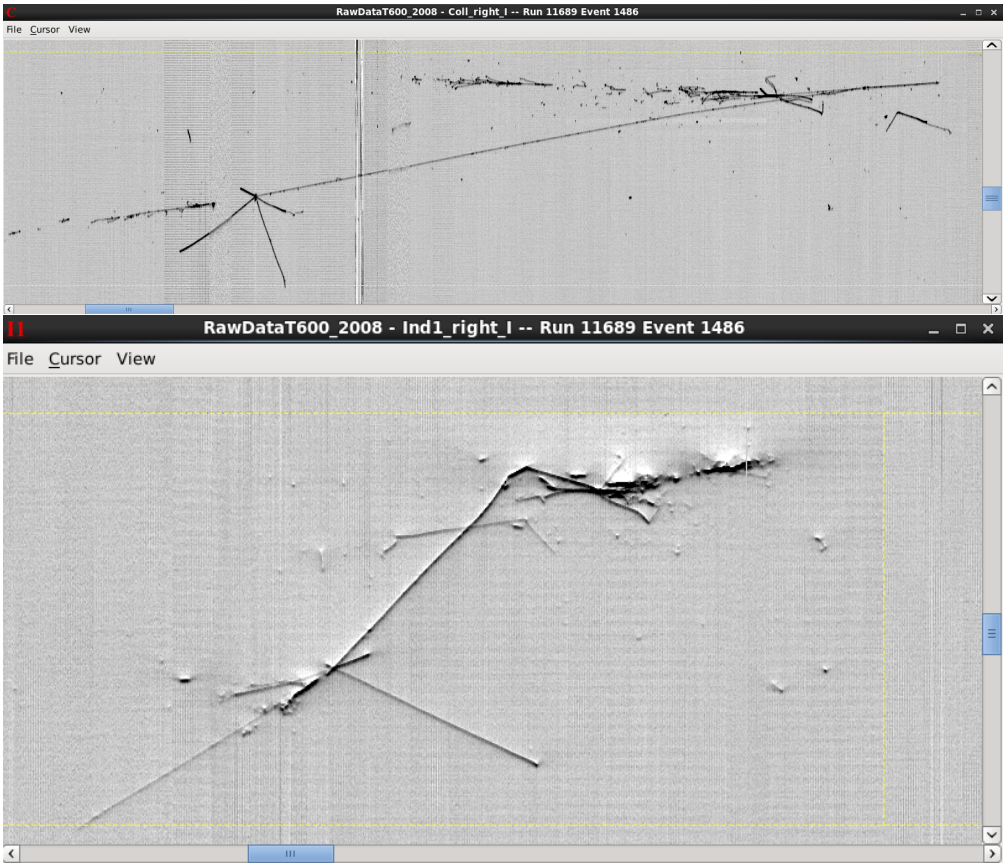

Figure 8.3: Run 11689 Event 1486 is classified as a vertex event(5 classification). From the top image (coll view), two vertices can be identified, with the leftmost vertex showing evidence of a nuclear neutrino interaction, specifically ν_μ due to the clear long straight track in the coll view (top image).

Training sessions were organized for the UTA scanning group in order to educate each member on how the topological features of each track in the event display indicate what type of particle produced the track. This included some examples of iBDM simulated events. The initial training on the Qscan software and classification guidance was performed by INFN collaborator Christian Farnese. As the principal investigator of the atmospheric neutrino study, his experience with the dataset and Qscan software expedited the learning process.

8.3 Classification in Action

Examples of how the classification system was implemented in the data are in Fig.8.1-8.3. Each figure contains event displays of the Collection wire plane view (Coll) and the Induction-1 view (Ind1). Information on whether the track entered the side of the detector can be obtained from Induction 2 view (abbreviated ind2 in the event display), or the collection view (abbreviated coll in the event display) by noting that each of these views have yellow dashed lines that indicate the boundary of the TPC. The induction 1 view (abbreviated ind1 in the event display)event display has an extra yellow line in the middle of the view that indicates the top of the detector due to this wire plane having the wires subtend horizontally. This view gives information on whether the track came from the top or the bottom of the detector.

Figure 8.1 is an example of a muon event with a shower activity originating from behind the wires planes. In the Induction-1 view (Ind1), the white "tracks" indicate reverse polarization for the bipolar signal, therefore, the charges are inducing the signal opposite from the direction of the drift. The muon crosses the cathode plane afterward (top yellow dashed line). The Collection view (Coll) shows signs of PMT interference at the top of the view, also indicating there is activity originating behind the wire planes. This event was classified as a "1" with a description indicating there is shower activity that is not isolated from the muon event.

Figure 8.2 is an example of a vertex event with classification "3". There are clear visual indications that there are two vertices in the Collection view (Coll). There are indications of showers coming from electron-positron pairs as well.

Figure 8.3 shows an example of a vertex event that in fact is also a neutrino event and is identified as ν_μCC interaction because of the long straight track seen in the top event display corresponding to the Collection view.

The signals discussed in this section show a stark contrast to the simulated signal example in Ch. 5, Fig. 5.2. Although vertex events can classify neutrino events, the goal of this study was not to do a re-scan for neutrino events but rather scan for iBDM events with a classification system that leads to clear background and iBDM signal distinction. The identification and classification events shown in Fig. 8.1-8.3 indicate that the classification system is comprehensive.

Chapter 9

Statistical and Systematic Uncertainties

This chapter presents the inherent statistical and systematic uncertainties for the evaluation of the number of expected events N_{expected} for the ICARUS detector sensitivity in the dark photon (m_X, ϵ) parameter space defined in Eq. 7.17. The selection criteria depend on spatial and energy measurements. Ultimately, the selection criteria influence the selection criteria efficiency $\xi_{criteria}$, and therefore $\xi_{criteria}$ is subject to the spatial and energy capabilities of the ICARUS detector. The statistical and systematic uncertainties of filter efficiency ξ_{filter}, trigger efficiency ξ_{trigger}, and the selection criteria efficiency ξ_{criteria} establish the uncertainty of the global efficiency ξ_{GE}, which when combined with scanning efficiency ξ_{scanning} play an integral part in determining the uncertainty in N_{expected} for the sensitivity plots of the three mass parameter sets (m_0, m_1, m_2) = (2 GeV, 10 MeV, 19 MeV), (2 GeV, 20 MeV, 28 MeV), (2 GeV, 30 MeV, 37 MeV) in the (m_X, ϵ) parameter space.

The final set of iBDM candidates that pass the data scanning classification stages and the selection criteria are subject to a wire-by-wire m.i.p classification stage for the primary interaction and a 2 m.i.p classification stage for the secondary interaction. This classification requires measuring the dE/dx at the beginning of each interaction. The wire-by-wire energy

resolution is presented and shown to have a negligible impact on the analysis.

9.1 Global Efficiency ξ_{GE}

The global efficiency is calculated as the number of iBDM events that satisfy the selection criteria, filter algorithm, and trigger divided by the total simulated events for the mass and dark photon parameters under investigation for the energy bins 0 MeV-200 MeV, 200 MeV-400 MeV, 400 MeV-600 MeV, 600 MeV-800 MeV, 800 MeV-1 GeV, and 1 GeV-1.5 GeV. 5,000 events are simulated for each $(m_0, m_1, m_2, m_X, \epsilon)$ and put through the detector simulation chain(Fig 7.5). Once the wire signals are obtained and the total deposited energy is obtained, the events are put into their corresponding bins. Applying the selection criteria, filter algorithm, and trigger efficiency results in the reduction of events seen per energy bin. Events either "passed" or "failed" the selection criteria, filter algothrim, or trigger. This leads to a binomial statistical uncertainty for each of the efficiencies in each bin

$$\delta\xi_{\mathrm{i}} = \sqrt{N_{\mathrm{bin}}\xi_{\mathrm{i}}(1-\xi_{\mathrm{i}})}. \tag{9.1}$$

where ξ_{i} is the efficiency under consideration and N_{bin} is the number of events in the bin before application of the efficiency related to the selection criteria, filter, or trigger. This section presents the range of uncertainties per iBDM parameter set and implements the energy bin with the highest uncertainty as a conservative overall estimate. The systematic uncertainty is calculated by varying the efficiencies per bin by a constant and evaluating the percent change in the number of expected events N_{expected}. The statistical and systematic uncertainties are then added in quadrature to determine the overall uncertainty of each efficiency to determine the 1 σ deviation of the detector sensitivity.

9.1.1 Selection Criteria Efficiency ξ_{criteria}

The selection criteria depend on the spatial and energy resolution. This includes the fiducial volume containment of the primary and secondary interaction vertices, a minimum 3 cm primary and secondary vertex distance requirement, and a 200 MeV total deposited energy threshold. The selection criteria efficiency is the determination of the total events across all energy bins that satisfy the selection criteria. Therefore, the uncertainty in the selection criteria efficiency $\delta\xi_{\text{criteria}}$ depends on the spatial and energy resolution.

The spatial resolution, in this instance, is the physical uncertainty in determining the 3D coordinates of the tracks in the detector. This uncertainty directly impacts the number of potential candidates since the selection criteria require full containment of both sets of electromagnetic showers in an iBDM event within the fiducial volume, defined as 5 cm inward from the boundaries of the active volume, and a minimum 3 cm distance separation between the primary and the associated secondary vertices. The spatial resolution is dependent on the inter-wire spacing for the wire planes. The inter-wire space, also known as wire pitch, is equal to 3 mm [40, 46] for all three wire planes. The same distance is also true for the wire plane spacing, making the spatial resolution $\sim \text{mm}^3$. The fractional uncertainties of the spatial resolution are $\sim 3\%$ to the minimum distance requirement and $\sim 2\%$ to the fiducial volume criterion.

The systematic uncertainty of the selection efficiency that pertains to the fiducial volume and the primary-secondary vertex distance is estimated using the standard technique of varying the cut value for each requirement by ± 1 mm in all directions and taking the fractional differences of the number of expected events that pass between the varied cut values. The resulting percentage uncertainty due to spatial resolution to the fiducial volume containment requirement is estimated to be $< 0.1\%$. On the other hand, the 3 cm minimum distance requirement uncertainty is estimated to be $+2\%$ and -1% due to the exponentially falling spectrum of the distance between the two vertices. We take 2% as the uncertainty

for this requirement to be conservative. The resulting combined percentage systematic uncertainty for selection efficiency, ξ_{criteria} for both fiducial volume and the 3 cm minimum distance requirements, due to the detector spatial resolution is $\pm 2\%$.

The energy resolution for the reconstructed e.m. shower was evaluated to be $\sigma/E(\text{GeV}) = 3\%/\sqrt{E} \bigoplus 1\%$ [58] by the ICARUS collaboration, studying the reconstruction of the π^0 events. This resolution corresponds to a few percent of the typical energy of the events considered for the iBDM interactions (around 1 GeV). The energy resolution directly impacts the present analysis since we implement a 200 MeV minimum energy deposition requirement to which the impact of the energy resolution at this threshold is at the level of 7.7%. The same methodology above is applied to the energy resolution uncertainty estimate, resulting in the percentage uncertainty $\delta N_{\text{expected}}/N_{\text{expected}} \sim 1\%$.

9.1.2 Trigger Efficiency $\xi_{trigger}$

In Ch. 3, the PMT trigger system was presented, and in Ch. 4, the cosmic ray (CR) trigger used to obtain the dataset for the iBDM analysis is presented. Figure 4.2 shows the PMT sum signal efficiency for different parameters that affect the efficiency. The trigger efficiency affects $N_{expected}$ via the parameter $\xi_{trigger}$. The trigger efficiency is energy bin dependent, and this dependence is on full display in Figure 4.2. There are other dependencies, such as distance from the wall where the PMTs are mounted (behind the wire planes) and position along the long Z coordinate (parallel to the wall on which the PMTs are mounted).

The parameter that most affects the trigger efficiency is the energy. The energy threshold established in the selection criteria is $E\text{thres} = 200$ MeV. At and above this threshold, the efficiency remains consistent, averaging 83%. The trigger also needs to be active outside the CNGS beam spill. Chapter 6 discussed the possible backgrounds from the CNGS beam. The "Early Warning" system [56] aids in the identification of time intervals when the next beam spill arrives at the ICARUS detector at LNGS. There are inefficiencies with this system, and therefore, the ability to separate the CNGS trigger and CR trigger contributes to the

Source	Uncertainty
ξ_{criteria}	2.2%
ξ_{filter}	1.9%
ξ_{trigger}	1.5%
ξ_{scanning}	5%
Total Uncertainty	6%

Table 9.1: The total systematic uncertainty from each source of the uncertainties. These values are reflected in the 1σ deviation of the dark photon exclusion limit.

fractional uncertainty of the trigger efficiency.

Incorporating energy effects and trigger separation, the fractional uncertainty of the trigger efficiency determined by the ICARUS collaboration, $\delta\xi_{\text{trigger}}/\xi_{\text{trigger}}$ is estimated to range between 1% and 2%, resulting in 1.5% systematics to this analysis.

9.1.3 Filter Efficiency ξ_{filter}

The filter efficiency ξ_{filter} was evaluated at the detector simulation stage. It is obviously dependent on the iBDM parameter set and the energy bin. The energy bins are constructed to match the energy bins of the trigger efficiency. This way, the filter and trigger efficiency can be combined per energy bin. The percentage uncertainty of the filter efficiency, $\delta\xi_{\text{filter}}/\xi_{\text{filter}}$ is estimated by applying the filter criteria to the detailed signal simulation sample and is found to range 1.7% – 2.3%, depending on the DM model parameter sets. The resulting systematic uncertainty due to the filter efficiency to present analysis is obtained using the same methodology as the above, namely varying the efficiency by the corresponding uncertainty, estimated to range 0.8% – 1.1%. We take 1.1% systematic uncertainty due to the uncertainty of the filter efficiency to be conservative.

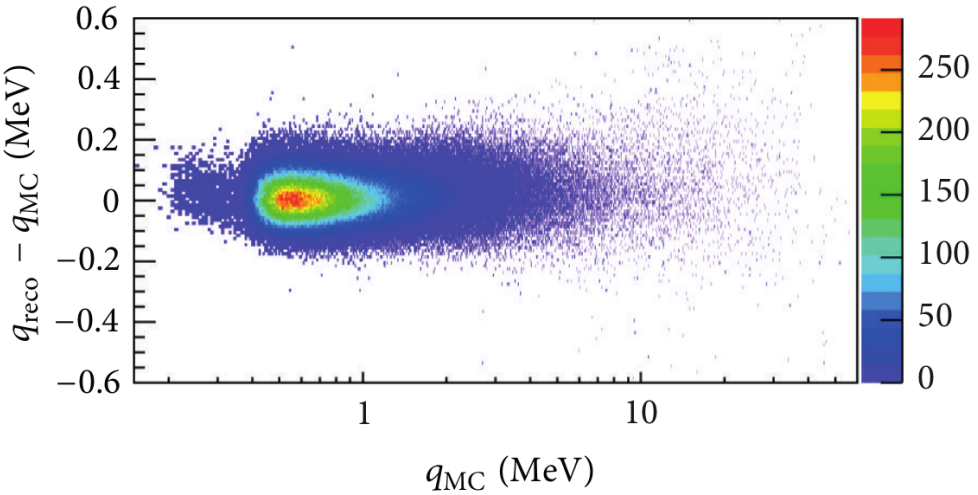

Figure 9.1: This graph is constructed via simulation of events looking at the difference between reconstructed deposited energy (q_{reco}) and the hit information from Monte Carlo (q_{MC}). This graph was produced under the study to understand 3D reconstruction in the ICARUS detector at Gran Sasso [46].

9.2 Scanning Efficiency $\xi_{scanning}$

The scanning efficiency $\xi_{scanning}$ is estimated using a blind set of 294 iBDM events. Each scanner is asked to scan the blind set of iBDM signal samples and categorize the events as described in Ch. 8. The efficiency for the event categorization is found to be consistent between the scanners, resulting in the overall efficiency of $\xi_{\mathrm{scanning}} = 76\% \pm 5\%$, where the uncertainty is estimated by adding the statistical binomial uncertainties of the scanner efficiencies in quadrature to be conservative.

Chapter 10

Results

The analysis of the four iBDM candidates(Fig. 10.1-10.5) consists of determining whether the dE/dx of the track at the beginning of the primary and secondary interaction matches that of a m.i.p and twice a m.i.p, respectively. There are many ICARUS publications [40, 46, 61] that demonstrate how analysis on the dE/dx of a track can be used as a marker for particle identification. A visual cue on the dE/dx of a track is the intensity of the track and is visually measured by how dark a track is.

The first iBDM candidate is in Fig. 10.1. The tracks in this event have topological features that of an iBDM interaction (for reference, see Fig. 5.2). There are clearly two major interactions, which can be labeled as the primary and secondary interactions (see figure for the identification of each). The geometric position of the interactions in this event is at the bottom of the TPC. This fact is shown in the view of Induction 1 (labeled ind1 in the figure at the top of the window). The bottom blue scroll wheel is in the extremum of the view (all the way to the left). The induction 1 view contains information on the vertical position because of the horizontal wire setup for this view. The top of the detector would be indicated by a dashed yellow line in the middle of the view when the blue scroll wheel is at the center position of the view.

The Collection view shows a short primary track and then a secondary track that looks

like a e^-e^+ shower. However, the primary track visually has a high dE/dx. This is not characteristic of an electron track but rather a much more massive particle such as the proton. This is especially noticeable when looking at the e^-e^+ track since the beginning of this track is a 2 m.i.p signature. These statements are quantified in Fig. 10.2, which shows the dE/dx as a function of wires from the primary interaction vertex and a zoomed-in view of the Collection plane event display. The arrows point from the dE/dx measurement data to the segments of the track they represent. Because of the lack of evidence to declare the primary track an electron track, this iBDM candidate is rejected.

The candidate shown in Fig. 10.3, also has topological similarities to an iBDM interaction highlighted by the identification of a primary and secondary interaction. The induction 1 view (ind1 at the top of the window) shows that the tracks are located at the top of the TPC (the yellow line is now visible in the induction 1 view) close to the edge. Because of their proximity to the edge of the detector, there is a chance that these tracks are a product of interactions outside the TPC volume. This is why the fiducial volume selection criteria are in place to filter out these kinds of scenarios. The initial track is too short to adequately acknowledge it as a m.i.p. The track indicated as secondary does have the characteristics of a e^+e^- shower. However, the whole event must match the topology of an iBDM interaction *and* to satisfy the selection criteria. Therefore, this iBDM candidate event is rejected.

The candidate in Fig. 10.4, therefore, the event was classified as an interesting event in the preliminary scanning due to the aforementioned conservative classification system. This is an event in which the e^+e^- tracks are present, but there is no evidence of a primary electron track. This event is indicative of pair production from a photon. With the selection criteria requiring an e^+e^- pair *and* an electron track, it is clear that this event is no longer an iBDM candidate for this analysis.

Lastly, the event in Fig. 10.5 has the closest resemblance to an iBDM interaction across all stages of this search. In the figure, the primary and secondary interactions are indicated. The event is also very much inside the TPC volume. In both the collection and induction 2 view,

it is clear that each interaction is a fair distance away from the top and bottom yellow dashed lines, which indicate the cathode and wire plane sides of the TPC. In induction 1, the top of the detector is indicated by a vertical yellow line in the middle of the view. This position is when the blue scroll wheel is moved to the middle of the view (see Fig. 10.4). Therefore, the probability of the interaction as a consequence of outside activity is suppressed. The secondary track is identified as a e^+e^- pair(short track). However, the primary track has some uncertainty. The dE/dx of the beginning of the track can resemble a 1 or 2 m.i.p signal. This means that the interaction could be a photon that the first pair produces, and showering ensues, creating another pair down (the misidentified secondary interaction). The analysis, therefore, does not have the certainty to claim this iBDM candidate to be identified as an iBDM interaction. Thus, this event is rejected.

The justified rejection of the four iBDM candidates due to the selection criteria and dE/dx analysis represents a null result, and therefore, the number of observed events is zero. This analysis, therefore, sets exclusion limits in the dark photon (m_X, ϵ) for the mass sets (m_0, m_1, m_2) = (2 GeV, 10 MeV, 19 MeV), (2 GeV, 20 MeV, 28 MeV), (2 GeV, 30 MeV, 37 MeV), which are shown in Fig. 10.6. The 90%C.L limit is represented by the solid red line, which includes the selection criteria, filter, and trigger efficiencies. The red dashed lines represent the 1σ from the total uncertainty calculated using Table 9.1, which includes the uncertainties of all the aforementioned efficiencies. The black lines represent the kinematic constraints, with the solid black line indicating the dark photon mass of invisible decays such as $X \rightarrow \overline{\chi}\chi$ is possible ($m_X \geq 2m_1$), and the black dashed line indicating the dark photon mass that enables on-shell dark photon production ($m_X \leq m_2 - m_1$). This analysis and Fig. 10.6 show that through the search of iBDM in the ICARUS detector at LNGS, a significant portion of the unexplored (white regions) of the dark photon parameter space for each (m_0, m_1, m_2) mass set indicated in the legend of each exclusion plot has been excluded, setting a new benchmark for future iBDM searches.

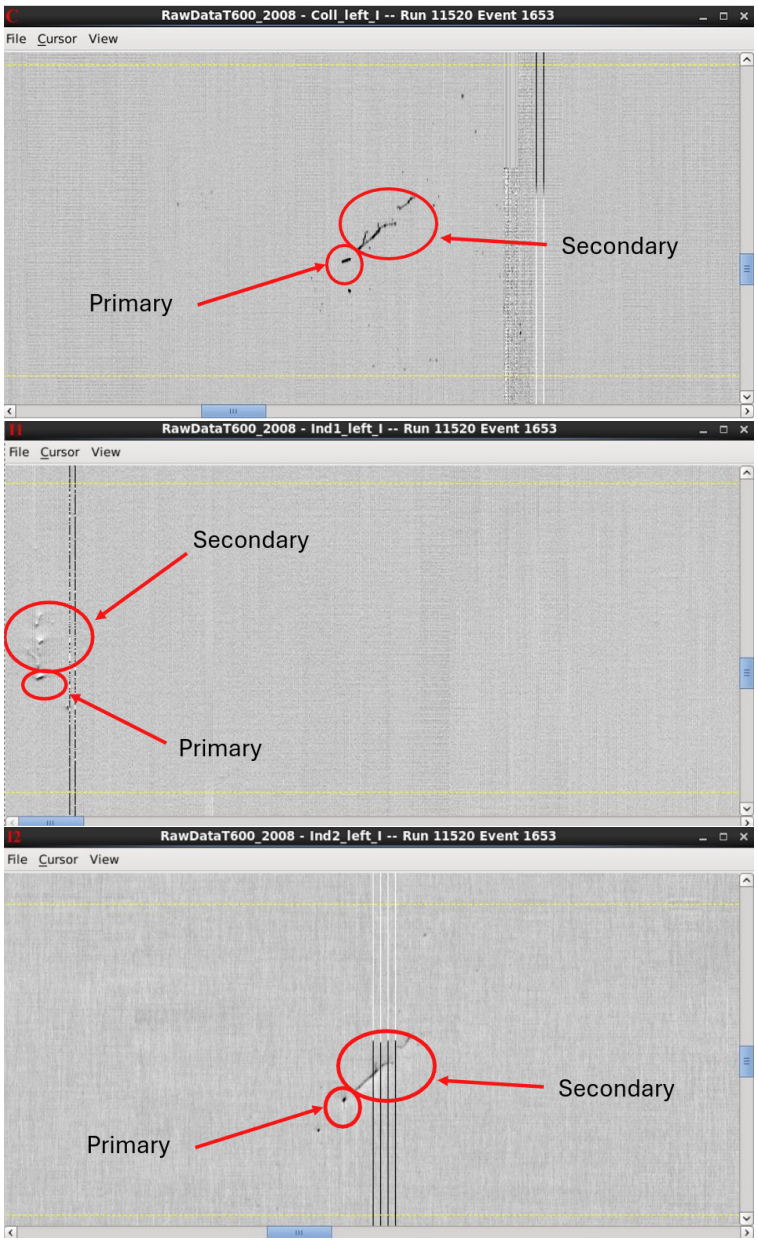

Figure 10.1: This iBDM candidate (Run 11520 event 1653) has very similar topology to an iBDM event. In the Ind2 view, there are two charge depositions before a showering track. If compared to iBDM, this section should be a recoil electron. However, the track is short and does not exhibit behavior that matches dE/dx of m.i.p. In fact, this track resembles a proton (see Fig. 10.2). For this reason, the event was rejected.

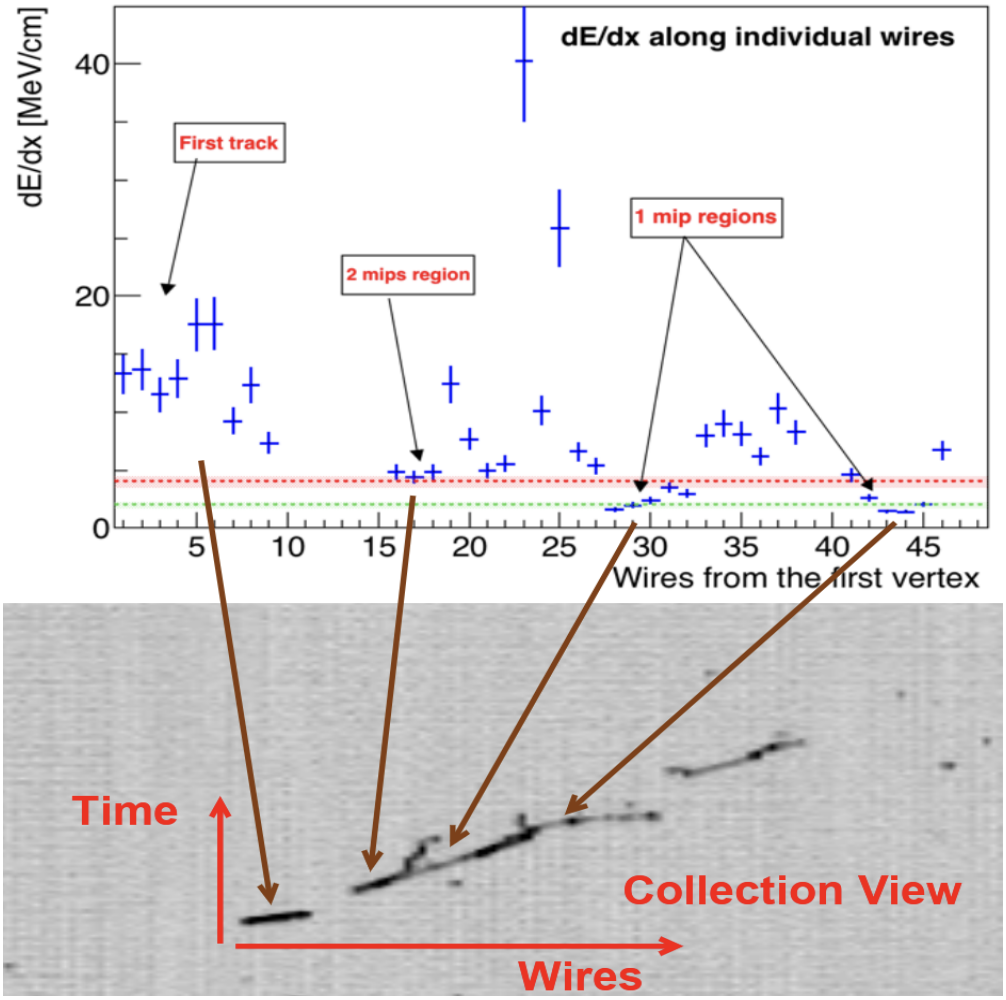

Figure 10.2: A zoomed-in Collection view of the iBDM candidate corresponding to Fig. 10.1 (bottom) and the corresponding dE/dx energy deposit as a function of wires (top). The dimension of the event display image represents 40 cm (H)$\times$ 50 cm (V) region of the detector. The brown arrows visually guide the wire numbers to the corresponding regions in the event display. The time and wire information is the same as referenced in Fig. 6.2. Based on the shower development pattern in the event display, the direction of the particle motion is from left to right. Topologically, two main interactions are recognizable in the event, with the left-most track resembling a primary interaction followed by the secondary one.

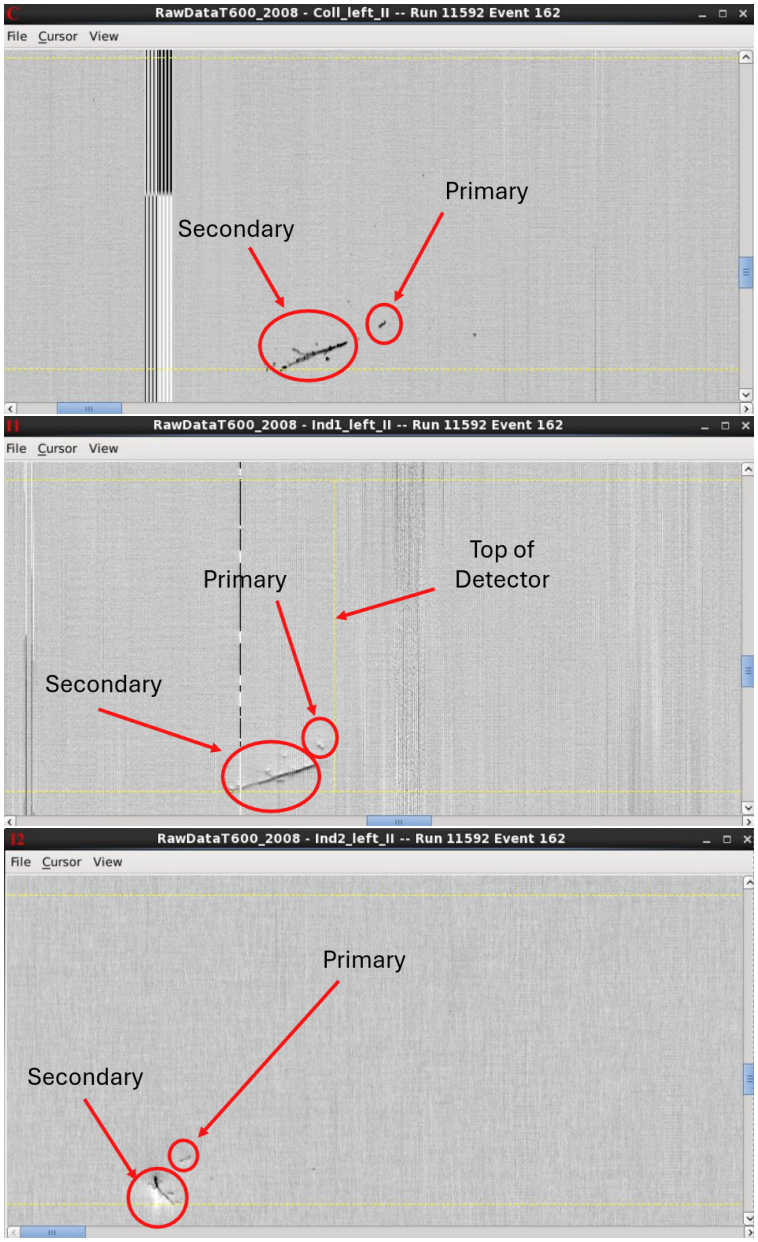

Figure 10.3: This iBDM candidate (Run 11592 event 162) when looking at all the views has a very similar topology is iBDM. Upon closer inspection of the middle view (ind1) it is apparent that the event is not fully contained. This is in addition to the fact that the event is partially outside the FV (5cm from the yellow vertical line). For these reasons, the event was rejected.

Figure 10.4: This iBDM candidate(Run 11654 event 2777) upon closer inspection only contains one part of the iBDM topology (e^+e^-). This event could have been produced by a stray gamma ray. For this reason, the event was rejected.

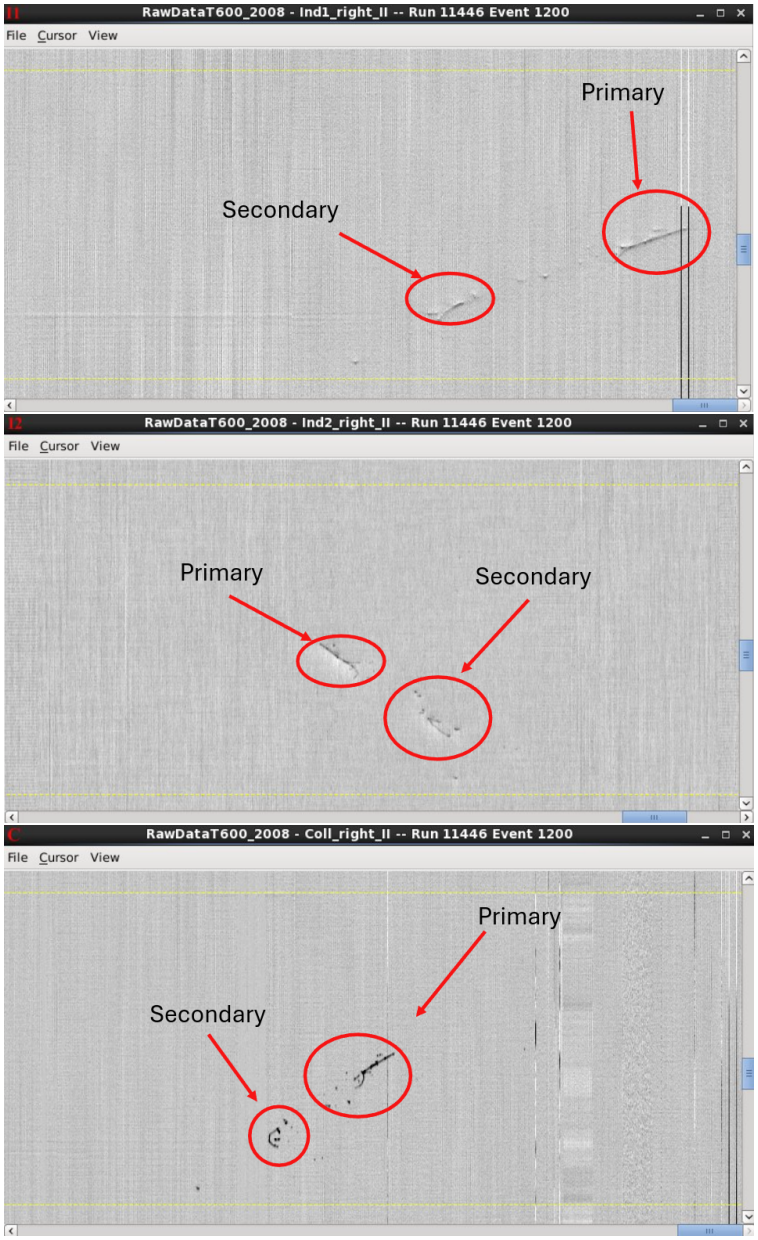

Figure 10.5: This iBDM candidate (Run 11446 event 1200) was the closest iBDM match topologically. A study was conducted to figure out the dE/dx at the beginning of the associated primary track (rightmost track in coll view) and unfortunately the m.i.p signal was not realized. For this reason, the event was rejected.

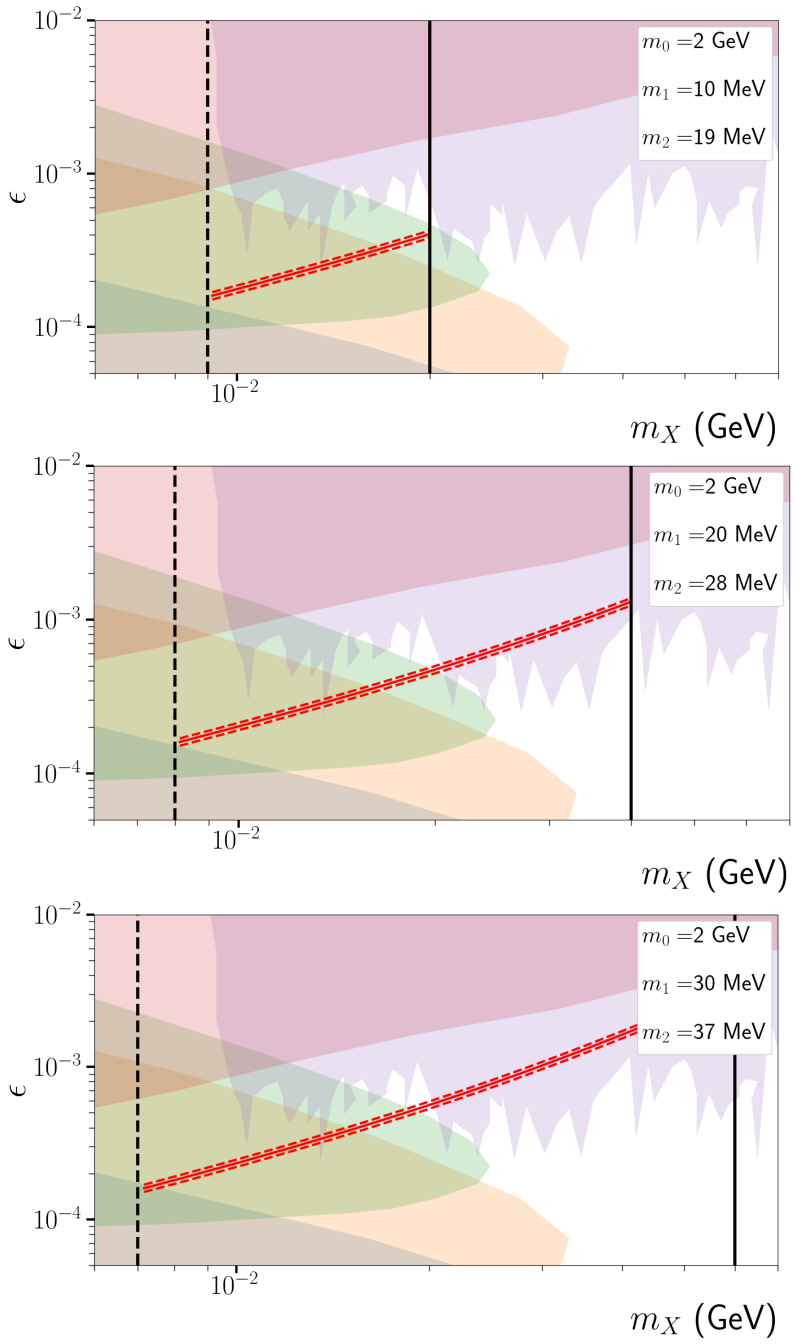

Figure 10.6: The 90% C.L. exclusion limit in the (m_X, ϵ) parameter space, on log scale, for the three optimal mass parameter sets where $m_0 = 2$ GeV and $(m_1, m_2) = (10$ MeV,19 MeV), (20 MeV, 28 MeV), and (30 MeV, 37 MeV), top to bottom, respectively. The excluded regions of other experiments have been obtained from Ref. [32], specifically consisting of beam dump experiments (e.g., nu-Cal [74], E141 [75])and collider/fixed target experiments (e.g., NA64(e) [76], NA48/2 [77]). The solid red line on each plot represents the exclusion limit based on the central value, while the dashed red lines reflect the overall uncertainties shown in Table 9.1. The black lines show the kinematic limits on which the final states are either unobservable - solid line - or fail the minimum distance and the fiducial volume containment requirements.

Chapter 11

Conclusions and Beyond

This dissertation presents a search for inelastic boosted dark matter (iBDM) in the ICARUS detector during the 2012-2013 operational period in the Gran Sasso Underground Laboratory. The dataset was a subset of the atmospheric neutrino filter dataset that contained events that were flagged due to the identification of electromagnetic shower activity.

An extensive simulation analysis is presented to find the accessible iBDM parameter sets. From this search, an *optimal* DM mass list was identified given the various selection criteria that reflect topological and kinematical constraints.

The mass set list in Table 7.1 only outlines the mass parameter sets that maximize the number of expected events $N_{expected}$ given the selection criteria presented in Ch. 7 at the limit of the dark photon unexplored (m_X, ϵ) parameter space. Focusing on optimal mass parameter sets (m_0, m_1, m_2)=(2 GeV, 10 MeV, 19 MeV), (2 GeV, 20 MeV, 28 MeV), and (2 GeV, 30 MeV, 37 MeV), a full detector simulation is performed with the available Gran Sasso software for wire simulation, alongside current ICARUS at Fermilab software for LAr-DM interactions via GEANT4 in ICARUScode. The detector simulation focuses on a sample space close to the limit of the dark photon (m_X, ϵ) parameter space defined by Eq. 7.17.

The detector performance is evaluated and is measured by global efficiency ξ_{GE}, which includes the selection criteria efficiency, the filter algothrim efficiency, and the trigger efficiency.

The detector sensitivity (Fig. 7.7 proved that the filtered dataset collected by ICARUS at LNGS was sensitive enough to probe regions of the (m_X, ϵ) parameter space unexplored by other experiments. With a total detector exposure of 0.13 kton·year, translating to 4,134 triggered events, four events with the iBDM topology passed the various scanning stages. After the application of the selection criteria and a dE/dx analysis, all candidates are rejected and therefore no events were observed.

All in all, the complete analysis of this dissertation sets new exclusion limits for the (m_0, m_1, m_2)=(2 GeV, 10 MeV, 19 MeV), (2 GeV, 20 MeV, 28 MeV), and (2 GeV, 30 MeV, 37 MeV) mass parameter sets in the dark photon (m_X, ϵ) as seen in Fig. 10.6. These results not only improve on past experiments but are the first of their kind in the ICARUS collaboration, marking an optimistic beginning for the search for many others beyond Standard Model physics models with the ICARUS detector.

Several improvements can be made to this study, including improving the scanning efficiency and a more streamlined procedure for the dE/dx analysis of interesting events. The data analyzed here was only 1/3 of the full dataset used for the atmospheric neutrino study. This means ICARUS at Gran Sasso might have more to say than a null result for the remaining detector exposure. Even if the result is still null, a multiple of three can greatly improve the new exclusion limits. Applying the improvements for training the scanners, a more streamlined analysis chain, and increased exposure will give us more insight into whether DM exists in the form of BDM or establish new parameter space targets for future experiments.

Bibliography

[1] A. Einstein. On the Foundations of the Generalized Theory of Relativity and the Theory of Gravitation. *Phys. Z.*, 15:176–180, 1914.

[2] S. Carroll. *Spacetime and Geometry: An Introduction to General Relativity*. Pearson Education, NJ, USA, 2013.

[3] S. Weinberg. *Lectures in Quantum Mechanics, 2nd Edition*. Cambridge University Press, 2015.

[4] Y. B. Zel'dovich and I. D. Novikov. *Stars and Relativity*. Dover Publications, 2011.

[5] R. C. Tolman. *Relativity, Thermodynamics and Cosmology*. Dover Publications, 2011.

[6] F. Zwicky. On the Masses of Nebulae and of Clusters of Nebulae. *The Astrophysical Journal*, 86:217, October 1937.

[7] S. Profumo. *An Introduction to Particle Dark Matter*. World Scientific, London, 2017.

[8] G. D'Olivo and M. Socolovsky. Poincaré gauge invariance of general relativity and einstein-cartan theory, 2011.

[9] D. Baumann. *Cosmology*. Cambridge University Press, Cambridge, 2022.

[10] Y. Yoon *et al.* New method to revisit the gravitational lensing analysis of the bullet cluster using radio waves. *Journal of Cosmology and Astroparticle Physics*, 2023(09):044, sep 2023.

[11] D. Clowe *et al.*. A direct empirical proof of the existence of dark matter. *Astrophys. J. Lett.*, 648:L109–L113, 2006.

[12] M. Markevitch *el al.*. Direct constraints on the dark matter self-interaction cross section from the merging galaxy cluster 1e 0657–56. *The Astrophysical Journal*, 606(2):819, may 2004.

[13] K. G. Begeman *et al.* Extended rotation curves of spiral galaxies: dark haloes and modified dynamics. *Monthly Notices of the Royal Astronomical Society*, 249(3):523–537, 04 1991.

[14] S. Navas *et al.* Review of particle physics. *Phys. Rev. D*, 110:030001, Aug 2024.

[15] C. L. Bennett *et al.*. Nine-year wilkinson microwave anisotropy probe (wmap) observations: Final maps and results. *The Astrophysical Journal Supplement Series*, 208(2):20, sep 2013.

[16] O. Lahav and A. R. Liddle. The cosmological parameters 2014, 2014.

[17] Evan Grohs and George M. Fuller. Big bang nucleosynthesis, 2023.

[18] L. Wyrzykowski *et al.*. The OGLE view of microlensing towards the Magellanic Clouds – IV. OGLE-III SMC data and final conclusions on MACHOs*. *Monthly Notices of the Royal Astronomical Society*, 416(4):2949–2961, 09 2011.

[19] D. P. Bennett. Large magellanic cloud microlensing optical depth with imperfect event selection. *The Astrophysical Journal*, 633(2):906, nov 2005.

[20] C. Alcock *el al.* The macho project: Microlensing results from 5.7 years of large magellanic cloud observations. *The Astrophysical Journal*, 542(1):281, oct 2000.

[21] H. Ruegg and M. Ruiz-Altaba. The stueckelberg field. *International Journal of Modern Physics A*, 19(20):3265–3347, 2004.

[22] D. Scott. The cosmic neutrino background, 2024.

[23] Signe Riemer-Sørensen, David Parkinson, and Tamara M. Davis. Combining planck data with large-scale structure information gives a strong neutrino mass constraint. *Phys. Rev. D*, 89:103505, May 2014.

[24] J. Billard *et al.* Direct detection of dark matter—appec committee report*. *Reports on Progress in Physics*, 85(5):056201, April 2022.

[25] P. A. Amaudruz *et al.*. Design and construction of the deap-3600 dark matter detector. *Astroparticle Physics*, 108:1–23, 2019.

[26] C. E. Aalseth *et al.*. Design and construction of a new detector to measure ultra-low radioactive-isotope contamination of argon. *Journal of Instrumentation*, 15(02):P02024, feb 2020.

[27] D. S. Akerib *et al.*. The lux-zeplin (lz) experiment. *Nuclear Instruments and Methods in Physics Research Section A: Accelerators, Spectrometers, Detectors and Associated Equipment*, 953:163047, 2020.

[28] E. Aprile *et al.* First dark matter search with nuclear recoils from the xenonnt experiment. *Phys. Rev. Lett.*, 131:041003, Jul 2023.

[29] R. Bernabei *et al.* Results from the dama/libra experiment. *Journal of Physics: Conference Series*, 203(1):012003, jan 2010.

[30] K. Agashe *et al.* (in)direct detection of boosted dark matter. *Journal of Cosmology and Astroparticle Physics*, 2014(10):062, oct 2014.

[31] Geneviève Bélanger and Jong-Chul Park. Assisted freeze-out. *Journal of Cosmology and Astroparticle Physics*, 2012(03):038, mar 2012.

[32] M. *et al.* Fabbrichesi. *The Physics of the Dark Photon: A Primer*. Springer International Publishing, 2021.

[33] G. F. Giudice *et al.* Inelastic Boosted Dark Matter at Direct Detection Experiments. *Phys. Lett. B*, 780:543–552, 2018.

[34] A. Chatterjee *et al.* Searching for boosted dark matter at protodune. *Phys. Rev. D*, 98:075027, Oct 2018.

[35] C. Ha *et al.* First direct search for inelastic boosted dark matter with cosine-100. *Phys. Rev. Lett.*, 122:131802, Apr 2019.

[36] G. Adhikari *et al.* Search for boosted dark matter in cosine-100. *Phys. Rev. Lett.*, 131:201802, Nov 2023.

[37] M. L. Graesser *et al.* Detecting boosted dark photons with gaseous detectors. *Phys. Rev. D*, 109:095015, May 2024.

[38] D. R. Nygren. The Time Projection Chamber: A New 4 pi Detector for Charged Particles. *eConf*, C740805:58, 1974.

[39] Carlo Rubbia. The liquid-argon time projection chamber: a new concept for neutrino detectors. Technical report, CERN, Geneva, 1977.

[40] S. Amerio *et al.*. Design, construction and tests of the icarus t600 detector. *Nuclear Instruments and Methods in Physics Research Section A: Accelerators, Spectrometers, Detectors and Associated Equipment*, 527(3):329–410, 2004.

[41] J. Dawson on behalf of the DUNE collaboration. Status of protodune dual phase. *Journal of Physics: Conference Series*, 1312(1):012004, sep 2019.

[42] B. Abi *et al.* Deep underground neutrino experiment (dune), far detector technical design report, volume i: Introduction to dune, 2020.

[43] P. Benetti *el al.*. A three-ton liquid argon time projection chamber. *Nuclear Instruments and Methods in Physics Research Section A: Accelerators, Spectrometers, Detectors and Associated Equipment*, 332(3):395–412, 1993.

[44] The ICARUS Collaboration. The ICARUS 50 l LAr TPC in the CERN Nu Beam. *arXiv e-prints*, pages hep–ex/9812006, December 1998.

[45] F Arneodo on behalf of the ICARUS collaboration. Operation of a 10 m3 icarus detector module. *Nuclear Instruments and Methods in Physics Research Section A: Accelerators, Spectrometers, Detectors and Associated Equipment*, 461(1):286–289, 2001. 8th Pisa Meeting on Advanced Detectors.

[46] M. Antonello *et al.*. Precise 3d track reconstruction algorithm for the icarus t600 liquid argon time projection chamber detector. *Advances in High Energy Physics*, 2013:1–16, 2013.

[47] Summary of liquid argon properities, Year Published. Accessed November, 2024.

[48] Z. Beever, D. Caratelli, A. Fava, F. Pietropaolo, F. Stocker, and J. Zettlemoyer. Translate - a monte carlo simulation of electron transport in liquid argon. *Computer Physics Communications*, 297:109056, 2024.

[49] P. Cennini *et al.*. Detection of scintillation light in coincidence with ionizing tracks in a liquid argon time projection chamber. *Nuclear Instruments and Methods in Physics Research Section A: Accelerators, Spectrometers, Detectors and Associated Equipment*, 432(2):240–248, 1999.

[50] J. Rico. *First study of the stopping Muon sample with the ICARUS T600 detector*. PhD thesis, Ph. D. Dissertation, ETH 14906, 2002. Available at: http://neutrino. ethz . . . , 2002.

[51] R. Agrawal, D.W. Woodward, and T.F. Yee. Argon production from air distillation: Use of a heat pump in a ternary distillation with a side rectifier. *Gas Separation Purification*, 8(1):37–43, 1994.

[52] M. Antonello *et al.* Experimental observation of an extremely high electron lifetime with the icarus-t600 lar-tpc. *Journal of Instrumentation*, 9(12):P12006, dec 2014.

[53] H. Bethe. Zur Theorie des Durchgangs schneller Korpuskularstrahlen durch Materie. *Annalen der Physik*, 397(3):325–400, January 1930.

[54] M. S. Livingston and H. A. Bethe. Nuclear physics c. nuclear dynamics, experimental. *Rev. Mod. Phys.*, 9:245–390, Jul 1937.

[55] E. Segreto. Properties of liquid argon scintillation light emission. *Phys. Rev. D*, 103:043001, Feb 2021.

[56] M Antonello *et al.*. The trigger system of the icarus experiment for the cngs beam. *Journal of Instrumentation*, 9(08):P08003, aug 2014.

[57] N. Canci. The icarus t600 detector at lngs underground laboratory. *Physics Procedia*, 37:1257–1265, 2012. Proceedings of the 2nd International Conference on Technology and Instrumentation in Particle Physics (TIPP 2011).

[58] C. Rubbia *et al.* Underground operation of the icarus t600 lar-tpc: first results. *Journal of Instrumentation*, 6(07):P07011, jul 2011.

[59] S. Amoruso *et al.* Analysis of the liquid argon purity in the icarus t600 tpc. *Nuclear Instruments and Methods in Physics Research Section A: Accelerators, Spectrometers, Detectors and Associated Equipment*, 516(1):68–79, 2004.

[60] E. Bellotti. The gran sasso underground laboratory. *Nuclear Instruments and Methods in Physics Research Section A: Accelerators, Spectrometers, Detectors and Associated Equipment*, 264(1):1–4, 1988.

[61] C. Farnese. Atmospheric neutrino search in the icarus t600 detector. *Universe*, 5(1), 2019.

[62] M. Meddahi *et al.* Cern neutrinos to gran sasso (cngs): results from commissioning. In *2007 IEEE Particle Accelerator Conference (PAC)*, pages 692–694, 2007.

[63] S. Cecchini and M. Spurio. Atmospheric muons: experimental aspects. *Geoscientific Instrumentation, Methods and Data Systems*, 1(2):185–196, 2012.

[64] A. D. Roeck *et al.* Probing energetic light dark matter with multi-particle tracks signatures at dune. *Journal of High Energy Physics*, 2020(11), November 2020.

[65] R. Brun and F. Rademakers. Root — an object oriented data analysis framework. *Nuclear Instruments and Methods in Physics Research Section A: Accelerators, Spectrometers, Detectors and Associated Equipment*, 389(1):81–86, 1997. New Computing Techniques in Physics Research V.

[66] MarleyUserGuide. Hepevt output interpretation, 2024.

[67] E. D. Church. Larsoft: A software package for liquid argon time projection drift chambers, 2014.

[68] S. Agostinelli *et al.*. Geant4—a simulation toolkit. *Nuclear Instruments and Methods in Physics Research Section A: Accelerators, Spectrometers, Detectors and Associated Equipment*, 506(3):250–303, 2003.

[69] P. K.F. Grieder. Chapter 4 - cosmic rays underground, underwater and under ice. In Peter K.F. Grieder, editor, *Cosmic Rays at Earth*, pages 459–668. Elsevier, Amsterdam, 2001.

[70] F. Arneodo*et. al.* Determination of through-going tracks' direction by means of -rays in the icarus liquid argon time projection chamber. *Nuclear Instruments and Methods in Physics Research Section A: Accelerators, Spectrometers, Detectors and Associated Equipment*, 449(1):42–47, 2000.

[71] MicroBooNe Collaboration. Selection and kinematic properties of muon-neutrino charged-current inclusive events in 5×10^{19} pot of microboone data -public note-, 2016.

[72] M. Ambrosio *et al.*. The macro detector at gran sasso. *Nuclear Instruments and Methods in Physics Research Section A: Accelerators, Spectrometers, Detectors and Associated Equipment*, 486(3):663–707, 2002.

[73] E. D. Nobile. *The Theory of Direct Dark Matter Detection*. Springer Cham, 2022.

[74] J. Blümlein and J. Brunner. New exclusion limits for dark gauge forces from beam-dump data. *Physics Letters B*, 701(2):155–159, 2011.

[75] E. Riordan *et al.* Search for short-lived axions in an electron-beam-dump experiment. *Phys. Rev. Lett.*, 59:755–758, Aug 1987.

[76] D. Banerjee *et al.* Dark matter search in missing energy events with na64. *Phys. Rev. Lett.*, 123:121801, Sep 2019.

[77] J. R. Batley *et al.* Search for the dark photon in π^0 decays. *Physics Letters B*, 746:178–185, 2015.

[78] The DUNE Collaboration. Design, construction and operation of the protodune-sp liquid argon tpc. *Journal of Instrumentation*, 17(01):P01005, jan 2022.

[79] Y. Abraham *et al.* 16(07):P07017, jul 2021.

Appendix A

Hardware Work I: ProtoDUNE Dual Phase

The Prototype Deep Underground Neutrino Experiment (ProtoDUNE) is an experiment that tests a set of LArTPCs that implement two types of LArTPC charge readout technologies: a single-phase readout system and a dual-phase readout system. The ProtoDUNE detectors are the result of an R&D effort for the construction of the DUNE experiment [42] far detector. DUNE is the next-generation long neutrino baseline experiment from Fermilab in Batavia, Illinois, to the Sanford Underground Research Laboratory in Lead, South Dakota. This amounts to a Baseline span of 1,300 km. The far detector will be installed and operated in Sanford and will consist of four modules, each 10kton LArTPCs, possibly a combination of different charge readout technologies like single phase and dual phase readout technologies.

ProtoDUNE single phase (ProtoDUNE-SP) [78] is very similar in design to the ICARUS detector. The single-phase charge readout system is in the LAr, and the ionization charge drifts horizontally, collected all within the LAr, just like the ICARUS detector. The detector has a total active volume of $7.2 \times 6.0 \times 7.0\ m^3$. The sensing planes are multiple modules, each called anode plane assembly (APAs), which use three wire planes as sensing planes. There are three APAs per TPC, and there are two TPCs. Scintillation light is also used for

the trigger system, with the light-sensitive sensors being silicon photomultipliers (SiPMs) instead of PMTs. The drift HV system uses the cathode-field cage-wire plane system with the cathode biased at -180kV.

ProtoDUNE dual phase (ProtoDUNE-DP) [41] flips the TPC to have a vertical drift direction, having the cathode toward the bottom of the detector and the sensing planes at the top. The dual-phase descriptor indicates that the ionization charge drifts to the surface of the LAr extracted out of the LAr via a biased grid and drifts into a gaseous argon (GAr) layer. The ionization electrons are then multiplied via large electron multipliers (LEMs) that result in a cascade effect in the GAr phase. In principle, this allows for better calorimetric reconstruction by amplifying the signal [41]. The sensing planes are different for ProtoDUNE-DP, with the wires replaced by etched PCB boards with two independent readout views instead of three. PMTs are coated with TPB and some PMTs have a circular piece of polyethylene naphthalate (PEN) [79] attached just above the surface of the PMT.

In 2019, I participated in the installation, commissioning, and operation of the ProtoDUNE-DP detector. My activities included

- **The installation of the various connections between the HV extender and the field cage**: The HV extender was necessary to feed the HV from the top of the detector via an HV feedthrough to the bottom of the detector where the cathode plane was suspended horizontally for a vertical drift. The end product can be seen in Fig.. I was trained to operate a lift in the vertical direction so I could access the higher sections of the extender. The connections were constructed and installed myself. Once all components were installed, I worked on drift HV data extraction and graphing.

- **Investigation into the short of the drift HV system**: I worked with collaborators to identify points of failure in the drift HV system, as well as the calculation as to what steps in the field cage could a short be possible. This was done by revisiting photos after the installation of drift HV parts and using the fact that the drift HV was connected step by step via not only resistor chains but also varistors that break down under some

voltage across. This enabled the identification of which section along the HV extender was the problem/short.

- **Shaping and Installing PolyEthylene Naphthalate (PEN) to PMTs**: ProtoDUNE-DP used a combination of PMTs coated with TPB on the surface and PMTs with PEN attached via mounts just above the surface of the PMTs. I aided in the preparation by shaping and puncturing holes for the installation of the PEN done by the PMT experts.

- **Investigation into bubble formation in the field cage electrodes and Extender** I worked with various collaborators to understand why bubbles were forming. The evidence was the repeated bubble emerging at the surface of the LAr on top of the field cage electrodes and just above the beginning of the field cage extender.

- **Run Coordinator**: I was assigned as run coordinator for a week. The conditions required for a data run were indicated and I coordinated with the various system experts to realize the conditions necessary to obtain the correct data.

- **Testing and Installation of the Camera and Lighting system for the Cryostat**: The camera and lighting system was designed to have a full internal cryostat view during commissioning (LAr filling and testing of components) and operation (physics data collection). I made sure the LED lights could withstand the temperatures of LAr and that the soldering was correctly applied to the end terminals. The cameras were placed in a vacuum-sealed container, and other collaborators ensured their functionality in and out of LAr. Once the cameras were verified to withstand being submerged in LAr and

Apart from these activities, many other tasks were introduced, and I would assist in any way I could, such as the construction of level meters, installing temperature sensors, organizing wires, co-leading in the final cleaning of the cryostat before the closure of the manhole, and

installing electrical and gas lines necessary at the top of the detector. This went on until the start of COVID-19 at the beginning of 2020.

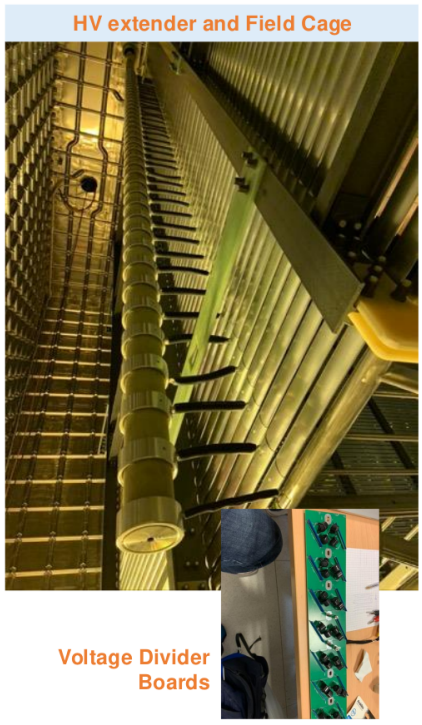

(a)

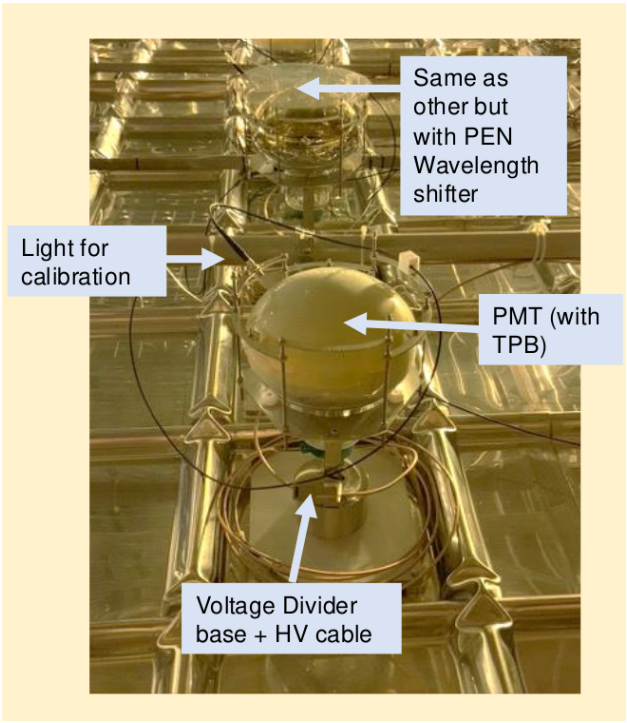

(b)

(c)

Figure A.1: Various pictures were taken during my time working at CERN on ProtoDUNE-DP. (a) is a bottom-up shot of the drift HV extender and its various connections to the field cage. I was responsible for preparing the connections and installing them. (b) are the two types of PMTs, with each type indicated on the picture. (c) is a photo of me and my colleague preparing the PEN for installation.

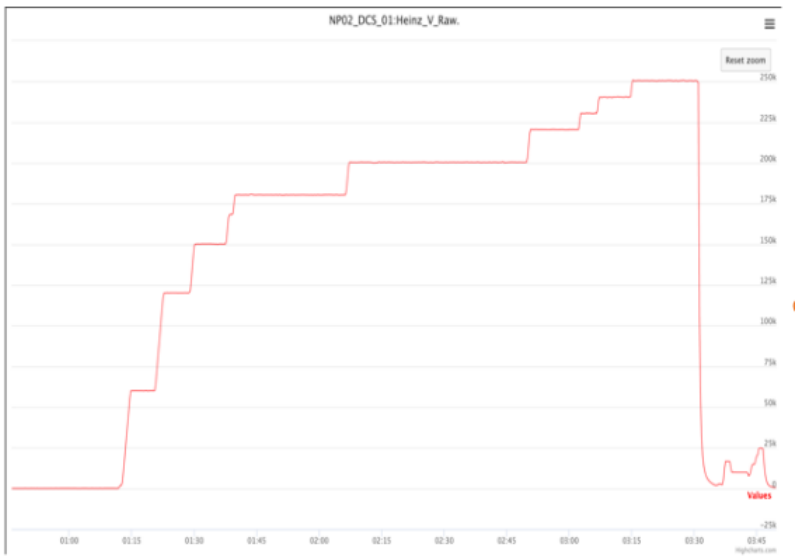

(a)

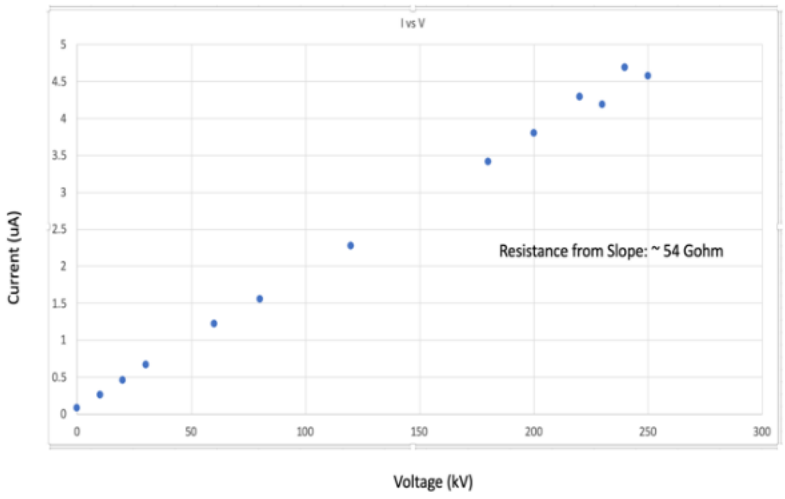

(b)

Figure A.2: The time-lapse of PDDP drift HV ramp up during commissioning (a) and the corresponding current vs voltage graph with the equivalent resistance indicated by the slope (b). At the end of the time-lapse, the HVPS trip can be seen by the sudden drop in voltage. The system instability can be seen in the current vs voltage plot (right) close to 200kV due to the irregular trend of the last few points.

Appendix B

Hardware Work II: ICARUS at Fermilab

Although I was not part of the operation of ICARUS at Gran Sasso, I was part of the commissioning of the ICARUS Detector at the Fermi National Accelerator Laboratory (Fermilab) starting at the end summer of 2020. The detector was repurposed for use in the Short Baseline Neutrino (SBN) program and was named the far detector. I was responsible for the successful installation, commissioning, and operation of the drift HV system. This includes testing the various components in the drift HV racks, including the HVPS (main and spare), the uninterruptible power supply (UPS), the monitoring programs, and the monitor chassis that housed the components, which allowed communication between the drift HV frontend desktop to the power supply. This last component was possible via the use of an ethernet data acquisition system (EDAS).

Starting in winter 2020, I became the lead drift HV expert of the ICARUS detector at Fermilab. There were various main components, all located in Racks, that had to be inspected, commissioned, and maintained during my three-year stay at Fermilab

- **Procuring and Testing of a Spare EDAS**: The EDAS used for the drift HV system was dated, and therefore, obtaining a spare was quite difficult. After obtaining a spare

EDAS, the previous drift HV lead and I constructed a work plan document to install and test the spare EDAS. The test was successful and was used for test bench activities.

- **Creation of EPICs database python scripts**: The EPICs database for ICARUS contains the various variables for the multitude of detector parameters that must be monitored. The monitoring program for the drift HV was outdated; therefore, a script had to be designed to extract the drift HV parameters (current, voltage, voltage divider readings, UPS status) and communicate to the EPICs database the value and timestamp to make sure the values are up-to-date. This script was designed by me, and improved as needed by myself and another drift HV expert.

- **Emergency ramp down procedure and script**: The drift HV system had a UPS that would go into battery mode when the external power (Fermilab power grid) would be interrupted during an unscheduled power outage. I took part in the planning, creation, and testing of the various components needed to implement a complete emergency ramp-down sequence for the drift HV systems. For the software since the software that monitored and controlled the drift HV was outdated, an external script had to be created in order for communication between the UPS and the drift HV monitoring software to take place. The script would poll the UPS via the network card webpage or ssh protocol. There exists a file that essentially contains a bit (0 or 1). If the script determined the UPS was still getting external power, the file would contain a 0. If the script determined that the UPS was using battery power for a duration of 30 seconds, the script would turn the file bit to 1. The drift HV control and monitoring software would read this file and act accordingly.

- **Monitor chassis grounding issue**: The monitor chassis houses the EDAS. If there is a problem with this unit, readback, and HVPS controlling issues would take place. I noted that the drift HV readback values were varying more than usual ($\geq$300V). With the help of several electrical experts in the group, a grounding issue was identified and

fixed. The variation in the readback values was back to normal ($\leq$75V).

- **Identification of a possible short at the field cage**: After the commissioning of the system, there was a moment where the drift HV current increased by $\sim 3\mu$A, with a corresponding increase in the voltage divider reading for one of the TPCs. The increase in both of these values corresponded roughly to the same increase if there was a short between two field cage electrodes, forgoing a chain of four 100MΩ resistors in parallel. There was also evidence from the TPC calibration group of E-field distortions at the edge of the TPC that saw a rise in the voltage divider reading. I communicated with the calibration group the details of the drift HV system for one of their members to model the system in COMSOL, a modeling software, and understand the effect of a field cage short toward the wire planes of the detector. At the end of 2023, the drift HV current value went back to the commissioning values, and the calibration group also saw evidence that the E-field distortions disappeared.

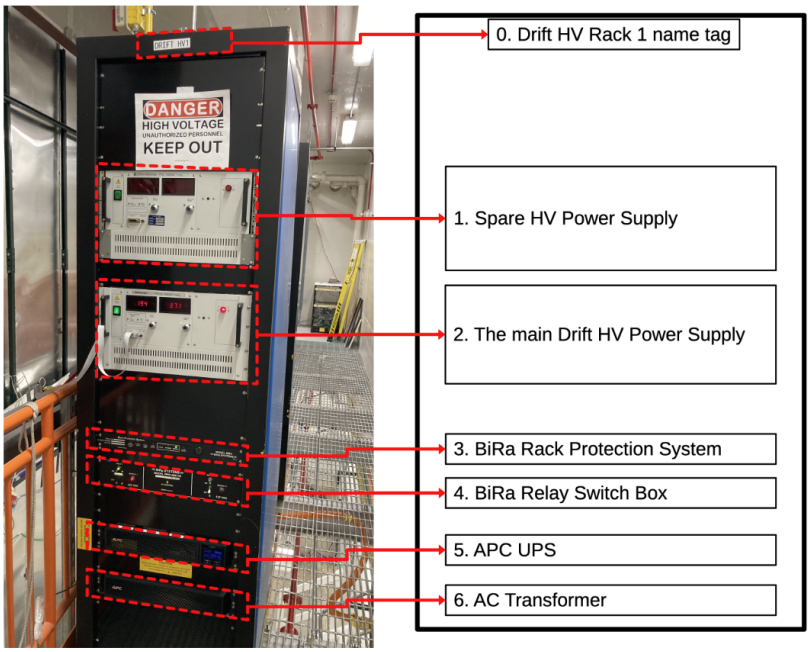

(a)

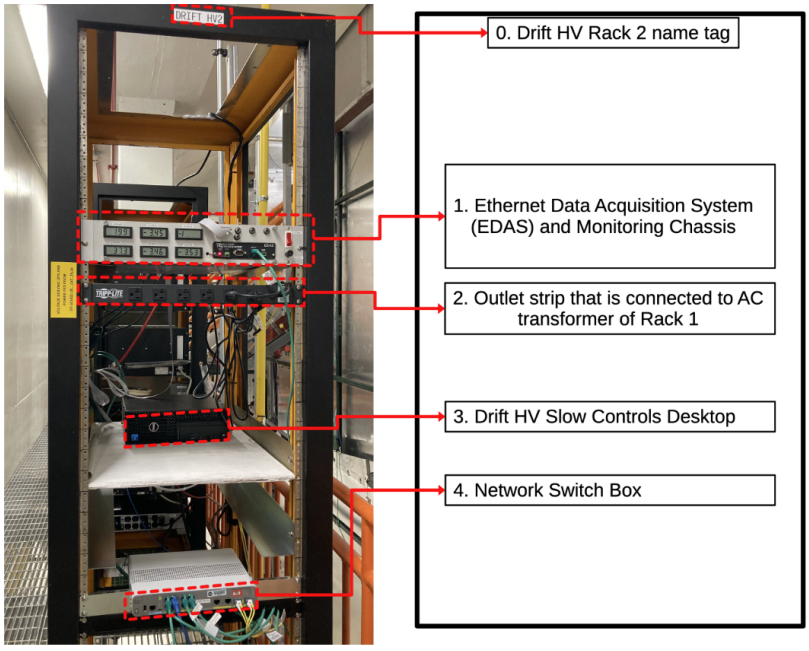

(b)

Figure B.1: Drift HV Racks located in the mezzanine level at the SBN-FD(ICARUS) building at Fermilab. (a) is the HV rack housing the HV components such as the HVPS. ICARUS at Fermilab only uses one HVPS due to the fact that a voltage splitter is used to feed the voltage to the two ICARUS modules. (b) is the monitoring Rack housing the monitor chassis, which contains the EDAS, the frontend drift HV desktop, and the network switch for communication to the EPICs database and the UPS.

Appendix C

Simulation Study I: Graphing Sensitivity Curves

```
######################################################################
#Hector Carranza PhD Candidate
#University of Texas at Arlington
#
#This code obtains the number of expected events for a given iBDM
#parameter set (m_0/E, m_1, m_2, epsilon, m_X) only for the
#primary interaction and graphs the sensitivity curve @ 90%CL
######################################################################

import random
import numpy as np
import scipy.integrate as integrate
import matplotlib.pyplot as plt
import statistics
from mpl_toolkits.mplot3d import Axes3D
```

```
import time
import math

start = time.time()

plt.rcParams['text.usetex'] = True

def mylambda(x,y,z):
        l = x**2 + y**2 + z**2 - 2*x*y - 2*x*z - 2*y*z
        return l

# All units are in GeV
# E = [0.2749]
E = [1,2,5,10]
# color_1 = [1,0,0,0.9,0,0,0.7,0,0,0.5,0,0,0.3]
# color_2 = [0,1,0,0,0.9,0,0,0.7,0,0,0.5,0,0]
# color_3 = [0,0,1,0,0,0.9,0,0,0.7,0,0,0.5,0,0]
m_1 = 0.02
m_2 = 0.028
m_DP = np.arange(0.001,2*m_1,0.00005)
m_e = 0.000511
N_e = 5.9*10**31
#N_e = 2.6*10**31


years = 0.31
detectors = 2
```

```
detector_efficency = 1


mixings = np.arange(0.00001, 0.001005, 0.000002)
fine_struc = 1/137

m_DP_graphing = []
mixing_graphing = []
A_cross_graphing = []
N_sig_graphing = []

m_DP_scattering = []
mixing_scattering = []
miminum_mixing_scattering = []
miminum_m_DP_scattering = []
minselect_mixing = []

chi2_flight_mdp = []
chi2_flight_mix = []

ax = plt.gca()
loopcounter = 0
for E_1 in E:
        F=(1.6*10**-4)*(1/E_1)**2
        s = m_1**2 + m_e**2 + 2*m_e*E_1


        recoil_term_1 = (2*m_e**2+2*E_1*m_e+m_1**2-m_2**2)/(2*np.sqrt(s))
        recoil_term_2 = (E_1+m_e)/np.sqrt(s)
```

```
        recoil_commonterm = recoil_term_1*recoil_term_2
        recoil_lambda_1 = ((((s-m_e**2-m_2**2)**2)-(4*(m_e**2)*(m_2**2)))*
(1/2))/(2*np.sqrt(s))
        recoil_lambda_2 = (np.sqrt(E_1**2-m_1**2))/np.sqrt(s)
        recoil_commonlambda = recoil_lambda_1*recoil_lambda_2

        empty_list = []

        E_e1_revised = recoil_commonterm - recoil_commonlambda
        E_e2_revised = recoil_commonterm + recoil_commonlambda

        a = (s + m_e**2 - m_1**2)/(2*math.sqrt(s))
        b = (s + m_e**2 - m_2**2)/(2*math.sqrt(s))
        c = math.sqrt(mylambda(s,m_1**2,m_e**2))/(2*math.sqrt(s))
        d = math.sqrt(mylambda(s,m_2**2,m_e**2))/(2*math.sqrt(s))

        E_recoil_minus = a * b - c * d
        E_recoil_plus  = a * b + c * d

        max_m2mass = np.sqrt(s) - m_e
        # print("Revised min Recoil Energy e= %f" % E_e1_revised)
        # print("Revised max Recoil Energy e= %f" % E_e2_revised)
        # print("max m2 mass = %f" % max_m2mass)
        # print(max_m2mass - 0.005*max_m2mass)

        print(E_e1_revised, E_e2_revised)
        print((1/m_e)*E_recoil_minus, (1/m_e)*E_recoil_plus)
```

```
    for mix in mixings:
            N_sig = 2.3
            for m in m_DP:
                    if N_sig < 2.3 or m==2*m_1:
                break
                    else:
                integral_constant = (4*(mix**2)*fine_struc*
        m_e**2)/((2568*10**24)((s-m_e**2-m_1**2)**2-(2*(m_e*m_1)**2)))

                integral = integrate.quad(lambda x:(m_e*(E_1**2+(E_1+m_e-x)**2)
((m_2-m_1)**2)*(m_e-0.5*x)+(m_e**2)*(m_e-x)+(m_1**2)*(E_1+m_e-x)
(m_2**2)*E_1)/((2*m_e*(m_e-x)-m**2)**2), E_e1_revised, E_e2_revised)

                            A_cross = integral_constant*integral[0]
                            # print(A_cross)
                            # print(integral)

                            N_sig = years * detectors *
detector_efficency * A_cross* F * N_e* 3.154*10**7

                            m_DP_graphing.append(m)
                            mixing_graphing.append(mix)
                            A_cross_graphing.append(A_cross)
                            N_sig_graphing.append(N_sig)

                            if N_sig >= 2.3:
                                    m_DP_scattering.append(m)
```

```
                                        mixing_scattering.append(mix)

                if mixing_scattering != empty_list and
  mixing_scattering[len(mixing_scattering)-1] == mix:
                        miminum_m_DP_scattering.append(m_DP_scattering
   [len(m_DP_scattering)-1])miminum_mixing_scattering.append(mix)



        ax.plot(miminum_m_DP_scattering, miminum_mixing_scattering, '-',
    markersize = '4', linewidth=4, label=r'$m_0 = %s$' % E_1)
        miminum_m_DP_scattering = []
        miminum_mixing_scattering = []
        loopcounter+=1

print(loopcounter)
# limits = [0.006, 0.305, 0.000022, 0.0035]
limits = [0.001, 1000, 0.000000001, 0.01]

plt.legend(fontsize=30)
ax.set_title(r'%.2f kton$\cdot$Year Exposure $m_{1} = %.3fGeV$, $m_{2} = %.3fGeV$'
% (years*0.43, m_1, m_2), fontsize=35)
ax.axvline(x = 2*m_1, color='black', linewidth=4, label=r'$m_X=2m_1$')
ax.set_yscale('log')
ax.set_xscale('log')
ax.set_xlabel('Dark Photon Mass (GeV)', fontsize=30)
ax.set_ylabel('Mixing Parameter', fontsize=30)
plt.yticks(fontsize=30)
```

```
plt.xticks(fontsize=30)
ax.set_xlim(limits[0], limits[1])
ax.set_ylim(limits[2], limits[3])
ax.set_zorder(2)
ax.set_facecolor('none')

ax_tw_x = ax.twinx()
ax_tw_x.axis('off')
ax2 = ax_tw_x.twiny()

# ax2 = ax.twinx().twiny()

img =  plt.imread('New_parameterspan_background.png')
ax2.axis('off')
# ax2.set_xscale('log')
# ax2.set_yscale('log')
ax2.imshow(img, extent = limits, aspect = 'auto')
end = time.time()
print(end-start)
plt.show()
```

Appendix D

Simulation Study II: Graphing $(m_1, \delta m)$ at $(m_X, \epsilon)_{limit}$ with $N_{expected}$

```
#####################################################################
#Hector Carranza PhD Candidate
#University of Texas at Arlington
#
#This code was used in conjunction with portions of the primary
#interaction sensitivity code to obtain the mass (m_0,m_1,m_2)
#parameter sets that are accessible to the ICARUS at Gran Sasso
#imposing selection criteria (E_depo, FV vertex containment,
#primary-secondary vertex displacment).
#####################################################################

import numpy as np
import math
import scipy.integrate as integrate
import matplotlib.pyplot as plt
```

```
import matplotlib.patches as mpatches
import statistics
from mpl_toolkits.mplot3d import Axes3D

plt.rcParams['text.usetex'] = True
plt.rcParams.update({'font.size':30})

E_1 = 2
N_thres = 2.3
m_1 = []
m_2 = []
N_sig_list = []
N_sig_cut_list = []
good_m1 = []
good_m2 =[]
bad_m1 = []
bad_m2 = []
max_m2mass = []
totenergy_pre = []
totenergy_pre_3cm = []
totenergy_3cm = []
totenergy = []
vertex_displacements_pre = []
vertex_displacements_non3cm_pre = []

vertex_displacements = []
vertex_displacements_non3cm = []
```

```
recoil_x_pre = []

recoil_y_pre = []

recoil_z_pre = []


pair_x_pre = []

pair_y_pre = []

pair_z_pre = []


recoil_x = []

recoil_y = []

recoil_z = []


pair_x = []

pair_y = []

pair_z = []


m_DP = 0.012

mixings = 0.0008


parameterlist_file = open('/Users/hectorc/Software/python_scripts/masslist_2GeV
_0.012GeV_0.0008mixing.txt', 'r')

parameterlist_data = parameterlist_file.readlines()


i = 0

while i < len(parameterlist_data):

        parameterlist_data[i] = parameterlist_data[i].split()
```

```
        m_1.append(float(parameterlist_data[i][0]))
        m_2.append(float(parameterlist_data[i][1]))
        max_m2mass.append(float(parameterlist_data[i][2]))
        N_sig_list.append(float(parameterlist_data[i][5]))
        # print(m_1[i], m_2[i])
        i+=1

counter = 0

j = 0
totalevents_pass = 0
totalevents_pass_3cm = 0
for m1 in m_1:
   newproduction_file = open('/Volumes/BackupPlus/iBDM_MonteCarlo/production
   /iBDM5000_2_masslist_0.012GeVmdp_0.0008mix/iBDM5000_%.0fGeV_%.3fGeV_%.3fGeV_%.6
   fGeV_%.6f_HEPevt.txt' % (E_1, float(m1), float(m_2[j]), m_DP, mixings), 'r')
   # newproduction_file = open('/media/hectorc/BackupPlus/iBDM_MonteCarlo/production/
   iBDM5000_0.7_masslis
   t_0.012GeVmdp_0.0008mix/iBDM5000_1GeV_%.3fGeV_%.3fGeV_%.6fGeV_%.6f_HEPevt.txt'
   % (float(m1), float(m_2[j]), m_DP, mixings), 'r')
   newproduction_data = newproduction_file.readlines()

   newepair_x_list = []
   newepair_y_list = []
   newepair_z_list = []

   i = 0
```

```
outside_counter = 0
inside_counter = 0
more_than_3cm_counter = 0
more_than_200_energy_counter = 0
while i < len(newproduction_data):

   event_newnumber = newproduction_data[i].split()

   if int(event_newnumber[1])==5:
      chi2_newdata = newproduction_data[i+1].split()
      chi1_newdata = newproduction_data[i+2].split()
      erecoil_newdata = newproduction_data[i+3].split()
      epair_newdata = newproduction_data[i+4].split()
      pospair_newdata = newproduction_data[i+5].split()
   if int(event_newnumber[1])==6:
      chi2_newdata = newproduction_data[i+1].split()
      chi1_newdata = newproduction_data[i+3].split()
      erecoil_newdata = newproduction_data[i+4].split()
      epair_newdata = newproduction_data[i+5].split()
      pospair_newdata = newproduction_data[i+6].split()

   newchi2_energy = float(chi2_newdata[9])
   newchi2_x = float(chi2_newdata[11])
   newchi2_y = float(chi2_newdata[12])
   newchi2_z = float(chi2_newdata[13])
   newchi2_px = float(chi2_newdata[6])
   newchi2_py = float(chi2_newdata[7])
```

```
newchi2_pz = float(chi2_newdata[8])
newchi2_posmag = math.sqrt(
newchi2_x**2 + newchi2_y**2 + newchi2_z**2)
newchi2_mommag = math.sqrt(
newchi2_px**2 + newchi2_py**2 + newchi2_pz**2)
newchi1_energy = float(chi1_newdata[9])
newchi1_x = float(chi1_newdata[11])
newchi1_y = float(chi1_newdata[12])
newchi1_z = float(chi1_newdata[13])
newchi2_distance = math.sqrt(
(newchi1_x-newchi2_x)**2 + (newchi1_y-newchi2_y)**2 + (newchi1_z-newchi2_z)**2)
newerecoil_energy = float(erecoil_newdata[9])
newerecoil_x = float(erecoil_newdata[11])
newerecoil_y = float(erecoil_newdata[12])
newerecoil_z = float(erecoil_newdata[13])
newerecoil_px = float(erecoil_newdata[6])
newerecoil_py = float(erecoil_newdata[7])
newerecoil_pz = float(erecoil_newdata[8])
newerecoil_posmag = math.sqrt(
newerecoil_x**2 + newerecoil_y**2 + newerecoil_z**2)
newerecoil_mommag = math.sqrt(
newerecoil_px**2 + newerecoil_py**2 + newerecoil_pz**2)
newepair_energy = float(epair_newdata[9])
newepair_x = float(epair_newdata[11])
newepair_y = float(epair_newdata[12])
newepair_z = float(epair_newdata[13])
newpospair_energy = float(pospair_newdata[9])
```

```
newpair_totenergy = newepair_energy + newpospair_energy
newdotproduct_chi2_erecoil = (newchi2_px*newerecoil_px) +
(newchi2_py*newerecoil_py) + (newchi2_pz*newerecoil_pz)
newcostheta_chi2_erecoil =
(newdotproduct_chi2_erecoil)/(newerecoil_mommag*newchi2_mommag)

if newepair_x < -363.49 or newepair_x > -76.94 or newepair_y > 129.96 or
newepair_y < -176.86 or newepair_z < -889.95 or newepair_z > 889.95:
   outside_counter+=1
   # print(event_newnumber[0])
else:
   inside_counter+=1
   vertex_displacements_non3cm_pre.append(newchi2_distance)
   if newchi2_distance > 3:
      more_than_3cm_counter+=1
      totenergy_pre_3cm.append(newpair_totenergy+newerecoil_energy)
      if newpair_totenergy + newerecoil_energy > 0.2:
         more_than_200_energy_counter+=1
         totenergy_pre.append(newpair_totenergy + newerecoil_energy)
         vertex_displacements_pre.append(newchi2_distance)
         recoil_x_pre.append(newerecoil_x)
         recoil_y_pre.append(newerecoil_y)
         recoil_z_pre.append(newerecoil_z)
         pair_x_pre.append(newepair_x)
         pair_y_pre.append(newepair_y)
         pair_z_pre.append(newepair_z)
```

```
    if int(event_newnumber[1])==5:
        i+=6
    if int(event_newnumber[1])==6:
        i+=7

if inside_counter == 0:
    ee_frac_contained = 0
    more_than_3cm_flight_frac = 0
    more_than_200_energy_frac = 0
else:
    ee_frac_contained = inside_counter/5000
    more_than_3cm_flight_frac = more_than_3cm_counter/5000
    more_than_200_energy_frac = more_than_200_energy_counter/5000

N_cut_0 = float(1) * float(N_sig_list[j])
N_cut_1 = float(ee_frac_contained) * float(N_sig_list[j])
N_cut_2 = float(more_than_3cm_flight_frac) * float(N_sig_list[j])
N_cut_3 = float(more_than_200_energy_frac) * float(N_sig_list[j])

if N_cut_3 > N_thres:
    totalevents_pass+=N_cut_3
    totalevents_pass_3cm+=N_cut_2
    good_m1.append(float(m1))
    good_m2.append(float(m_2[j]-m1))
    N_sig_cut_list.append(N_cut_3)
    for E in totenergy_pre:
```

```
            totenergy.append(E)
        totenergy_pre = []
        for E in totenergy_pre_3cm:
            totenergy_3cm.append(E)
        totenergy_pre_3cm = []
        for d in vertex_displacements_non3cm_pre:
            vertex_displacements_non3cm.append(d)
        vertex_displacements_non3cm_pre = []
        for d in vertex_displacements_pre:
            vertex_displacements.append(d)
        vertex_displacements_pre = []
        for x in pair_x_pre:
            pair_x.append(x)
        pair_x_pre = []
        for y in pair_y_pre:
            pair_y.append(y)
        pair_y_pre = []
        for z in pair_z_pre:
            pair_z.append(z)
        pair_z_pre = []
    else:
        bad_m1.append(float(m1))
        bad_m2.append(float(m_2[j]-m1))
        recoil_x_pre = []
        recoil_y_pre = []
        recoil_z_pre = []
        pair_x_pre = []
```

```
        pair_y_pre = []
        pair_z_pre = []
        vertex_displacements_pre = []
        vertex_displacements_non3cm_pre = []
        totenergy_pre = []
        totenergy_pre_3cm = []

    print(m1, m_2[j], format(ee_frac_contained,'.4f'),
    format(more_than_3cm_flight_frac,'.4f'), format(more_than_200_energy_frac,
    '.4f'), N_sig_list[j], N_cut_2)
    j+=1

plt.rcParams.update({'font.size': 30})

# numberlist = np.arange(1, 210, 1)
# print(numberlist)
# print(len(N_sig_list))

# z = np.array(N_sig_cut_list).reshape(3,3)
# plt.imshow(z)
# plt.figure()

# X,Y = np.meshgrid(m_1,m_2)
# plt.pcolormesh(X, Y, N_sig_cut_list)
# plt.figure()

# plt.plot(numberlist, N_sig_cut_list, '-', color = 'green', markersize = '4')
```

```
# plt.xlabel(r'Pair Number of £(m_{ 1 },m_{ 2 })£ (Total 209 Pairs)')
# plt.ylabel(r'£N_{ expected }£ with All Cuts')
# plt.grid()
# plt.figure()



axis_font=30

######################################################################
# plt.plot(good_m1, good_m2, 'o', markersize = '6',
color = 'green', label = 'Accepted')
plt.plot(bad_m1, bad_m2, 'o', markersize = '8',
color = 'Red', label = r'$N_{expected}<$ 2.3')
plt.scatter(good_m1, good_m2, s = 50, c = N_sig_cut_list, vmin = 2.3, vmax = 300)
plt.colorbar().set_label(r'$N_{expected}$', fontsize=axis_font)
# plt.plot(m_1, max_m2mass, 'o', markersize = '4',
color = 'red', label = r'$m_2$ Range')
# plt.plot(m_1, m_1, 'o', markersize = '4', color = 'red')
plt.legend(loc='upper right', title=r'$m_0=$%0.0f' % E_1)
# plt.title(r' £\chi_{ 1,2 }£ Mass Ranges for £N_{expected}£ £\ge£ %.1f and
$E_{\chi_1}$/$m_0$ = %2.1f GeV' % (N_thres, E_1))
plt.xlabel(r'$m_{ 1 }$ (GeV)', fontsize= axis_font, loc='right')
plt.ylabel(r'$\delta$$m$ (GeV)', fontsize=axis_font)
plt.xticks(fontsize=30)
plt.yticks(fontsize=30)
plt.grid()
```

```
plt.figure()

print((int((max(totenergy_3cm)-min(totenergy_3cm))/0.01)))
hist, bins = np.histogram(totenergy, bins=int((max(totenergy)-min(totenergy))/0.01))
twohist, twobins = np.histogram(totenergy_3cm,
bins=int((max(totenergy_3cm)-min(totenergy_3cm))/0.01))

# desired_sum = totalevents_pass  # The value you want the histogram to sum to
# hist_normalized = hist * desired_sum / np.sum(hist)

normed_events_list = []
for events in hist:
   normed_events = (events/sum(hist))*totalevents_pass
   normed_events_list.append(normed_events)



normed_events3cm_list = []
for events in twohist:
   normed_events = (events/sum(twohist))*totalevents_pass_3cm
   normed_events3cm_list.append(normed_events)

print(sum(normed_events_list)/sum(normed_events3cm_list))

# print(twobins)
# print(normed_events_list)
# print(sum(normed_events_list))
# print(totalevents_pass)
```

```
# print(totalevents_pass_3cm)


center = (bins[:-1] + bins[1:])/ 2
width = 1 * (bins[1] - bins[0])
twocenter = (twobins[:-1] + twobins[1:]) / 2
twowidth = 1 * (twobins[1] - twobins[0])
# twowidth = 0.01
print('%.3f' % twowidth)
colors = ['orange' if i > 0.2 else 'blue' for i in twocenter]
alphas = [0.5 if i > 0.2 else 1 for i in twocenter]
plt.bar(twocenter, normed_events3cm_list, align='center', width=twowidth, color=colors,
blue_patch = mpatches.Patch(color='blue', label=r'$E_{tot}<$200 MeV')
orange_patch = mpatches.Patch(color='orange', label=r'$E_{tot}>$200 MeV')
# handles = [plt.Rectangle((0,0),1,1, color=colors) for color in colors]
# plt.bar(center, normed_events_list, align='center', width=width, color='orange', alp
plt.xlabel(r'$E_{tot}$ (GeV)', fontsize=axis_font, loc='right')
plt.ylabel(r'Events/10MeV', fontsize=axis_font)
# plt.xlim(0, 1)
plt.xticks(fontsize=30)
plt.yticks(fontsize=30)
# plt.ticklabel_format(axis='y', style='sci', scilimits=(0,0))
plt.legend(title=r'$m_0=$%0.0fGeV' % E_1, handles=[blue_patch,orange_patch], fontsize=ax
plt.figure()


#########################################################
plt.title(r' Primary-Secondary Vertex Seperation for $N_{expected}$ $\ge$ %.1f and $E_{\
plt.hist(vertex_displacements_non3cm, range=[0,1813], bins=605, label='Primary-Secondary
```

```
plt.hist(vertex_displacements, range=[0,1813], bins=605, color='orange', label='Primary-
plt.xlabel(r'Seperation Distance (cm)', fontsize=axis_font)
plt.ylabel(r'Events', fontsize=axis_font)
# plt.ticklabel_format(axis='y', style='sci', scilimits=(0,0))
plt.axvline(x = 3, color='red', linewidth=3, label=r'3cm line'
# plt.axvline(x = 1812, color='red', linewidth=1, label=r'1812cm line')
plt.legend()
plt.xlim(0,150)
plt.xticks(fontsize=28)
plt.yticks(fontsize=28)
plt.show()
```

Appendix E

ξ_{GE} Graphing Code

```
######################################################################
#Hector Carranza PhD Candidate
#University of Texas at Arlington
#
#This code was used to book keep the global efficiencies of the
#various iBDM parameter sets and graph the result.
######################################################################
import matplotlib.pyplot as plt
import numpy as np
import scipy as sp
import scipy.interpolate
from mpl_toolkits.mplot3d import axes3d


plt.rcParams['text.usetex'] = True
master_GE = []
master_mass = []
```

```
master_epsilon = []


four_list =    [0.170, 0.131, 0.113, 0.098]
four_minlist = [0.071, 0.081, 0.093, 0.11]
five_list =    [0.353, 0.316, 0.276, 0.238,
                0.197, 0.165, 0.143, 0.118, 0.100, 0.094]
five_minlist = [0.028, 0.033, 0.039, 0.045,
                0.052, 0.060, 0.068, 0.077, 0.087, 0.098]
six_list =     [0.470, 0.425, 0.364, 0.332,
                0.313, 0.259, 0.217, 0.187, 0.184, 0.151, 0.128, 0.110, 0.094, 0.091]
six_minlist =  [0.017, 0.020, 0.023, 0.027,
                0.031, 0.036, 0.041, 0.047, 0.053, 0.060, 0.068, 0.076, 0.085, 0.095]


four_masslist = np.arange(0.018, 0.021+0.0001, 0.001)
five_masslist = np.arange(0.015, 0.024+0.0001, 0.001)
six_masslist = np.arange(0.014, 0.027+0.0001, 0.001)
################################################
three_six_masslist = [0.014, 0.015, 0.017, 0.018,
                      0.019, 0.020, 0.021, 0.023,
                      0.024, 0.025, 0.026, 0.027]
three_six_list =     [0.368, 0.321, 0.246, 0.203,
                      0.178, 0.150, 0.121, 0.092,
                      0.087, 0.077, 0.064, 0.057]
three_six_minlist =  [0.019, 0.022, 0.031, 0.036,
                      0.042, 0.048, 0.055, 0.072,
                      0.081, 0.092, 0.103, 0.116]
```

```
three_five_masslist= [0.015, 0.017, 0.019, 0.020,
                      0.021, 0.022, 0.023, 0.024]
three_five_list =    [0.259, 0.185, 0.136, 0.111,
                      0.099, 0.080, 0.064, 0.061]

three_four_masslist= [0.018, 0.019, 0.020, 0.021]
three_four_list =    [0.110, 0.095, 0.070, 0.068]
#####################################################
one_six_masslist =   [0.014, 0.015, 0.016, 0.017,
                                    0.018, 0.019, 0.020]
one_six_list =       [0.499, 0.451, 0.388, 0.353,
                                    0.292, 0.259, 0.224]
one_five_masslist =  [0.015, 0.016, 0.017, 0.018,
                                    0.019, 0.020]
one_five_list =      [0.371, 0.325, 0.280, 0.226,
                                    0.200, 0.172]

one_four_masslist =  [0.018, 0.019, 0.020]
one_four_list =      [0.166, 0.134, 0.117]




#####################################################
plt.plot(one_six_masslist, one_six_list, '--',
        color='black',label=r'$\epsilon$ = 0.0006 for $m_1=0.01GeV,m_2=0.019GeV$')
# plt.plot(three_six_masslist, three_six_minlist, '-',
        color='orange', label=r'mixing parameter = 0.0006 for 0.03GeV, $2.3/N_{Theo}$')
```

```
plt.plot(one_five_masslist, one_five_list, '--',
        color='red',label=r'$\epsilon$ = 0.0005 for $m_1=0.01GeV,m_2=0.019GeV$')
# plt.plot(three_six_masslist, three_six_minlist, '-',
        color='orange', label=r'mixing parameter = 0.0006 for 0.03GeV, $2.3/N_{Theo}$')

plt.plot(one_four_masslist, one_four_list, '--',
        color='blue',label=r'$\epsilon$ = 0.0004 for $m_1=0.01GeV,m_2=0.019GeV$')
# plt.plot(three_six_masslist, three_six_minlist, '-',
        color='orange', label=r'mixing parameter = 0.0006 for 0.03GeV, $2.3/N_{Theo}$')

#######################################################
# plt.title(r'Global Efficiency Calculated vs Minimum Global Efficiency Allow by
$N_{Theo}$')
plt.title(r'$\xi_{GE}$ for $(m_X,\epsilon)$ Sample Points Setting $m_0=2GeV$',
fontsize=30)

plt.plot(six_masslist, six_list, '-o',
        color='black', label=r'$\epsilon$ = 0.0006 for $m_1=0.02GeV,m_2=0.028GeV$')
# plt.plot(six_masslist, six_minlist, '-',
        color='black', label=r'mixing parameter = 0.0006 for 0.02GeV, $2.3/N_{Theo}$')

plt.plot(five_masslist, five_list, '-o',
        color='red', label=r'$\epsilon$ = 0.0005 for $m_1=0.02GeV,m_2=0.028GeV$')
# plt.plot(five_masslist, five_minlist, '-',
        color='red', label=r'mixing parameter = 0.0005for 0.02GeV, $2.3/N_{Theo}$')
```

```
plt.plot(four_masslist, four_list, '-o',
        color='blue', label=r'$\epsilon$ = 0.0004 for $m_1=0.02GeV,m_2=0.028GeV$')
# plt.plot(four_masslist, four_minlist, '-',
        color='blue', label=r'mixing parameter = 0.0004 for 0.02GeV, $2.3/N_{Theo}$')
#########################################################
plt.plot(three_six_masslist, three_six_list, '-',
        color='black',label=r'$\epsilon$ = 0.0006 for $m_1=0.03GeV,m_2=0.037GeV$')
# plt.plot(three_six_masslist, three_six_minlist, '-',
        color='orange', label=r'mixing parameter = 0.0006 for 0.03GeV, $2.3/N_{Theo}$')

plt.plot(three_five_masslist, three_five_list, '-',
        color='red',label=r'$\epsilon$ = 0.0005 for $m_1=0.03GeV,m_2=0.037GeV$')
# plt.plot(three_six_masslist, three_six_minlist, '-',
        color='orange', label=r'mixing parameter = 0.0006 for 0.03GeV, $2.3/N_{Theo}$')

plt.plot(three_four_masslist, three_four_list, '-',
        color='blue',label=r'$\epsilon$ = 0.0004 for $m_1=0.03GeV,m_2=0.037GeV$')
# plt.plot(three_six_masslist, three_six_minlist, '-',
        color='orange', label=r'mixing parameter = 0.0006 for 0.03GeV, $2.3/N_{Theo}$')

plt.xlabel(r'$m_X$ (GeV)', fontsize=30)
plt.ylabel(r'$\xi_{GE}$', fontsize=30)
plt.legend(fontsize=18)
plt.xticks(fontsize=30)
plt.yticks(fontsize=30)
plt.show()
```